

**INTERVERTEBRAL DISC DEGENERATION, QUANTIFIED BY T2* MRI,
BIOCHEMISTRY, AND COMPRESSIVE MECHANICS, CORRELATED TO
GLOBAL FUNCTIONAL MECHANICS OF THE LUMBAR SPINE**

**A DISSERTATION SUBMITTED TO THE FACULTY OF
UNIVERSITY OF MINNESOTA**

BY

ARIN MICHAEL ELLINGSON

**IN PARTIAL FULFILLMENT OF THE REQUIREMENTS FOR THE DEGREE OF
DOCTOR OF PHILOSOPHY**

DAVID J. NUCKLEY

MAY 2013

ACKNOWLEDGEMENTS

I would first like to thank my advisor, David J. Nuckley, his guidance, support, and encouragement at times of need lead to the accomplishment of this dissertation. I would also like to express my gratitude to my committee members, David W. Polly Jr., Joan E. Bechtold, Victor Barocas, and Daniel F. Keefe, for their time and efforts shaping this dissertation. The expert support by my committee members as well as Jutta Ellerman, Sandy Johnson, Peter Kollasch, and Conrad Lindquist allowed for a multidisciplinary dissertation of this nature to be achieved. I would also like to thank the members of the lab, specifically Hitesh Mehta and Tina Nagel, for their data collection assistance, motivation, and support. Finally, I would like to acknowledge the University of Minnesota Musculoskeletal Training Grant (NIH/NIAMS T32 AR050938) and in particular the directors Denis Clohisy and Cathy Carlson. Their financial and moral support was pivotal in allowing me to explore my own research interests.

“If I have seen further it is by standing on the shoulders of giants.”

– Sir Isaac Newton

DEDICATION

I dedicate this dissertation to my wife for her constant love and continued support.

ABSTRACT

Low back pain is one of the most prevalent health complaints in the US, with an estimated 70-85% of the population developing back pain at some point in their life, creating a significant financial burden. Although the causes of low back pain are poorly defined and indistinct, most often implicated as the origin of pain, is the intervertebral disc. The disc affords the spine its extensive multidirectional motion due to the complex interaction between two morphologically, biomechanically, and biochemically distinct tissues: the annulus fibrosus and the nucleus pulposus. With advancing age, injury, pathology or a combination of these, a degenerative cascade of biomechanical, biochemical, and nutritional alterations diminish the discs' ability to maintain its structure and function. Unfortunately, measurement of these properties *in vivo* is currently not a viable option due to the invasiveness of the procedures. Therefore, an indirect method is needed to evaluate the multifarious characteristics of a patient's disc health. Of critical interest is the relationship that functional spinal mechanics has with the morphologic, biochemical, and biomechanical properties of the intervertebral disc as they change with degeneration.

Eighteen osteoligamentous cadaveric lumbar spines that spanned the degenerative spectrum were utilized in a correlation study design to evaluate the relationships between each factors of disc health: imaging, biochemical content, biomechanical competency, and functional mechanics. Each specimen was first imaged using quantitative T2* MRI techniques, where the site-specific relaxation times and features of the Pfirrmann grading system, including signal intensity and distinction between the nucleus pulposus and surrounding annulus fibrosus, were measured. Then their functional spinal mechanics

were evaluated and range of motion, neutral zone ratio, bending stiffness and helical axis patterns were computed. Local biochemical content and compressive biomechanical properties were subsequently analyzed. Each outcome measure was then assessed with respect to the others using correlation statistical methods in an effort to understand the multifactorial relationships surrounding disc degeneration.

The T2* relaxation times and newly defined variables, T2* Intensity Area and Transition Zone Slope, were significantly correlated to the standard Pfirrmann grading, showing the T2* MR imaging parameters are sensitive to the morphological changes associated with disc degeneration. Also, these features enable the quantitative grading of disc degeneration without subjectivity or bias but with clinically recognized features of distinction. Furthermore, T2* relaxation times were found to have a high sensitivity for detecting the proteoglycan content of the intervertebral disc, which may potentially have a profound impact on the early diagnosis of degeneration. The T2* relaxation times were also significantly correlated to the residual stress and excised strain of the disc. These multi-faceted changes that occur with degeneration impact the global mechanics of the spinal unit by increasing the neutral zone to range of motion ratio, or joint instability, and altering the bending stiffness and range of motion. Even stronger correlations were measured with alterations in the helical axis patterns of lateral bending. There was a marked increase of out-of-plane rotations and a larger migration of the instantaneous axis of rotation with worsening degeneration evaluated by MRI, local biochemistry, and local residual mechanics.

Quantitative T2* MRI has the sensitivity to predict the local biochemical and biomechanical properties of the intervertebral disc. Complementary to MRI analysis, the

measurement of the pathway of motion throughout the degenerative progress, using the helical axis approach, can enhance the disc assessment. Altogether, these clinically viable methods may immediately improve the characterization of the intervertebral disc for enhanced treatment and care.

TABLE OF CONTENTS

ACKNOWLEDGEMENTS	I
DEDICATION	II
ABSTRACT	III
LIST OF TABLES	IX
LIST OF FIGURES	X
1 CHAPTER 1: MOTIVATION	1
2 CHAPTER 2: INTRODUCTION- REVIEW OF LITERATURE	3
2.1 ANATOMY OF THE SPINE	3
2.2 INTERVERTEBRAL DISC	5
2.3 KINEMATICS OF THE LUMBAR SPINE	6
2.3.1 RANGE OF MOTION AND NEUTRAL ZONE	8
2.3.2 HELICAL AXES OF MOTION AND INSTANTANEOUS AXIS OF ROTATION	9
2.4 INTERVERTEBRAL DISC DEGENERATION	11
2.4.1 MORPHOLOGICAL CHANGES.....	11
2.4.2 BIOCHEMICAL CHANGES	16
2.4.3 TISSUE MECHANICAL CHANGES.....	18
2.4.4 FUNCTIONAL MECHANICAL CHANGES	22
2.5 SUMMARY OF INTRODUCTION	23
3 CHAPTER 3: STUDY DESIGN AND SPECIFIC AIMS	25
3.1 STUDY DESIGN	25
3.2 SPECIFIC AIMS.....	26
3.3 HYPOTHESES	28
4 CHAPTER 4: RESEARCH METHODS	31
4.1 MAGNETIC RESONANCE IMAGING	31

4.1.1	TRADITIONAL T2 WEIGHTED MAGNETIC RESONANCE IMAGING	32
4.1.2	QUANTITATIVE T2* MAGNETIC RESONANCE IMAGING	33
4.1.3	IMAGING ANALYSIS.....	34
4.1.4	SUMMARY OF IMAGING PARAMETERS	37
4.2	FUNCTIONAL LUMBAR SPINE MECHANICS	37
4.2.1	SPINE KINETIC SIMULATOR	38
4.2.2	OPTICAL MOTION CAPTURE SYSTEM	39
4.2.3	TESTING PROCEDURE	40
4.2.4	FUNCTIONAL LUMBAR MECHANICAL OUTCOMES	41
4.2.5	SUMMARY OF FUNCTIONAL SPINE MECHANICS PARAMETERS	43
4.2.6	HELICAL AXIS OF MOTION	43
4.2.7	SUMMARY OF HELICAL AXIS PARAMETERS	49
4.3	LOCAL TISSUE COMPRESSIVE MECHANICS	49
4.3.1	HYBRID CONFINED / IN SITU INDENTATION METHODOLOGY	51
4.3.2	SUMMARY OF COMPRESSIVE MECHANICAL PROPERTIES.....	55
4.4	BIOCHEMICAL ANALYSIS	55
4.4.1	SUMMARY OF BIOCHEMICAL PROPERTIES	59
4.5	STATISTICAL TREATMENT AND TESTING OF HYPOTHESES	59
5	CHAPTER 5: RESULTS	65
5.1	QUANTITATIVE T2* ASSESSMENT OF DISC HEALTH	66
5.2	BIOCHEMICAL CONTENT	67
5.3	LOCAL BIOMECHANICAL PROPERTIES	70
5.4	LOCATION DEPENDENT CHANGES IN DISC HEALTH	73
5.5	FUNCTIONAL MECHANICAL OUTCOMES.....	82
5.6	ALTERATIONS IN HELICAL AXES.....	85

5.7	FUNCTIONAL MECHANICS CHANGES WITH LOCAL PROPERTIES	94
6	CHAPTER 6: DISCUSSION.....	99
6.1	EXAMINATION OF TESTED HYPOTHESES	100
6.2	QUANTITATIVE T2* ASSESSMENT OF DISC HEALTH	109
6.3	SITE-SPECIFIC CHANGES WITH DISC HEALTH	111
6.4	CHANGES IN FUNCTIONAL MECHANICS WITH DISC HEALTH.....	115
6.5	HELICAL AXES CHANGES WITH DISC HEALTH	118
6.6	DEVELOPMENT AND PARAMETERIZATION OF A PREDICTIVE MODEL.....	121
6.7	EXPERIMENTAL LIMITATIONS	128
6.8	SUMMARY	131
7	BIBLIOGRAPHY	134
8	APPENDIX.....	143
8.1	T2* MRI MAPS	143
8.2	HELICAL AXIS COMPUTATION.....	147
8.2.1	HELICAL AXIS VALIDATION	147
8.2.2	HELICAL AXIS SENSITIVITY ANALYSIS	148

LIST OF TABLES

<i>Table 2.1. Literature Reported Ranges of Motion and Representative Angles (degrees)¹¹</i>	9
<i>Table 2.2. Literature Reported Neutral Zone (degrees), Ranges of Motion (degrees), and Neutral Zone Ratio (%)¹⁵</i>	9
<i>Table 4.1. Imaging Parameters (n=54)</i>	37
<i>Table 4.2. Functional Spine Mechanics Parameters (n=54)</i>	43
<i>Table 4.3. Helical Axis Parameters (n=18)</i>	49
<i>Table 4.4. Compressive Mechanical Parameters (n=18)</i>	55
<i>Table 4.5. Biochemical Parameters (n=18)</i>	59
<i>Table 5.1. Specimen Demographics</i>	65
<i>Table 5.2. Correlations between T2* Imaging Parameters and Pfirrmann Grade</i>	67
<i>Table 5.3. Correlations between T2* Relaxation Times (ms) and Biochemical Content</i>	69
<i>Table 5.4. Correlations between Transition Zone Slope and Biochemical Content</i>	69
<i>Table 5.5. Correlations between T2* Intensity Area and Biochemical Content</i>	70
<i>Table 5.6. Correlations between Pfirrmann Grade and Biochemical Content</i>	70
<i>Table 5.7. Correlations between T2* Relaxation Times and Local Biomechanics</i>	72
<i>Table 5.8. Correlations between Transition Zone Slope and Local Biomechanics</i>	72
<i>Table 5.9. Correlations between T2* Intensity Area and Local Biomechanics</i>	73
<i>Table 5.10. Correlations between Pfirrmann Grade and Local Biomechanics</i>	73
<i>Table 5.11. Correlations between T2* Parameters and Range of motion and Neutral Zone Ratio</i>	83
<i>Table 5.12. Correlations between T2* Parameters and Bending Stiffness</i>	83
<i>Table 5.13. Correlations between T2* Parameters and Range of motion and Neutral Zone Ratio</i>	95
<i>Table 5.14. Correlations between T2* Parameters and Bending Stiffness</i>	95
<i>Table 6.1. Correlation between Strong Predictors of Disc Health</i>	122
<i>Table 6.2. Linear Regression Coefficients</i>	123
<i>Table 6.3. Multiple Linear Regression Model Parameters</i>	126

LIST OF FIGURES

<i>Figure 2.1. Anatomy of the Spinal Column.....</i>	<i>3</i>
<i>Figure 2.2. Anatomy of a Functional Spinal Unit.</i>	<i>4</i>
<i>Figure 2.3. Biochemical Composition of the Intervertebral Disc.</i>	<i>5</i>
<i>Figure 2.4. Intervertebral Disc Load Distribution During Compression.</i>	<i>6</i>
<i>Figure 2.5. Bending Directions of the Lumbar Spine.</i>	<i>7</i>
<i>Figure 2.6. Force Distribution During Bending.....</i>	<i>8</i>
<i>Figure 2.7. Theoretical Helical Axes in the Lumbar Spine.</i>	<i>10</i>
<i>Figure 2.8. Pfirrmann Grading System.</i>	<i>13</i>
<i>Figure 2.9. Fiber interactions between disc and cartilaginous endplate.</i>	<i>19</i>
<i>Figure 2.10. Average Relaxation Curves Showing Percent Relaxation Rate.....</i>	<i>21</i>
<i>Figure 3.1. Specific Aims.....</i>	<i>27</i>
<i>Figure 4.1. Conventional T2 weighted and T2* Mapping MRI.....</i>	<i>32</i>
<i>Figure 4.2. Quantitative T2* MRI Mapping.....</i>	<i>33</i>
<i>Figure 4.3. Magnetic Resonance Images of Lumbar Spine and Intervertebral Disc Using T2 and Quantitative T2* Techniques.....</i>	<i>34</i>
<i>Figure 4.4. T2* Coronal Plane Profile of Mid-Sagittal Region of Interest.....</i>	<i>35</i>
<i>Figure 4.5. Quantification of Imaging Parameters, Transition Zone Slope and T2* Intensity Area, from T2* Relaxation Profile in the Coronal Plane of ROI 3.</i>	<i>35</i>
<i>Figure 4.6. Intervertebral Disc Test Sites.....</i>	<i>36</i>
<i>Figure 4.7. Illustration of the Spine Kinetic Simulator.</i>	<i>38</i>
<i>Figure 4.8. Image of Spine Kinetic Simulator.</i>	<i>39</i>
<i>Figure 4.9. Specimen Loading in Spine Kinetic Simulator.....</i>	<i>40</i>
<i>Figure 4.10. Representative Angular Displacement- Moment Plot with Metrics.....</i>	<i>42</i>
<i>Figure 4.11- Helical Axis Parameters.....</i>	<i>44</i>
<i>Figure 4.12. Instantaneous Helical Axis of Motion.....</i>	<i>46</i>
<i>Figure 4.13. Representative Angle vs. Moment Plot with 1 Nm Bins.....</i>	<i>47</i>
<i>Figure 4.14. Minimally Enclosed Ellipse of IAR, Vector Tips, and Volume of Vector Space.....</i>	<i>48</i>
<i>Figure 4.15. Sample Preparation for Hybrid Confined/in situ Indentation Tests.....</i>	<i>50</i>
<i>Figure 4.16. Hybrid Confined/in situ Indentation Test Sites.....</i>	<i>51</i>
<i>Figure 4.17. Time history of stress-relaxation protocol with representative test site data.....</i>	<i>52</i>

<i>Figure 4.18. Sites for Biochemical Analysis.</i>	56
<i>Figure 4.19. Schematic for Biochemical Analysis.</i>	57
<i>Figure 5.1. Distribution of Disc Health.</i>	66
<i>Figure 5.2. Correlation between T2* Imaging Parameters and Pfirrmann Grade.</i>	67
<i>Figure 5.3. Correlation between T2* Relaxation Time and Glycosaminoglycan Content.</i>	68
<i>Figure 5.4. Correlations between T2* Relaxation time and Excised Strain and Residual Stress.</i>	71
<i>Figure 5.5. Example Plot with Locations Labeled.</i>	74
<i>Figure 5.6. Location Based Differences in T2* Relaxation Times for Healthy, Moderate, and Severely Degenerated Discs.</i>	76
<i>Figure 5.7. Location Based Differences in Residual Stress for Healthy, Moderate, and Severely Degenerated Discs.</i>	76
<i>Figure 5.8. Location Based Differences in Excised Strain for Healthy, Moderate, and Severely Degenerated Discs.</i>	77
<i>Figure 5.9. Location Based Differences in Glycosaminoglycan Content for Healthy, Moderate, and Severely Degenerated Discs.</i>	77
<i>Figure 5.10. Location Based Differences in Hydroxyproline Content for Healthy, Moderate, and Severely Degenerated Discs.</i>	78
<i>Figure 5.11. T2* Relaxation Time as a Function of Disc Health at Different Locations.</i>	79
<i>Figure 5.12. T2* Residual Stress as a Function of Disc Health at Different Locations.</i> .	80
<i>Figure 5.13. Excised Strain as a Function of Disc Health at Different Locations.</i>	80
<i>Figure 5.14. Glycosaminoglycan Content as a Function of Disc Health at Different Locations.</i>	81
<i>Figure 5.15. Hydroxyproline Content as a Function of Disc Health at Different Locations.</i>	82
<i>Figure 5.16. Correlational Plots Between Flexion Stiffness and Range of Motion with Disc Health.</i>	84
<i>Figure 5.17. Correlational Plots Between Lateral Bending Stiffness and Neutral Zone Ratio with Disc Health.</i>	85
<i>Figure 5.18. Representative Helical Axes from a Healthy Intervertebral Disc.</i>	86
<i>Figure 5.19. Representative Helical Axes from a Degenerative Intervertebral Disc.</i>	86
<i>Figure 5.20. Example Angle- Moment Plot Illustrating a significant correlation between the helical axis parameter (n_x) and measure of disc health (transition zone slope).</i>	87
<i>Figure 5.21. Primary Helical Axis Orientation (x-axis) During Lateral Bending.</i>	88
<i>Figure 5.22. Changes in the Helical Axis Orientation (z-axis) During Lateral Bending.</i>	89

<i>Figure 5.23. Changes in the Helical Axis Orientation (y-axis) During Lateral Bending.</i>	90
<i>Figure 5.24. Changes in the Standard Deviation of the Primary Helical Axis Orientation (x-axis) During Lateral Bending.....</i>	91
<i>Figure 5.25. IAR Location (lateral) During Lateral Bending.</i>	92
<i>Figure 5.26. Standard Deviation of the IAR Location (lateral) During Lateral Bending.</i>	92
<i>Figure 5.27. Changes in the Standard Deviation of the Instantaneous Axis of Rotation Location (superior direction) During Lateral Bending.</i>	93
<i>Figure 5.28. Changes in the Primary Helical Axis Orientation (x-axis) During Lateral Bending.</i>	96
<i>Figure 5.29. Changes in the Helical Axis Orientation (z-axis) During Lateral Bending.</i>	97
<i>Figure 5.30. Changes in the Helical Axis Orientation (y-axis) During Lateral Bending. A yellow bar indicates a significant negative correlation with NP parameter listed above each subplot over the corresponding 1 Nm window ($p < 0.05$). This suggests an increased flexion component in the rotation during at the areas shaded in yellow.</i>	97
<i>Figure 5.31. Changes in the Instantaneous Axis of Rotation Location (lateral direction) During Lateral Bending.</i>	98
<i>Figure 6.1. T2* Relaxation Time Correlational Plots of the Nucleus Pulposus and Inner Annulus Fibrosus.</i>	114
<i>Figure 6.2. Lumbar Facet Orientation and Coupling Nature.</i>	116
<i>Figure 6.3. Representative Helical Axis Patterns of Healthy (top) and Degenerative (bottom) Disc during Lateral Bending.</i>	119
<i>Figure 6.4. Sulfated-Glycosaminoglycan Predictive Model.</i>	124
<i>Figure 6.5. Residual Stress Predictive Model.</i>	125
<i>Figure 6.6. Excised Strain Predictive Model.</i>	126
<i>Figure 8.1. Helical Axis Validation Set-up.</i>	148
<i>Figure 8.2. Helical Axis Sensitivity Analysis.</i>	149

1 CHAPTER 1: MOTIVATION

Chronic low back pain is one of the most prevalent health complaints in the US, with an estimated 70-85% of the population developing back pain at some point in their life¹. It is the leading cause of lost wages and accounts for more than 700,000 surgical procedures per year with a total of over \$80 billion annually spent on treatment and care^{2,3}. Although the causes of low back pain are poorly defined and indistinct, the most often implicated tissue as the origin for pain is the intervertebral disc. The intervertebral disc affords the spine its extensive multidirectional motion due to the complex interaction between two morphologically, biomechanically, and biochemically distinct tissues: the annulus fibrosus (AF) and the nucleus pulposus (NP). The AF consists of highly organized concentric rings of fibrocartilaginous material surrounding the NP, which is composed of a hydrated, disorganized matrix of collagen and proteoglycans. With advancing age, injury, musculoskeletal pathology or a combination of these, a degenerative cascade of biomechanical, biochemical, and nutritional alterations diminish the discs' ability to maintain its structure and function. Morphologically and biochemically, disc degeneration presents with decreased proteoglycans, reduced water content, altered collagen synthesis and degradation, an amorphous transition zone between the annulus fibrosus and nucleus pulposus, and a decrease in total disc height. Biomechanically, degeneration progresses with decreased spinal stability, which may occlude the spinal cord and/or pinch the nerve roots. Altogether, these degenerative changes lead to increased pain be it osteoligamentous, muscular, or peripheral in nature—a health outcome with significant debilitating and financial costs.

Traditional range of motion measurements, mechanical properties, and biochemical composition of the disc have been shown to progress with disc degeneration severity and these changes provide sensitive and accurate predictors of progression. Unfortunately, measurement of these properties *in vivo* is currently not a viable option due to the invasiveness of the procedures. Therefore, an indirect method is needed to evaluate the multifarious characteristics of a patient's disc health. Of critical interest is the relationship that intervertebral disc functional mechanics has with the other morphologic, biochemical, and biomechanical properties that change with degeneration.

This research program aimed to define the relationship between disc degeneration, quantitatively assessed using magnetic resonance imaging, biochemical analyses, and local compressive mechanics, and global functional lumbar spine mechanics.

Together, these goals will lead to an enhanced mechanistic understanding of the degenerative intervertebral disc and the potential clinical utility of an *in vivo* kinematic disc health assessment strategy.

2 CHAPTER 2: INTRODUCTION- REVIEW OF LITERATURE

Considering the pain, dysfunction, and financial burden that spinal health problems create, this dissertation will address the health of the intervertebral disc from a multifactorial perspective. Thus, this review of the literature will provide the basis for subsequent experiments and a critical examination of hypotheses aimed at revealing discriminating factors of lumbar intervertebral disc health. Achievement may improve care and treatment for individuals suffering from low back pain.

2.1 ANATOMY OF THE SPINE



Figure 2.1. Anatomy of the Spinal Column.

The spine can be divided into five distinct regions (superior to inferior): cervical, thoracic, lumbar, sacral, and coccygeal⁴.

The vertebral column is a complex structure that provides mobility while maintaining stability of the trunk and extremities. It is also responsible for providing protection for the spinal cord. The vertebral column can be divided into five distinct regions (superior to

inferior): cervical, thoracic, lumbar, sacral, coccygeal (Figure 2.1). For the purposes of this dissertation, focus will be taken on the lumbar region, which is composed of five vertebrae with intervening intervertebral discs, ligaments, and other soft tissues connecting them.

The unique shape of the vertebral bodies allows for the transmission of load, where the posterior elements protect the neural space and allow for muscle attachment to the transverse and spinous processes. Each functional spinal unit, bone-disc-bone construct, consists of two articular facet joints on each lateral side made up from the superior and inferior articular processes. The facets form a supportive column known as the articular pillar helping guide motion, while providing additional transfer of load. Figure 2.2 illustrates the typical lumbar vertebra and the positioning of the attached ligaments, intended to provide additional support and stability.

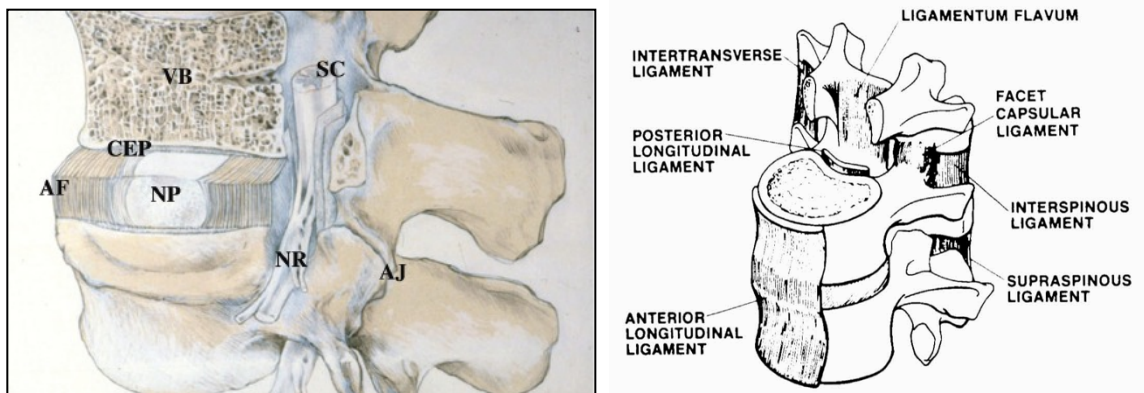


Figure 2.2. Anatomy of a Functional Spinal Unit.

Left- The intervertebral disc is made up of the nucleus pulposus (NP) is surrounded by the annulus fibrosus (AF), which separates adjacent vertebral bodies (VB) by the cartilaginous end-plate (CEP). The image also shows the spinal cord (SC), nerve roots (NR), and the apophyseal or facet joints (AJ) (reprinted with permission)⁵. **Right-** Ligaments of the spine (reprinted with permission)⁶.

2.2 INTERVERTEBRAL DISC

The intervertebral disc allows the spine its extensive multidirectional motion due to the complex interaction between two morphologically, biomechanically, and biochemically distinct tissues: the annulus fibrosus (AF) and the nucleus pulposus (NP) (Figure 2.3). The AF consists of highly organized concentric rings (lamellae) of fibrocartilaginous material surrounding the NP. The lamellae are primarily composed of Type I collagen fibers oriented at approximately 30 degrees from the horizontal and altering direction with each successive layer. The NP is composed of a hydrated, disorganized matrix of collagen (mainly Type II, with Types VI, IX, X, XI to a lesser degree) and proteoglycans (principally Aggrecan)^{7,8}. Due to the high concentration of proteoglycans, which are negatively charged hydrophilic molecules, water diffuses into the NP providing an internal osmotic pressure to the IVD.

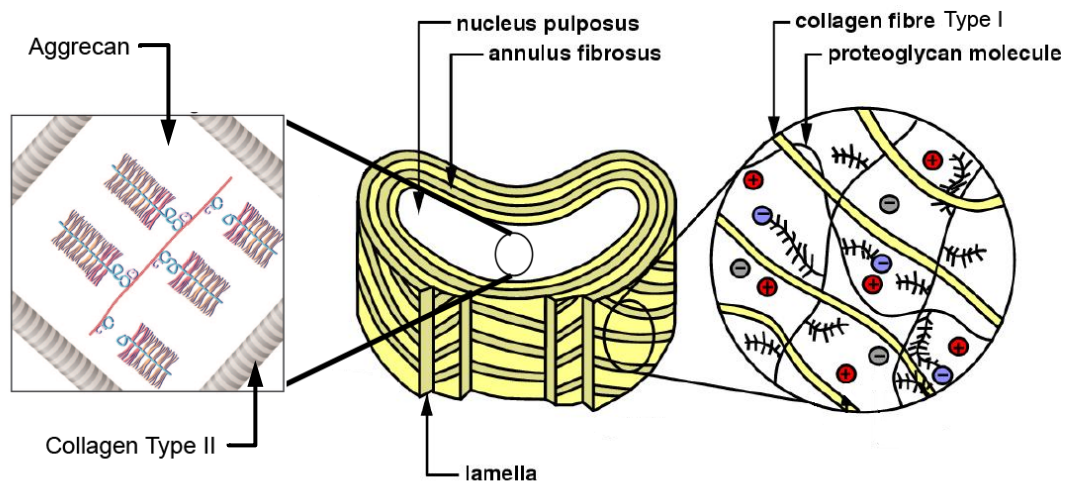


Figure 2.3. Biochemical Composition of the Intervertebral Disc.

Left- Shows the interaction of proteoglycans (Aggrecan) and collagen Type II in the NP. **Middle-** Shows the relative positions and macro-structure of the disc, highlighting the lamella of the annulus fibrosus, surrounding the nucleus pulposus. **Right-** Shows the orientation ($\sim 30^\circ$ from the horizontal) of collagen Type I fibers and their interactions with proteoglycans. Reprinted with permission^{9,10}.

When a load is applied to the spine, the hydrated NP acts like a pressure vessel, placing the AF in tension (Figure 2.4). This unique system allows the disc to absorb and dissipate large compressive loads applied to the spine.

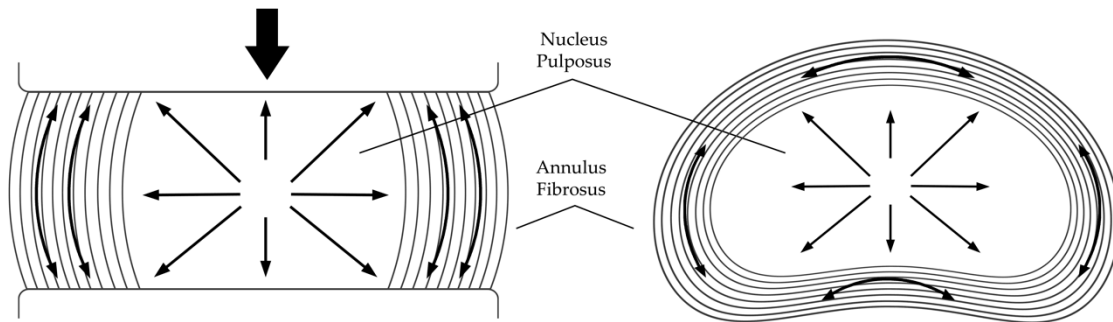


Figure 2.4. Intervertebral Disc Load Distribution During Compression. When a load is applied to the spine, the hydrated nucleus pulposus acts like a pressure vessel, placing the annulus fibrosus in tension (adapted from White and Panjabi)¹¹.

2.3 KINEMATICS OF THE LUMBAR SPINE

Typically, individuals with low back pain exhibit some alterations in their movement or kinematics and thus, this section will review healthy spinal kinematics as to define terms and create a foundation for assessment of unhealthy spinal motion¹². Spinal kinematics, the study of motion without regard to the influence of forces, of a healthy spine is pivotal in establishing a normal pattern of motion, which is critical to the identification of irregularities. There are two main metrics in evaluating spinal kinematics: range of motion and helical axes of motion (or instantaneous axis of rotation). The lumbar spine undergoes motion in multiple directions, much of them coupled between: flexion/extension, right & left lateral bending, and right & left axial rotation (Figure 2.5), and likely undergo an infinite number of different motion paths throughout everyday activities.

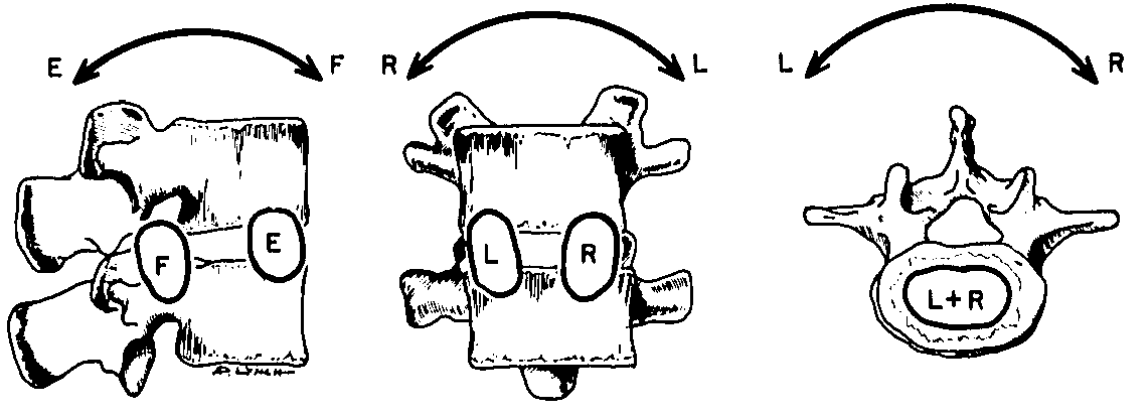


Figure 2.5. Bending Directions of the Lumbar Spine.

The structures of the lumbar spine permit motion in all three bending directions: Flexion/Extension (left), Lateral Bending (middle), and Axial Rotation (right). Each figure has its estimated center of rotation in each bending direction illustrated between the vertebral bodies (reprinted with permission)⁶

During flexion, extension, and lateral bending the portion of the disc closest to the direction of motion is in compression, while the opposite side is in tension (Figure 2.6). Axial rotation places the entire exterior portion of the annulus fibrosis in torsional tension. During bending activities the nucleus pulposus acts similar to a pivot point, but due to its high water content and viscoelastic material properties it also has the ability to deform and shift within the disc away from the direction of motion^{13,14}. Therefore, the mechanical integrity of the intervertebral disc directly affects the kinematics of the spine. It is important to note that the disc alone is not responsible for all of the motion patterns and ranges of motion. Facet joints, ligaments, and muscles can affect *in vivo* lumbar motion, but of these the intervertebral disc has the greatest effect on lumbar kinematics.

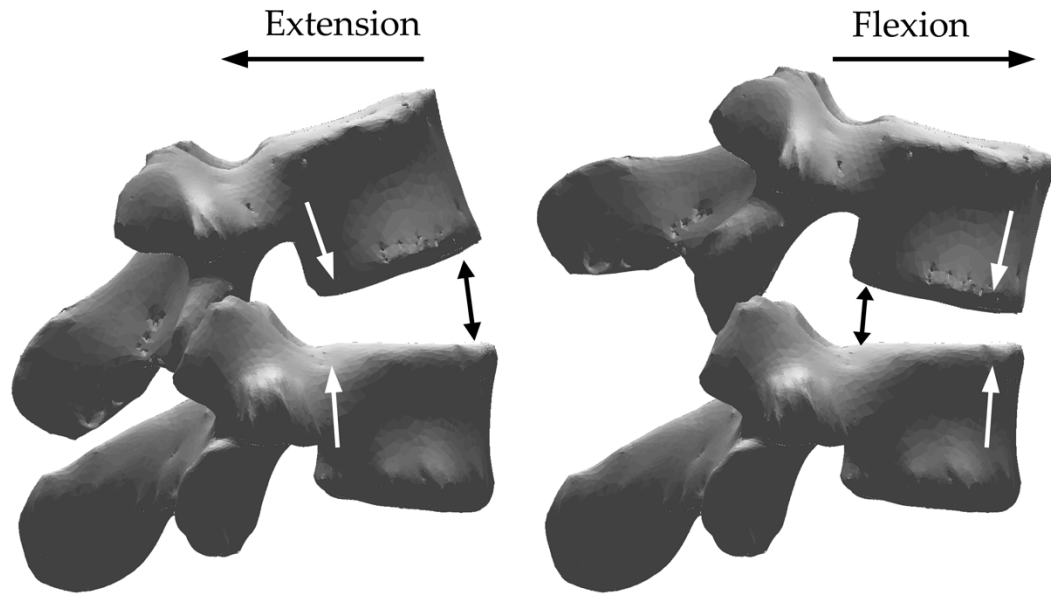


Figure 2.6. Force Distribution During Bending.
Flexion, extension, and lateral bending the portion of the disc closest to the direction of bending is in compression, while the opposite side is in tension (adapted from White and Panjabi)¹¹.

2.3.1 RANGE OF MOTION AND NEUTRAL ZONE

The physiologic range of intervertebral rotation measured from neutral position to the extreme position in any direction is defined as range of motion (ROM)¹¹. The primary direction of motion of the lumbar spine is flexion/extension, which occurs mainly in the sagittal plane. Lateral bending and axial rotation are also permitted in the lumbar segments and often are coupled, where motion occurring about one axis induces rotation about another axis. There have been many papers that have reported lumbar spine range of motion. Table 2.1 shows the limits and representative angles for each functional unit of the lumbar spine.

Table 2.1. Literature Reported Ranges of Motion and Representative Angles (degrees)¹¹

	Flexion/ Extension		Lateral Bending		Axial Rotation	
	Range	Mean Angle	Range	Mean Angle	Range	Mean Angle
L1-L2	5-16	12	3-8	6	1-3	2
L2-L3	8-18	14	3-10	6	1-3	2
L3-L4	6-17	15	4-12	8	1-3	2
L4-L5	9-21	16	3-9	6	1-3	2
L5-S1	10-24	17	2-6	3	0-2	1

The neutral zone (NZ) is the part of the range of physiologic intervertebral motion, measured from neutral position, within which the spinal motion is produced with minimal resistance¹⁵. In other words, the NZ is the angular change between the loading and unloading curve when there is no moment applied to the construct. Neutral zone, or the ratio of neutral zone to range of motion (NZR), is often used as a relative metric for defining spinal stability¹⁵. The larger the ratio, the larger the portion the NZ encompasses of the entire ROM, which suggests an increase in joint laxity or decreased stability. Table 2.2 displays representative values for the neutral zone and neutral zone ratio.

Table 2.2. Literature Reported Neutral Zone (degrees), Ranges of Motion (degrees), and Neutral Zone Ratio (%)¹⁵

	Flexion			Extension			Lateral Bending			Axial Rotation		
	NZ	ROM	NZR	NZ	ROM	NZR	NZ	ROM	NZR	NZ	ROM	NZR
Lumbar	1.5	7.6	19.7	1.5	3.8	39.5	1.6	6.6	24.2	0.7	2.4	29.2
L5-S1	3.0	10	30.0	3.0	7.8	38.5	1.8	5.5	32.7	0.4	1.4	28.6

2.3.2 HELICAL AXES OF MOTION AND INSTANTANEOUS AXIS OF ROTATION

The range of motion and neutral zone are scalars, which define kinematic endpoints, however the spine can move in infinite pathways of motion to reach those endpoints. In describing the health of the spine, it may also be pertinent to describe the pathway of

motion one vertebra takes with respect to another. The helical axis (HA) is a useful instrument to visualize and analyze the motion one rigid body takes while rotating about another body. The helical axis vectors describe the location and direction of the axes, as well as the magnitude of translation along that axis. The helical axis of motion allows analysis of the complete, precise three-dimensional motion for bodies that encounter both rotation and translation. A more thorough description of the helical axis methodology is found in Section 4.2.6. The instantaneous axis of rotation (IAR) simplifies this motion into a planar or two-dimensional equivalent to the helical axis; however, this simplification contains less information for describing a complex series of events. It should be mentioned that due to the strong coupling nature during lateral bending and axial rotation, motion of the lumbar spine is truly three-dimensional, and providing information only regarding the IAR is insufficient for describing spinal kinematics. Figure 2.7 displays the position and orientation of helical axes in a healthy, theoretically developed finite element spine model¹⁶.

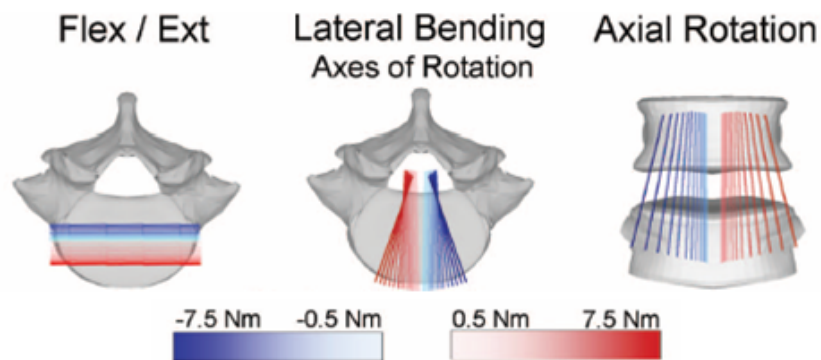


Figure 2.7. Theoretical Helical Axes in the Lumbar Spine. These axes were developed in a finite element model and are estimations based on the shape and interactions of the elements of the lumbar spine when a pure moment is applied superiorly (reprinted with permission)¹⁶.

2.4 INTERVERTEBRAL DISC DEGENERATION

Degeneration of the intervertebral disc is a progressive phenomenon that occurs in response to age, injury, pathology, or more likely a combination of these. Increased or abnormal mechanical loading leads to alterations in the discs' biochemical composition. The degeneration process of the disc typically begins in the nucleus pulposus (NP) with the breakdown of hydrophilic proteoglycans^{9,17}. This leads to a loss of hydration resulting in a decrease in the hydrostatic pressure, as well as the compressive residual stress and strain of the disc¹⁸⁻²¹. Later stages of degeneration include modification in collagen synthesis and degradation and eventually disc collapse. Altogether, the degradation in biochemical content affects the mechanical response and structural integrity of the disc.

The intervertebral disc is the largest avascular tissue in the body, and therefore even minor alterations in the competency of the tissue may lead to long-term difficulties in healing. These changes lead to diminished mechanical competency resulting in the discs' inability to maintain its structure and function potentially causing discogenic pain or pain due to cord occlusion, neural compressive lesions, or nerve root pinching, from altered spinal stability. Noninvasive evaluation of the biochemical content of the intervertebral disc potentially has a profound impact on the assessment of degeneration and it is of critical interest to detect these changes early in the degeneration process in order to cease the progression with the development of new biologic treatments and other therapeutics.

2.4.1 MORPHOLOGICAL CHANGES

The classical T2 weighted sagittal MRI has been studied and its features defined to produce subjective grading systems, which identify the health of the disc^{22,23}. These disc

health scores are used in the clinical decision making process and yet they lack a high degree of specificity^{24,25}. The Pfirrmann grading system produces a score from 1-5 based upon the MRI signal intensity, clarity of the transition zone between the annulus fibrosus (AF) and nucleus pulposus (NP), and disc height²². The Pfirrmann score is based on the following criteria (Figure 2.8):

Grade I- The structure of the disc is homogeneous, with a bright hyper-intense white signal intensity and a normal disc height.

Grade II- the structure of the disc is inhomogeneous, with a hyper-intense white signal. The distinction between nucleus and annulus is clear, and the disc height is normal, with or without horizontal gray bands.

Grade III- The structure of the disc is inhomogeneous, with intermediate gray signal intensity. The distinction between nucleus and annulus is unclear, and the disc height is normal or slightly decreased.

Grade IV- The structure of the disc is inhomogeneous, with a hypo-intense dark gray signal intensity. The distinction between nucleus and annulus is lost, and the disc height is normal or moderately decreased.

Grade V- The structure of the disc is inhomogeneous, with a hypo-intense black signal intensity²².

This subjective scoring system largely fails to correlate well with pain or provide clinically useful patient stratification, especially in detecting early signs of degeneration²⁶⁻²⁹.

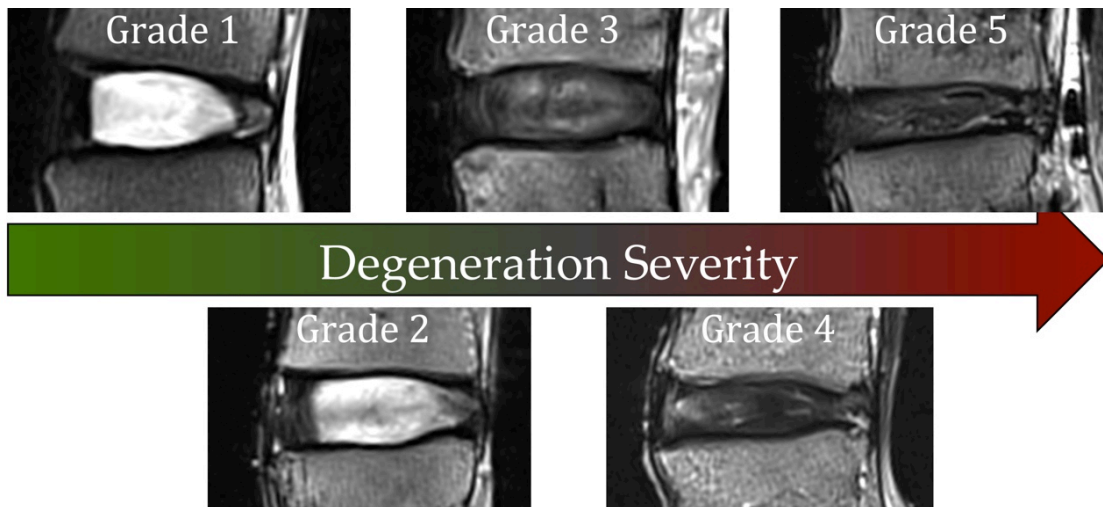


Figure 2.8. Pfirrmann Grading System.

Grades (1-5) are assessed based on the health of the intervertebral disc using T2-weighted magnetic resonance imaging. Grades are based on signal intensity and homogeneity of the nucleus pulposus, distinction between the nucleus and annulus, and disc height.

Other MRI methods have also been utilized to evaluate the health of the disc; some evaluate morphology and others interrogate the biochemical content. Direct measurement of the discs' biochemical content is not possible *in vivo*; therefore magnetic resonance imaging (MRI) is used to evaluate disc health. New quantitative MRI techniques are being developed to overcome the subjectivity in determining tissue health. These techniques include T1 ρ , chemical exchange saturation transfer (CEST), dGEMRIC, Sodium Imaging, magnetic transfer, T2 mapping, and T2* mapping³⁰⁻³⁵. These have largely been utilized for studying articular cartilage. The following techniques have been applied to the intervertebral disc and utilize the physics of water molecule relaxation within a magnetic field to produce images, which highlight the presence of proteoglycans (T1 ρ), hydration level (T2), and structure of the macromolecular network in combination with hydration level (T2*)^{30,31,36}.

Previous studies have aimed to determine the relationship between proteoglycan content of the disc and imaging parameters from various MRI techniques, such as T2 mapping, T1, and T1 ρ . Marinelli et al. did not find a correlation between T2 relaxation time and proteoglycan content in the nucleus pulposus ($r=0.73$; $p=0.06$) and the annulus fibrosus ($r=0.45$; $p=0.21$), however the NP did show a trend approaching significance³⁷.

Weidenbaum et al. also reported a lack of significant correlation between $1/T2$ and proteoglycan content³⁸. Each of these studies did report a significant correlation between T2 and water content^{37,38}. Terri et al. and Benneker et al. both found a significant relationship between T2 values and water and proteoglycan content^{39,40}.

Johannessen et al. reported a correlation coefficient of $r=0.67$ ($p<0.01$) between T1 ρ value and s-GAG per dry weight in non-degenerative discs with a Pfirrmann grade of 3.5 or less⁴¹. They also found a significant correlation between T1 ρ and water content. Other studies have also established the relationship between T1 ρ and proteoglycans in both articular cartilage and the disc⁴²⁻⁴⁴. Nguyen et al. aimed to evaluate the functionality of T1 ρ in more degenerative discs and determine the relationship between T1 ρ values and the mechanics of the NP⁴⁵. The previous relationships with proteoglycans ($r=0.69$; $p<0.05$) and water content ($r=0.53$; $p<0.05$) were confirmed, but were not significant when corrected for the intercorrelations within the same spine. They did find a significant correlation with the swelling pressure ($r=0.59$; $p<0.05$) of the NP.

Quantitative T2* (T2 star) is a multi-echo gradient-echo technique, rather than a multi-echo spin-echo technique of traditional T2 mapping. This provides the added benefit of a short acquisition time, high signal-to-noise ratio, three-dimensionality, and retains the ease of implementation on a clinical scanner^{31,46,47}. Also, other than T2 mapping, T2* is

the only sequence listed above that is FDA approved and is available on clinical scanners of all vendors. Traditional T2 mapping has been shown to correlate with hydration, but to a lesser degree with proteoglycan and collagen concentration and organization^{37,38,40}. T2* relaxation times provide information regarding the biochemical properties of the tissue, specifically interrogating water mobility within the macromolecular network, and has been shown to be beneficial in cartilage imaging^{31,36,46-54}. T2* relaxation is a combination of inherent “true” T2 relaxation and additional relaxation due to magnetic inhomogeneity, on both a microscopic and macroscopic scale ($1/T2^* = 1/T2 + 1/T2'$, where T2' is the relaxation due to magnetic field inhomogeneities)⁵⁵. While T2* is affected by bulk inhomogeneities in the magnetic field, which are typically not of interest, it is also affected by the differences in tissue composition at microscopic level, such as the change from cartilage to bone, annulus to nucleus pulposus or susceptibility-induced changes related to para- or diamagnetic depositions within the disc⁵⁵.

Recent studies have expanded T2* imaging to the intervertebral disc. Hoppe et al. proposed a technique for assessment of disc degeneration using axial T2* maps based on Watanabe et al. classification and found a significant correlation between T2* parameters and Pfirrmann grades^{56,57}. Welsch et al. correlated quantitative T2 and T2* relaxation times with Pfirrmann Score in patients suffering from low back pain⁴⁶. They reported both techniques correlated strongly with Pfirrmann Score regarding the nucleus pulposus, but T2* alone had the ability to identify changes in the posterior annulus fibrosus. They also performed a parametric analysis between T2* relaxation times at different regions of interest (ROI) and reported the highest spatial variation from AF to NP in Pfirrmann grade 1, and a decline at higher grades.

These T2* seminal works provide the basis for our investigation which aims to utilize the quantitative nature of the imaging technique and distinguish critical features of the Pfirrmann grading system. The features of the Pfirrmann grading system include disc signal intensity and clarity of the transition zone between the AF and NP. The interrogation of these features using the T2* images will enable the quantitative grading of disc degeneration without subjectivity or bias but with clinically recognized features of distinction. These efforts utilized ROI data alone to quantify disc health despite knowing that specific features of classification systems enable those systems to predict morphological changes better than others. Although T2* has been shown to be correlated with disc degeneration, the relationship between T2* relaxation times and the intervertebral disc constituents has yet to be established.

2.4.2 BIOCHEMICAL CHANGES

The etiology—initiation and progression being of mechanical or biological origin—of disc degeneration is unknown. Thus, monitoring the alterations in ultrastructural biochemistry can lead to an enhanced understanding of the biological response of the disc throughout degeneration. These biochemical changes primarily affect the structural collagen and proteoglycans in the AF and NP.

2.4.2.1 *Proteoglycans*

The abundance of proteoglycans in the NP region of the disc plays a vital role in hydration of the tissue. Proteoglycans are negatively charged and therefore are hydrophilic by nature. This hydrophilicity gives rise to the disc's internal osmotic

pressure, which is essential in distributing loads in the IVD. The unique interaction between the hydrated NP, which bulges under a compressive load, and the AF, which is primarily loaded in tension, affords the spine with its distinctive motion. The degeneration process typically begins in the NP with the breakdown of proteoglycans, which leads to decreased water content^{9,58,59}. Aggrecan is the most abundant proteoglycan found in the disc, and therefore is the primary source of degradation⁹. This change in structure affects the interaction between the NP and AF, resulting in a diminished ability to properly absorb loads.

2.4.2.2 *Collagen*

Later stages of degeneration include modification in collagen synthesis and degradation, although the changes are not as pronounced as the alterations in proteoglycans. The AF in a healthy tissue is primarily composed of highly organized Type I collagen fibers. Throughout degeneration, catabolic activity of Type I collagen increases and there is an upregulation of anabolic activity for Type II collagen^{9,17,60}. However, the total amount of collagen does not change; there is just a shift in relative production⁹. Other collagen types also encounter similar changes in synthesis, but are minor in comparison^{8,61}. These minor degradation changes are observed in the NP. This alteration in content leads to a less organized structure, which impacts the mechanical strength of the tissue, specifically in tension. The modification leads to altered disc mechanics and motion of the spinal unit as a whole. The end stages of disc degeneration eventually result in disc collapse due to a loss of protein structural integrity.

Although the bulk of the biochemical changes in the disc associated with degeneration are quite understood, the direct measurement of these properties is not available *in vivo*. Therefore, the development of new imaging modalities and mechanical assessment may be able to predict these changes *in vivo*.

2.4.3 TISSUE MECHANICAL CHANGES

The previously mentioned changes associated with disc degeneration give reason to suspect that the mechanical properties of the disc are also altered, which is the case. Previous studies have examined changes in the compressive moduli of the IVD with respect to degeneration severity through the use of confined compression or disc excision techniques^{21,62-65}. Johannessen et al. examined human disc samples in confined compression and reported a decrease in aggregate modulus of the NP with from $1.01 \pm 0.43 \text{MPa}$, for healthy discs, to $0.44 \pm 0.19 \text{MPa}$, for degenerated discs²¹. Using similar techniques, Iatradis et al.^{63,66} concluded that both the compressive and shear moduli of the AF increase with worsening degeneration.

One study aimed to quantify spatially based compressive mechanical properties at 10mm increments across the entire surface of the disc⁶⁵. Direct indentation was performed following complete excision of the entire disc. The elastic modulus was symmetric about the mid-sagittal plane. The NP displayed lower moduli than the annular regions. Also, the anterior and posterior AF moduli were significantly higher than the lateral AF regions. Degenerative changes were only determined in the anterior and posterior regions, where a significant reduction in moduli was observed. This indentation technique involves the removal of the cartilaginous endplate, which is highly interwoven with the fibers of the

disc (Figure 2.9). This causes disruption of the orientation of the annular fibers in the vertical direction⁶⁷. Thus, removal of the endplate prevents precise quantification of *in situ* mechanical properties of the native IVD.

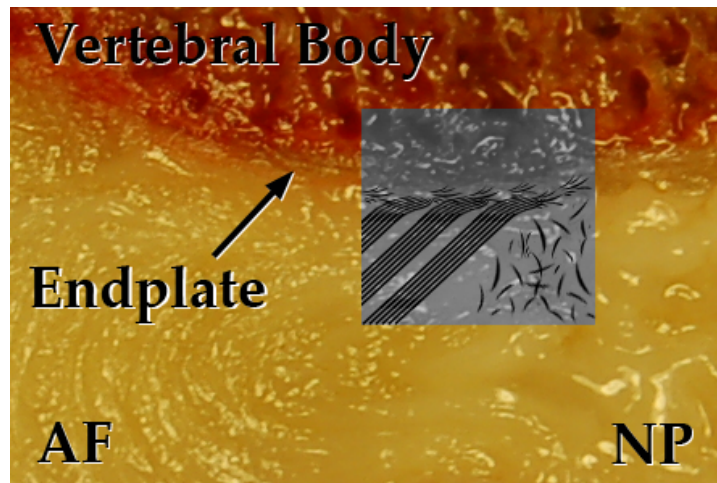


Figure 2.9. Fiber interactions between disc and cartilaginous endplate. The fibers of the disc are highly interwoven with the cartilaginous endplate and removal of this endplate disrupts the orientation of the AF fibers below. The newly developed technique leaves this interaction to quantify the compressive mechanics of the underlying disc. Adapted from *Journal of Orthopaedic Research* 1993;11:747-757 (reprinted with permission)²⁰.

For these reasons, a new technique was developed where the rigid porous endplate provides a boundary connection to the indenter to facilitate hybrid confined / *in situ* indentation loading²⁰. This technique does not destroy the interface between the cartilaginous endplate and the fibers of the disc and allows for the quantification of the residual stresses and strains on the tissue at different regions of the disc. This residual stress was found to be significantly lower in both ‘moderate’ and ‘severely’ degenerated discs when compared to the ‘healthy’ group in all locations ($p < 0.016$). Adams et al. reported a decrease in the hydrostatic pressure and others have observed a decrease in the swelling pressure with age and degeneration^{21,45,68}. The extent of strain following release of the endplate progressively decreased with degeneration severity in the NP (posterior

site), significant differences were found between the 'healthy' and 'severe' degeneration groups ($p < 0.037$). The AF locations demonstrated non-significant differences in excised strain. Similar to the other studies the modulus in the NP decreased significantly from healthy to severe ($p = 0.038$), however no change was observed in the annular regions.

Similar trends were observed regarding a decrease in the NP moduli with degeneration and an increase in the AF moduli with degeneration. The moduli values obtained in the present study are larger than the direct indentation method. The values are in the megapascal range, but not quite as high as the values reported using the traditional confined compression methods. Our methodology utilizes the disc's native boundary conditions and the cartilaginous endplate as our porous indenter. Since the confined compression chamber prevents the IVD from expanding inferiorly and radially, it would be expected to produce higher moduli than a tissue that is allowed to expand. Conversely, the direct indentation method allows expansion, but due to the excision from the endplate, the annular fibers are allowed to spread out and lose orientation, producing lower modulus values.

The viscoelastic response of the disc varies with the degree of degeneration as well as regionally. The short time constant, τ_s , increases in the AF with degeneration, but is not altered in the NP. In the NP, the long time constant, τ_L , decreased significantly with degeneration, but increased with severity of degeneration in the anterior AF. O'Connell et al. also noted a significant increase in the long time constant with worsening degeneration when performing compressive creep tests on whole disc motion segments⁶⁹. These results indicate that perhaps the AF is responsible for the discs' fast response, while the NP may play a minor role.

The stress-relaxation curves, fit parameters, and peak force response of the intervertebral disc allude that severely degenerated discs have a greater inability to maintain force, both in the NP and AF. As shown in Figure 2.10, the percent relaxation rate is the greatest in the ‘severe’ degeneration group, whereas healthier tissues resist load decay better. The ratio of force over time to the final equilibrium force displays how well the tissue is able to maintain loads under constant strain. For example, if the ratio were one, the lowest possible, this would mean that the force imposed did not change throughout the allotted stress-relaxation time, and thus the tissue has a greater ability to sustain loads than a tissue with a higher ratio. Discs showcasing a presence of severe degeneration had a higher ratio than healthy discs. Healthy discs encounter higher forces at the same strain level, and are able to maintain this force, where degenerated discs are unable to maintain this force.

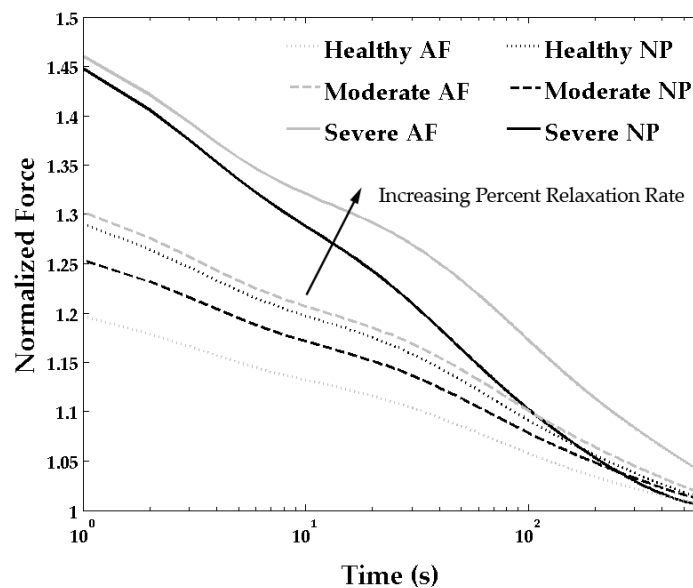


Figure 2.10. Average Relaxation Curves Showing Percent Relaxation Rate.

The percent relaxation rate in severely degenerated disc is higher than healthier tissue, both in the NP and AF. A degenerated disc, under the same constant strain, will relax to equilibrium faster and that percent change in force is greater than in healthier tissue (reprinted with permission)²⁰.

While phenomenologically this is well understood, the relationship between these local biomechanical changes and altered global mechanics are unknown.

2.4.4 FUNCTIONAL MECHANICAL CHANGES

The primary path of load transfer in the lumbar spine is through the intervertebral disc, with only a very small portion of the loads being transferred through the facet joints⁷⁰.

This suggests that the health of the disc, affecting both the biochemical composition and mechanical properties, primarily dictates the quality of motion of the lumbar spine.

Previous studies have reported a decrease in range of motion for both flexion and lateral bending, while axial rotation increased with degeneration⁷¹⁻⁷⁵. Mimura et al. reported an increase in the NZR for flexion-extension, lateral bending, and axial rotation with disc degeneration⁷⁴. Other studies support the Kirkaldy-Willis and Farfan hypothesis that there are three stages to spinal instability (1) temporary dysfunction, (2) unstable phase, and (3) stabilization; where there is an increase in ROM, followed by a decrease at the very end stages of degeneration^{75,76}. Likely the formation of osteophytes at the end stages of degeneration is the primary reason for the increased stability and fully bridged osteophytes. Other differences that could explain the varying results are in the evaluation of disc health, where some used MRI based methods and others used radiographic or macroscopic, dissection based, grading. The literature also suggests an increase in the bending stiffness of both lateral bending and flexion with degeneration⁷⁷. Where the range of motion has shown been to increase in axial rotation with degeneration, and the bending stiffness decreases⁷⁸.

The instantaneous axis of rotation has been shown to migrate in the degenerative discs^{11,79-82}. This has been observed in both flexion-extension and lateral bending. No studies to my knowledge have quantified the helical axes of the spine as a function of disc health. The helical axis has been employed to analyze the difference in kinematics associated with disc replacement devices and has been suggested as a means to assess spinal stability by monitoring the location and out of plane axis rotations⁸³⁻⁸⁵. Also, patients with low back pain have been shown to exhibit larger out-of-plane motion during bending, thus reinforcing the need to analyze three-dimensional motion^{86,87}. Due to the uncertainty in the literature regarding the changes to ROM, further investigation of the pathway of motion may provide a more definitive answer to the kinematic changes associated with disc degeneration.

2.5 SUMMARY OF INTRODUCTION

Functional spine mechanics, local compressive mechanical properties, and biochemical composition of the disc have been shown to progress with disc degeneration severity. These changes provide sensitive and accurate predictors of progression. Unfortunately, measurement of these properties *in vivo* is currently not a viable option due to the invasiveness of the procedures. Therefore, an indirect method is needed to evaluate the multifarious characteristics of a patient's disc health. Of critical interest is the relationship that spinal functional mechanics has with the other morphologic, biochemical, and biomechanical properties that progress with intervertebral disc degeneration. These known relationships are the foundation of the hypothesis testing herein, where the ultimate goal is correlation with new imaging techniques to assess

morphologic changes and new analysis techniques to assess clinical functional mechanics.

3 CHAPTER 3: STUDY DESIGN AND SPECIFIC AIMS

The aim of this research program was to measure the properties of the intervertebral disc across the degeneration spectrum in an effort to identify potential predictors of disc degeneration. The functional mechanics of the lumbar spine was correlated with degenerative changes as measured from the discs' morphology, local biochemical content, and local mechanical properties.

3.1 STUDY DESIGN

An *in vitro*, correlational study design was utilized to examine the relationships between the factors of intervertebral disc: (i) morphology, (ii) local biochemistry, and (iii) local compressive biomechanics and the functional biomechanics of the lumbar spine.

These studies were conducted on eighteen (n=18) fresh frozen osteoligamentous cadaveric lumbar spine specimens (L3-S1) acquired from the University of Minnesota Bequest Program for experimental investigation. Correlational analyses between each functional spinal unit from L3 to S1 were conducted to investigate the relationship between disc morphology as measured by MRI and functional biomechanics. Further investigation of the L4-L5 level was executed in a factorial fashion to define the relationships between MRI calculated disc morphology and regional biochemistry and regional compressive biomechanics. More in-depth analysis, including three-dimensional helical axes, was performed at the L4-L5 level to quantify the precise pathway of motion undergone during bending activities (flexion, extension, lateral bending, and axial rotation). The correlative strength of these helical axis parameters was then assessed with

the parameters of disc morphology, biochemistry, and compressive biomechanics on specimens that spanned the degenerative spectrum.

3.2 SPECIFIC AIMS

My research objectives were to measure the functional biomechanics of lumbar spinal motion segments, as well as the helical axes of motion, using a human cadaveric model to establish factors associated with intervertebral disc degeneration that are distinguishable and correlated to functional motion. These factors include morphological MR images, regional compressive mechanical properties, and biochemical composition. Together, achievement of these goals lead to an enhanced mechanistic understanding of the degenerative intervertebral disc and the potential clinical utility of an *in vivo* kinematic disc health strategy. The pathway to achieving these goals is through the following specific aims (Figure 3.1):

SPECIFIC AIMS:

1. Measure the helical axis of motion and traditional spinal mechanics of the lumbar spine in a cadaveric model (L3-S1) as a function of disc degeneration health (Pfirrmann and T2* Parameters) in flexion, extension, lateral bending, and axial rotation.
2. Assess intervertebral disc health using a traditional clinical T2 weighted MRI and evaluate these features with quantitative T2* techniques. Quantify regional disc compressive biomechanical and biochemical properties as a function of disc

health. Proteoglycan, collagen, and water content of the nucleus pulposus and inner and outer annulus fibrosus were assayed and computed for these samples.

3. Develop the framework for a predictive model assessing the multiple factors measured above using clinically viable metrics, such as MRI and global spinal biomechanics, to predict disc health.

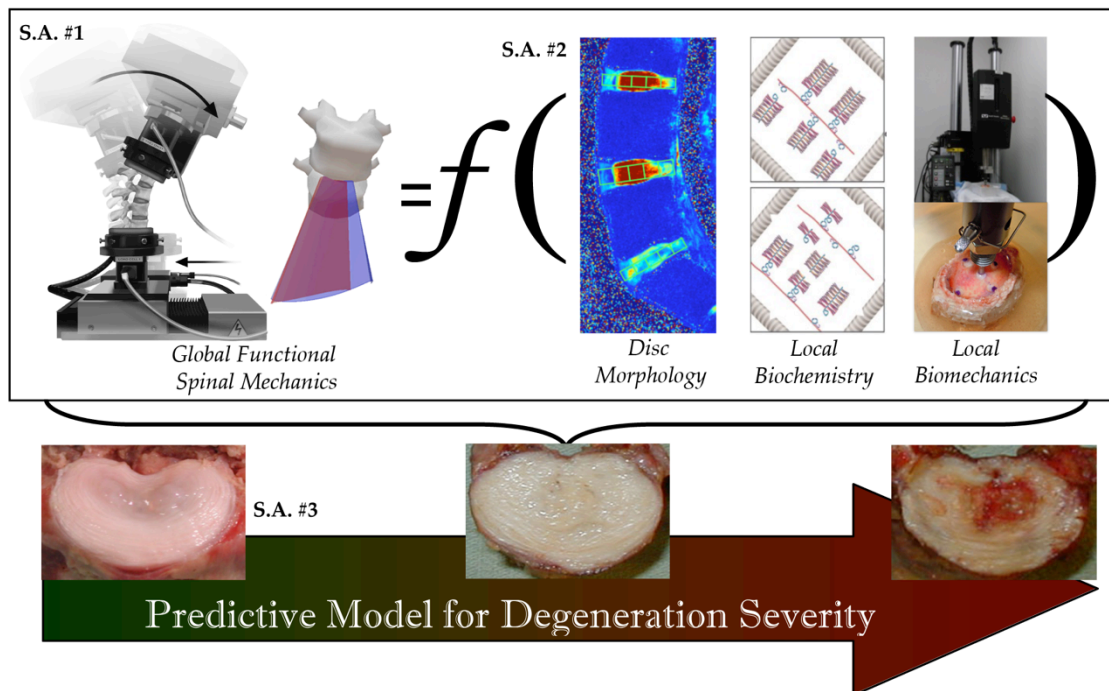


Figure 3.1. Specific Aims.

My research objectives are to measure the functional biomechanics of lumbar spinal motion segments [S.A. #1], as well as the helical axes of motion, using a human cadaveric model to establish factors associated with intervertebral disc degeneration [S.A. #2] that are distinguishable and correlated to functional motion; developing the framework for a predictive model for disc degeneration [S.A. #3].

Achievement of these aims provide the foundation for a clinically viable tool to predict spinal health based upon biomechanics, potentially enabling the stratification of the low back pain populace. Improved patient stratification can lead to treatment strategies, which

are targeted specifically for the morphology, biochemistry, and biomechanics of that patient.

3.3 HYPOTHESES

The hypotheses are structured such that the initial hypothesis examines the ability of the T2* MRI assessment system to predict the health of the disc. The next two hypotheses examine the relationships between the imaging, local biochemistry, and local biomechanics. The final hypotheses all examine the global spinal mechanics as they relate to the features of T2* MRI imaging, biochemistry, and local biomechanics. Taken as a whole, these hypotheses verify new methods in spinal measurements with prior techniques and propose a new biomechanics-centric approach to the evaluation of patients with disc degeneration.

Hypothesis 1: *Pfirrmann Grade is negatively correlated with the following quantitative T2* MR imaging parameters: a) the NP T2* relaxation time, b) transition zone slope between the NP and AF, and c) T2* signal intensity area of the coronal plane.*

Hypothesis 2: *The T2* relaxation time is correlated with the following site-specific biochemical properties: A) Glycosaminoglycan Content (positively), B) Hydroxyproline Content (negatively), and C) Water Content (positively), at the following regions: a) NP, b) inner lateral AF, c) outer lateral AF, d) anterior AF, and e) posterior AF.*

Hypothesis 3: *The T2* relaxation time is positively correlated with the following local compressive mechanical properties: A) residual stress and B) excised strain at the*

following regions: a) NP, b) inner lateral AF, c) outer lateral AF, d) anterior AF, and e) posterior AF.

Hypothesis 4: The range of motion in A) flexion, B) extension, and C) lateral bending is positively correlated with, and D) axial rotation is negatively correlated with T2* MR imaging parameters of disc health, including: a) NP T2* relaxation time, b) transition zone slope between the NP and AF, and c) T2* signal intensity area of the coronal plane.

Hypothesis 5: The neutral zone to range of motion ratio in A) flexion, B) extension, C) lateral bending and D) axial rotation negatively correlated with T2* MR imaging parameters of disc health, including: a) NP T2* relaxation time, b) transition zone slope between the NP and AF, and c) T2* signal intensity area of the coronal plane.

Hypothesis 6: The bending stiffness in A) flexion, B) extension, and C) lateral bending is negatively correlated with, and D) axial rotation positively correlated with T2* MR imaging parameters of disc health, including: a) NP T2* relaxation, b) transition zone slope between the NP and AF, and c) T2* signal intensity area of the coronal plane.

Hypothesis 7: The average primary orientation of the helical axis vector in A) flexion, B) extension, and C) lateral bending is positively correlated with T2* MR imaging parameters of disc health, including: a) NP T2* relaxation time) transition zone slope between the NP and AF, and c) T2* signal intensity area of the coronal plane.

Hypothesis 8: The standard deviation of the primary orientation of the helical axis vector in A) flexion, B) extension, and C) lateral bending is negatively correlated with T2* MR

imaging parameters of disc health, including: a) NP T2 relaxation, b) transition zone slope between the NP and AF, and c) T2* signal intensity area of the coronal plane.*

Hypothesis 9: *The average distance of the instantaneous axis of rotation from the origin in A) flexion, B) extension, and C) lateral bending is negatively correlated with T2* MR imaging parameters of disc health, including: a) NP T2* relaxation time, b) transition zone slope between the NP and AF, and c) T2* signal intensity area of the coronal plane.*

Hypothesis 10: *The standard deviation of the distance of the instantaneous axis of rotation from the origin in A) flexion, B) extension, and C) lateral bending are negatively correlated with T2* MR imaging parameters of disc health, including: a) NP T2* relaxation time, b) transition zone slope between the NP and AF, and c) T2* signal intensity area of the coronal plane.*

Hypothesis 11: *The A) bending stiffness, B) range of motion, and C) neutral zone to range of motion ratio in A) flexion, B) extension, C) lateral bending, and D) axial rotation are correlated with the a) residual stress, b) excised strain, c) sulfated-glycosaminoglycan content, and d) water content in the NP.*

Hypothesis 12: *The helical axis orientation and instantaneous axis of rotation location in A) flexion, B) extension, and C) lateral bending are significantly correlated to the a) residual stress, b) excised strain, c) sulfated-glycosaminoglycan content, and d) water content in the NP.*

4 CHAPTER 4: RESEARCH METHODS

Eighteen fresh frozen human cadaveric lumbar spines (L3-Sacrum) were obtained from the University of Minnesota Bequest program (age: 53.2 ± 15.5 years; range: 21-71 years; sex: 11 male, 7 female). Specimens were thawed to room temperature and examined for any bony abnormalities. Those displaying gross abnormalities, such as scoliosis or bridging osteophytes, were excluded from the study. This resulted in one specimen being excluded due to severe scoliosis. Included specimens had musculature and soft tissue, except for ligamentous structures and the intervertebral disc, removed prior to further investigation. Specimens were wrapped in a 0.9% saline solution filled chuck and stored in the freezer at -20°C until testing.

4.1 MAGNETIC RESONANCE IMAGING

All magnetic resonance imaging was performed using a clinical Siemens 3-Tesla scanner (Magnetom Trio; Siemens Healthcare). Sagittal slices of each specimen, composed of three intervertebral discs each (L3-L4, L4-L5, L5-S1) 54 discs in total, were acquired using traditional T2 weighed and quantitative T2* MRI techniques. T2 and T2* imaging protocols followed standard techniques and were implemented on the same 3-T scanner at the Center for Magnetic Resonance Research for consistency. Figure 4.1 displays two specimens, one healthy and one degenerative, utilizing T2 weighted and T2* weighted MRI.

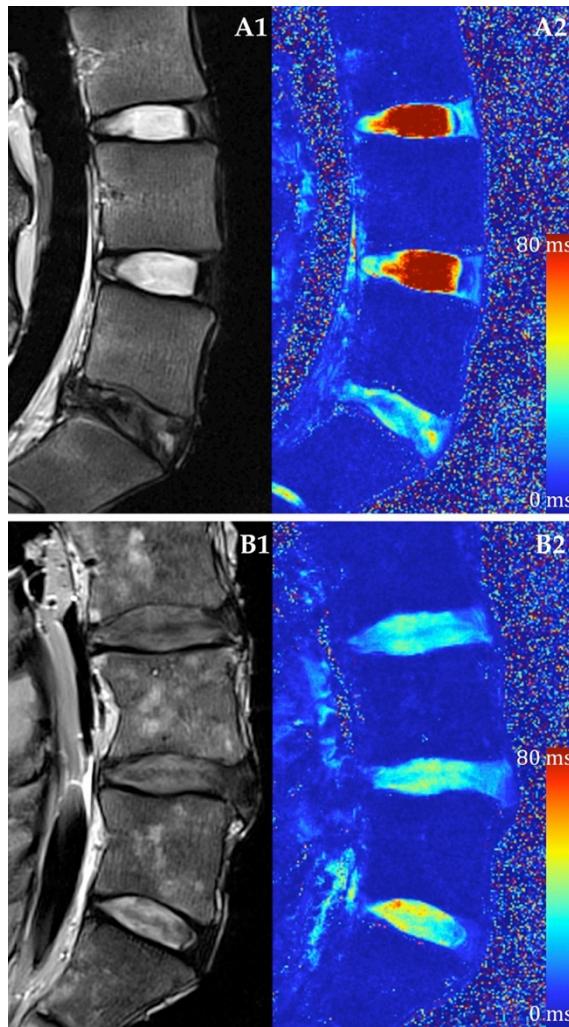


Figure 4.1. Conventional T2 weighted and T2* Mapping MRI.
 Healthy lumbar intervertebral discs (A) and degenerated discs (B) imaged using a conventional T2 imaging sequence (1) and quantitative T2* mapping techniques (2).

4.1.1 TRADITIONAL T2 WEIGHTED MAGNETIC RESONANCE IMAGING

Conventional T2-weighted sagittal images were acquired to estimate disc health based on the Pfirrmann disc grading scheme (Figure 2.8). Each disc was graded via the Pfirrmann scale independently by seven spine surgeons and three experienced spine researchers. These scores were then averaged and rounded to the nearest integer.

4.1.2 QUANTITATIVE T2* MAGNETIC RESONANCE IMAGING

Quantitative T2* magnetic resonance images were acquired [TR (ms): 500; TE (ms): 4.18, 11.32, 18.46, 25.60, 32.74, 39.88; Voxel Size (mm): 0.5x0.5x3.0, Slices: 33]^{30,56}.

Quantitative T2* maps were calculated (MapIt, Siemens Healthcare), (Figure 4.1 A2-B2), by fitting the signal intensity (S) value, pixel-by-pixel, obtained for each echo time to an exponential decay function Equation 1, where T2* is the relaxation coefficient (Figure 4.2).

Equation 1

$$S(t) = e^{-t/T2^*}$$

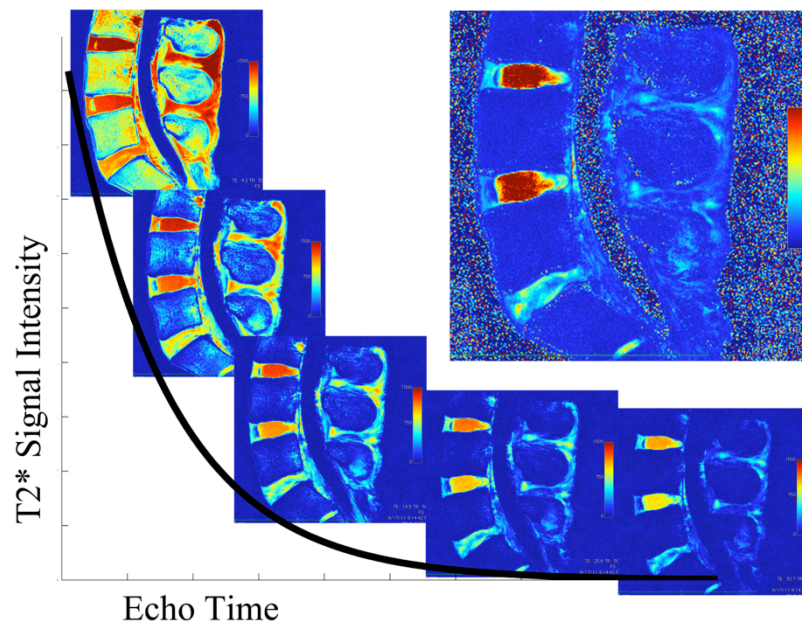


Figure 4.2. Quantitative T2* MRI Mapping.

Quantitative T2* maps were calculated by fitting the signal intensity (S) value, pixel-by-pixel, obtained for each echo time to an exponential decay function **Equation 1**, where T2* is the relaxation coefficient. T2* Relaxation times are then compiled to create a map, upper right.

The quantitative T2* maps represent the relaxation coefficient of the exponential decay fit of the signal intensity for a pixel across the echo times.

4.1.3 IMAGING ANALYSIS

Using the created T2* maps, the average T2* values were recorded using the open-source Osirix Imaging Software across five mid-sagittal plane regions of interest (ROI) from anterior (ROI 1) to posterior (ROI 5) (Figure 4.3). Further analysis utilizing MATLAB (Mathworks Inc. Natick, MA), evaluated the central ROI (ROI 3) mean relaxation value in all sagittal slices across the coronal plane as the intensity changed from lateral to medial to lateral. Using a least squares method, the slope of the transition zone (ms/mm) between the annulus fibrosus and nucleus pulposus on each side was linearly regressed and then averaged (Figure 4.4). The right and left sides were averaged to reveal a metric developed to quantify the distinction between the NP and AF. To quantify the signal intensity of the disc, another feature of the Pfirrmann grading system, the area underneath the curve was calculated by the trapezoidal integration method and normalized to the width of the IVD, measured on the MRI (Figure 4.5).

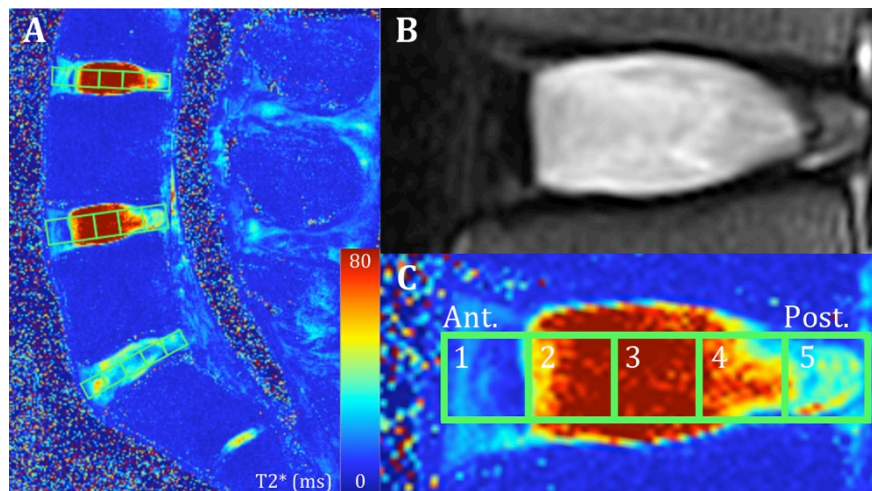


Figure 4.3. Magnetic Resonance Images of Lumbar Spine and Intervertebral Disc Using T2 and Quantitative T2* Techniques.

Left: T2* Map of Lumbar Spine. **Top Right:** Healthy Lumbar Intervertebral disc imaged with classical T2 MRI. **Bottom Right:** Same disc using T2* map showcasing the five regions of interest from anterior to posterior (1 to 5).

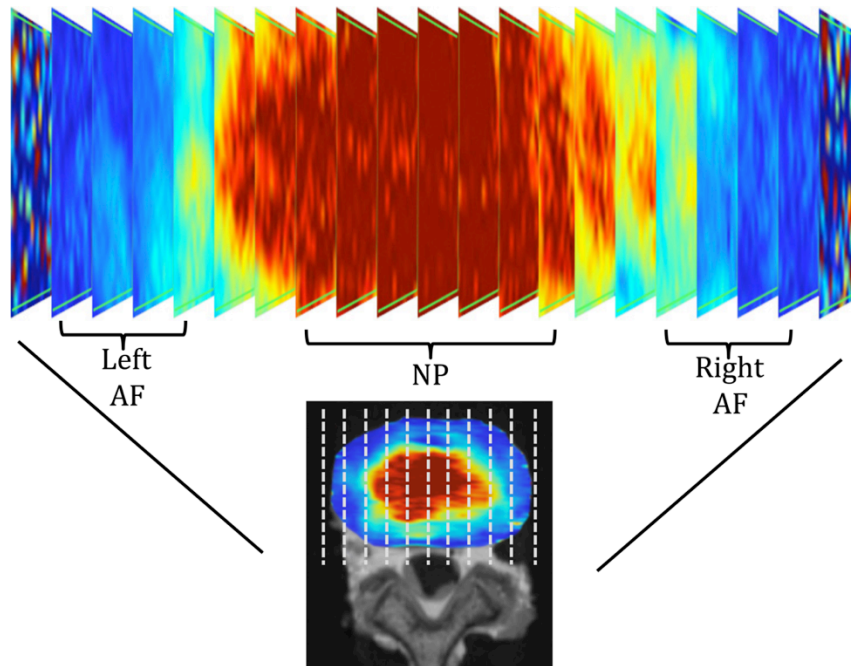


Figure 4.4. T2* Coronal Plane Profile of Mid-Sagittal Region of Interest.
 The mid-sagittal region of interest (ROI 3) T2* relaxation time was measured in each sagittal slice through the coronal plane of the disc.

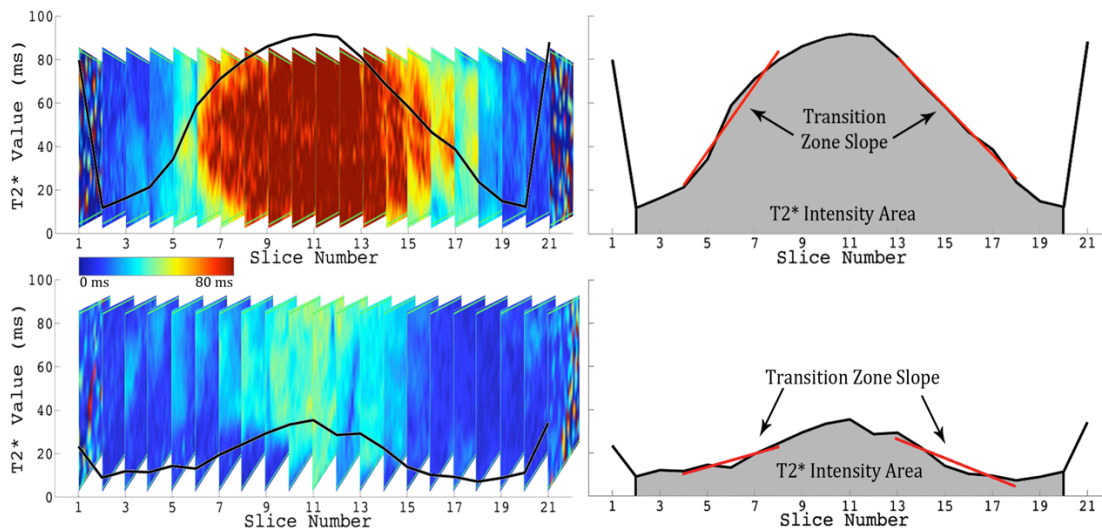


Figure 4.5. Quantification of Imaging Parameters, Transition Zone Slope and T2* Intensity Area, from T2* Relaxation Profile in the Coronal Plane of ROI 3.
Top Left: Coronal Profile of Healthy Disc with Plot of Average T2* Relaxation Time (ms) overlaid. **Top Right:** Corresponding quantification of Transition Zone Slope and T2* Intensity Area of the healthy disc. **Bottom Left:** Coronal Profile of Degenerated Disc with Plot of Average T2* Relaxation Time (ms) overlaid. **Bottom Right:** Corresponding quantification of Transition Zone Slope and T2* Intensity Area of degenerated disc.

For local regional comparisons with biochemical content and compressive biomechanics, five test sites were isolated across the transverse plane of the IVD and mean T2* relaxation times were recorded using Osirix Imaging Software at each region of interest (ROI). The sites, displayed in, included the center nucleus pulposus (NP) and four in the annulus fibrosus (AF), including three outer AF areas: anterior (aAF), posterior (pAF), and lateral (oAF), as well as one inner lateral region (iAF). The lateral test sites were randomized left or right based on a block design utilizing the Pfirrmann grade.

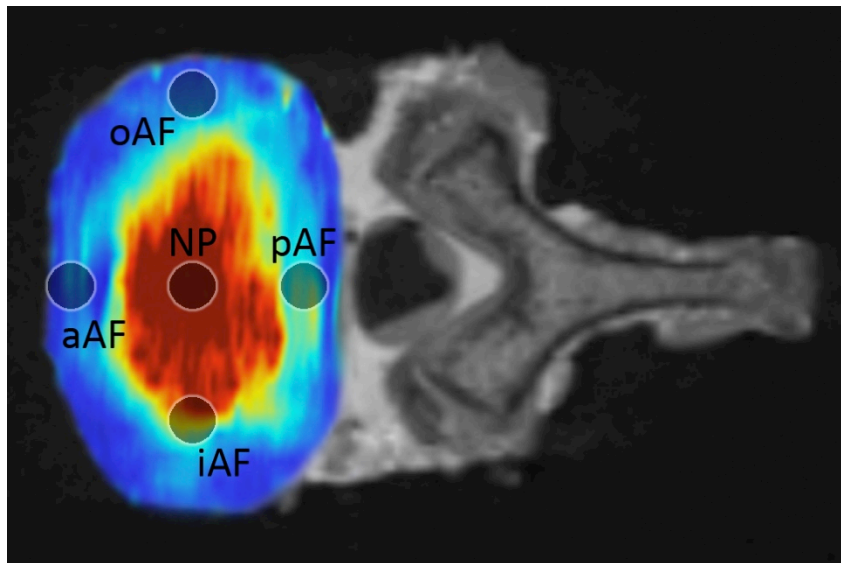


Figure 4.6. Intervertebral Disc Test Sites.

Locations are shown on a transverse slice of a quantitative T2 map. The average T2* relaxation time was measured at each region of interest. NP: nucleus pulposus, AF: annulus fibrosus, o: outer, i: inner, a: anterior, p: posterior*

4.1.4 SUMMARY OF IMAGING PARAMETERS

Table 4.1. Imaging Parameters (n=54)

Variable	Units	Range	Levels Tested	Description
Pfirschmann Grade	Unitless	1-5	L3-L4 L4-L5 L5-S1	Standard for Disc Health
T2* Relaxation Times AP ROI (1-5)	msec	8.8 - 93.3	L3-L4 L4-L5 L5-S1	Average T2* Relaxation Time
T2* Intensity Area	msec	14.5 – 54.6	L3-L4 L4-L5 L5-S1	Integrated ROI 3 Coronal Plane T2* Value
Transition Zone Slope	msec / mm	0.5 – 7.3	L3-L4 L4-L5 L5-S1	Linear Slope of T2* Value between NP and AF
T2* Health	Unitless	1-3	L3-L4 L4-L5 L5-S1	(ROI 3 T2*/Max T2*) + (T2* Intensity Area/Max T2* Intensity Area) + (Transition Zone Slope/Max Transition Zone Slope)
T2* Relaxation Times Transverse Plane (Specific Sites Chosen)	msec	9.1 – 91.6	L4-L5	Average T2* Relaxation time in NP, aAF, pAF, iAF, and oAF

4.2 FUNCTIONAL LUMBAR SPINE MECHANICS

The superior (L3) and inferior (Sacrum) vertebral bodies of each osteoligamentous lumbar spine were embedded in polymethylmethacrylate (PMMA), with screws inserted in the bodies of L3 and S1 first to allow for better purchase with the PMMA, in order to rigidly fix the specimen in the testing apparatus.

4.2.1 SPINE KINETIC SIMULATOR

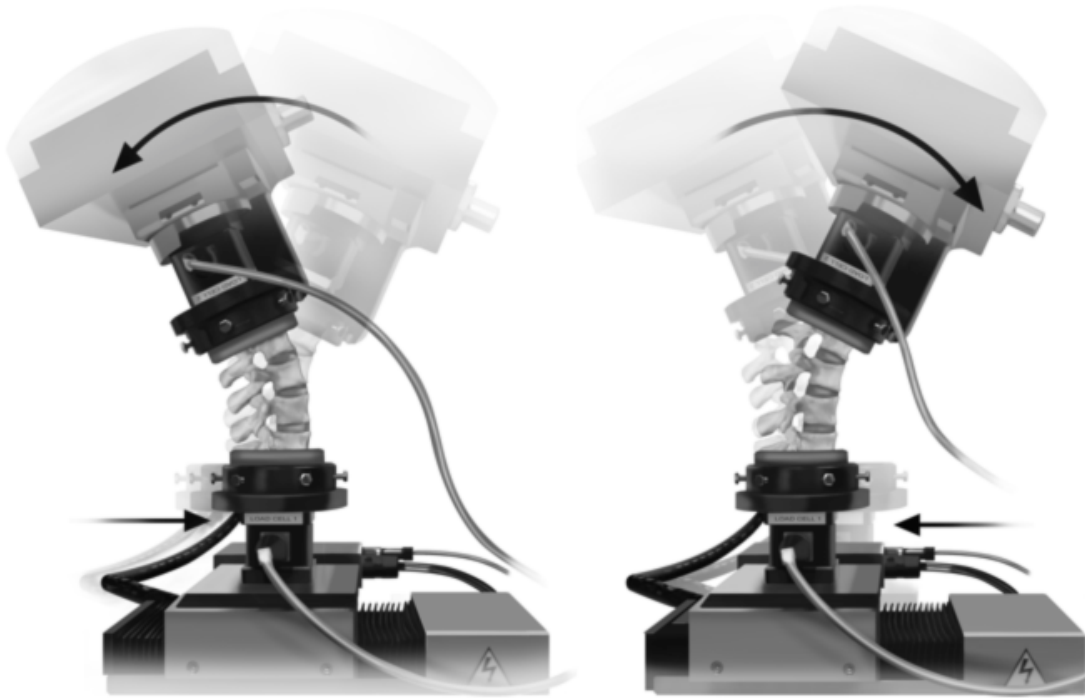


Figure 4.7. Illustration of the Spine Kinetic Simulator.

Left: Machine performing extension of the spine. **Right:** Machine performing flexion of the spine. Pure moment is applied superiorly, while allowing the inferior track to translate to minimize shear forces.

The Spine Kinetic Simulator (8821 Biopuls, Instron, Norwood, MA) is a six-axis servo-hydraulic testing apparatus capable of reproducing spinal motion for *in vitro* specimens by applying pure moments in all bending directions (Figure 4.7, Figure 4.8):

flexion/extension, left/right lateral bending, and left/right axial rotation⁸⁸. Pure moments can be created by applying a rotation to the superior vertebral body while allowing the inferior vertebra unconstrained movement on an X-Y table (resistance <0.1 N). Six-degree-of-freedom load cells (AMTI M4380, Watertown, MA) are attached the superior and inferior ends of the specimen to both measure and control the forces and moments through the specimen. The simulator employs a PIDF controller wherein feedback from

the digital encoders provides displacement data and the load cells provide force and moment data collected at 10,000 Hz. Fine control of this system facilitates the re-creation of the natural motion of the lumbar spine⁸⁹.

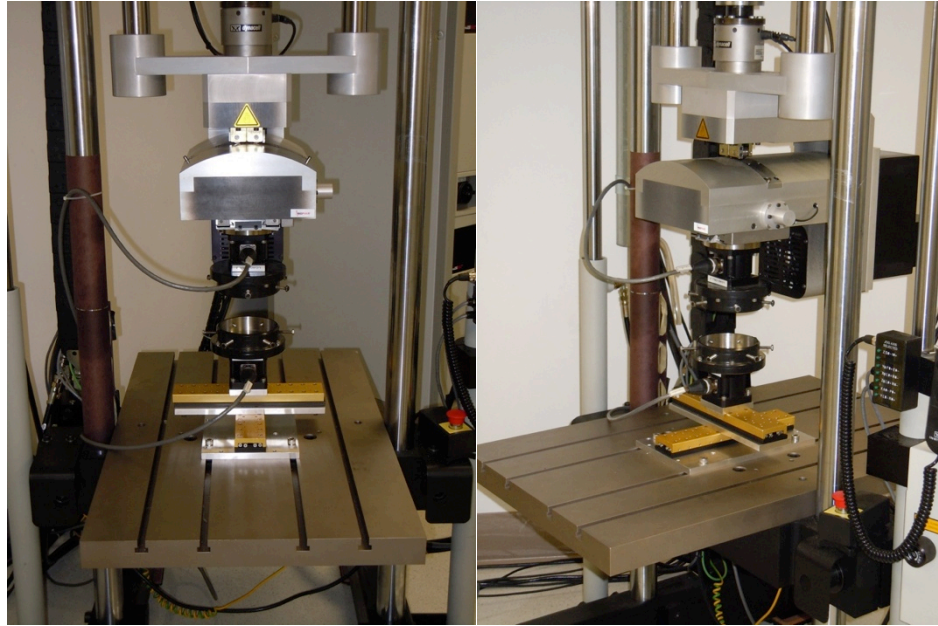


Figure 4.8. Image of Spine Kinetic Simulator.

Pure moment is applied superiorly, while allowing the inferior track to translate to minimize shear forces

4.2.2 OPTICAL MOTION CAPTURE SYSTEM

A 5-camera infrared motion capture system (Vicon MX-F40NIR, Vicon Motion Systems, Centennial, CO) allows for the quantification of orientation and position of each vertebral body in three dimensions throughout motion. Four passive infrared reflecting markers (flag with 4 non-collinear points) are attached to each vertebra (Figure 4.9A). Using a digitizing probe an internal coordinate system can be embedded into each of the vertebral bodies by digitizing three points. These positions are the superior anterior most point, which was defined as the origin, and the left and right lateral most points. The resultant

coordinate system is such that the x-axis oriented positively anterior, the y-axis positive left-lateral, and the z-axis perpendicular to the x-y plane with positive superior (Figure 4.9B). The vertebrae are tracked with 0.02 mm accuracy, determined by calibration parameters, over the calibrated volume for spinal motion within the simulator, and these data are collected at 100 Hz.

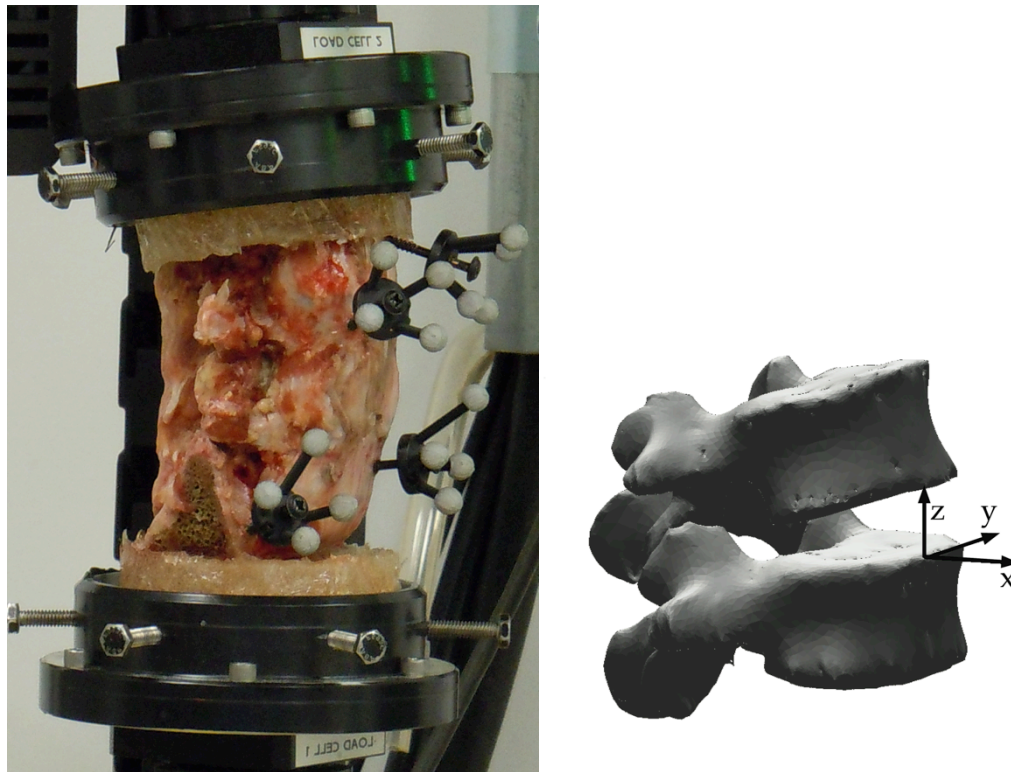


Figure 4.9. Specimen Loading in Spine Kinetic Simulator.

Left: Specimen with infrared marker set attached to each vertebral body. **Right:** Local coordinate system imbedded in vertebral body. X-axis oriented positively anterior; Y=axis positive left-lateral; and Z-axis positive superior.

4.2.3 TESTING PROCEDURE

Each specimen was carefully positioned in the center of the Spine Kinetic Simulator, while maintaining the natural lordosis of the unloaded lumbar spine. Once positioned, the load cells were balanced to zero. Preconditioning bending tests were performed in

flexion/extension, lateral bending, and axial rotation; including three cycles of $\pm 7\text{Nm}$ applied across each spinal construct in a pure moment fashion with an axial preload of 0 Nm. Moments were applied sinusoidally at 0.015 Hz, which is approximately 0.21 Nm/s. This was followed by an additional four loading cycles in each bending direction for data acquisition. The third cycle was used for data analysis. These force and moment data were collected on a 100 Hz DAQ system coupled with the controller of the Spine Kinetic Simulator (SKS). Load cells attached to the SKS provided the forces and moments at the superior and inferior ends of the construct, while the infrared Vicon cameras, in conjunction with the reflective marker set attached to each vertebral body, provide precise three-dimensional spatial information for each functional spinal unit. In order to synchronize the two data collection systems, the voltage of the axial channel of the Spine Kinetic Simulator was collected by both systems. Each collected curve was aligned using custom MATLAB code (Mathworks Inc. Natick, MA), such that the data was aligned within 0.01 seconds. The combination of these systems provides information regarding the forces, moments, translations, and rotations between each vertebral body, allowing for intersegmental mechanics to be computed.

4.2.4 FUNCTIONAL LUMBAR MECHANICAL OUTCOMES

All data was filtered using a fourth order low-pass Butterworth filter (cutoff 10 Hz). The intersegmental angular displacement vs. moment plots were constructed and traditional spine mechanics outcomes were computed for each functional spinal unit L3-L4, L4-L5, L5-S1 (Figure 4.10). These plots were based on the third, of four cycles of bending. From the angle-moment data the following outcome metrics were calculated: range of motion

(ROM), neutral zone (NZ), ratio of NZ-to-ROM (NZR), and bending stiffness (λ_1 , λ_2). ROM is defined as the maximum angular change between each direction of bending. NZ is the angular change between the loading and unloading curve when there is no moment applied to the construct. The bending stiffness was defined as the slope of the linear regression from the end range of motion step-wise backwards through the linear portion of the curve, until a minimum R^2 of 0.98 was reached.

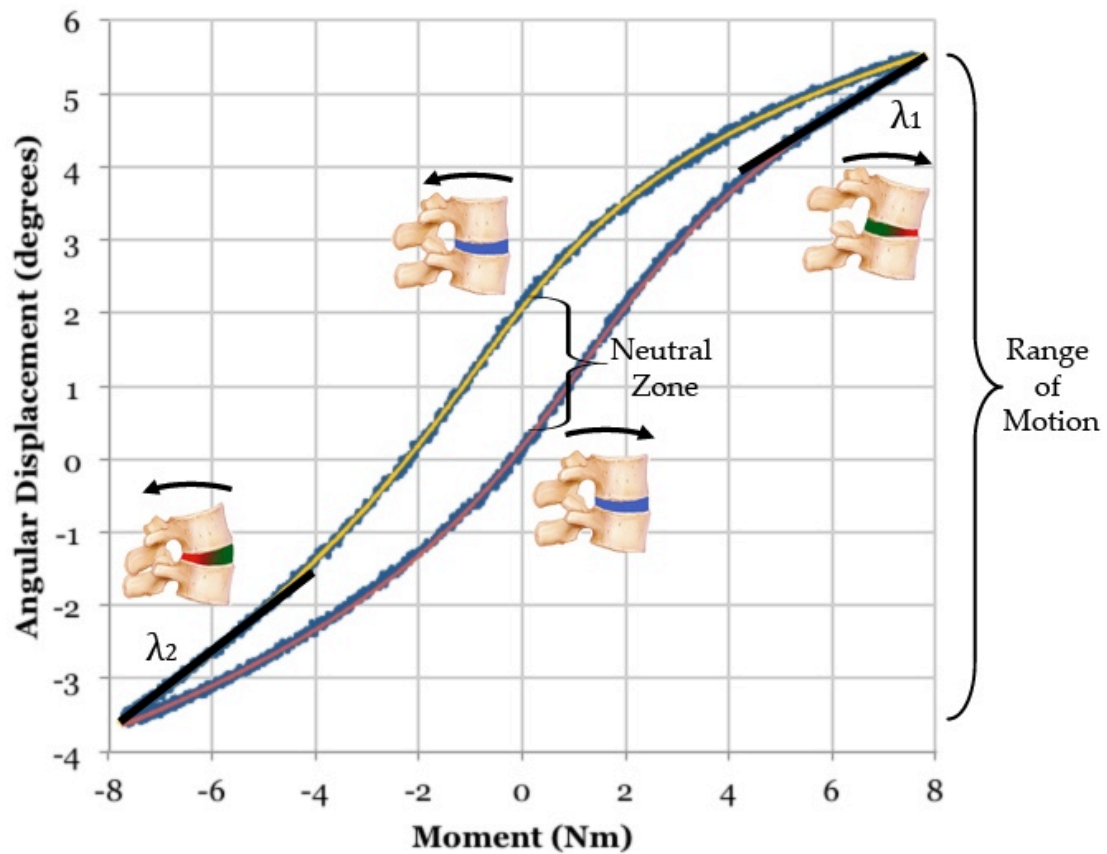


Figure 4.10. Representative Angular Displacement- Moment Plot with Metrics. The range of motion is defined as the maximum displacement and the neutral zone is defined as the displacement between the zero moment values on the unloading curves. Neutral Zone Ratio was computed by dividing the range of motion by the neural zone (NZ/ROM). Bending stiffness (λ_1 , λ_2) was defined by fitting a linear regression line from the end range of motion step-wise backwards through the linear portion of the curve, until a minimum R^2 of 0.98 was reached.

4.2.5 SUMMARY OF FUNCTIONAL SPINE MECHANICS PARAMETERS

Table 4.2. Functional Spine Mechanics Parameters (n=54)

Variable	Units	Range	Levels Tested	Description
Range of Motion	degree	Flex: 0.1 – 7.26 Ext: 0.3 – 9.82 FE: 1.7 – 15.3 LB: 1.68 – 14.47 AR: 0.4 – 8.65	L3-L4 L4-L5 L5-S1	Angular Change from extreme bending in one direction to the other
Neutral Zone	degree	FE: 0.12 – 2.50 LB: 0.13 – 2.99 AR: 0.03 – 2.49	L3-L4 L4-L5 L5-S1	Angular Change between loading and unloading curve, when no moment is applied
Neutral Zone Ratio	degree / degree	Flex: 0.06 – 0.91 Ext: 0.08 – 0.52 FE: 0.03 – 0.29 LB: 0.05 – 0.30 AR: 0.03 – 0.41	L3-L4 L4-L5 L5-S1	Ratio of Neutral Zone to Range of Motion
Bending Stiffness	Nm / degree	Flex: 0.81 – 7.14 Ext: 0.78 – 5.31 LB: 1.83 – 12.77 AR: 2.56 – 35.75	L3-L4 L4-L5 L5-S1	Linear Change in Moment / Angular Change at end ranges of motion

4.2.6 HELICAL AXIS OF MOTION

Traditional biomechanical measurements of spinal kinetics typically define endpoints or scalars, which do not describe the pathway of motion. Since there are infinite ways in which a vertebra can get from point a to point b, a biomechanical measure of the pathway of vertebral motion may be a more sensitive measurement of spinal health. One way in which the pathway of motion has been described is through the use of the helical axis of motion. The helical axis parameters were extracted in accordance with methods first published by Spoor & Veldpaus 1980⁹⁰, and later expanded by Woltring et al. 1985⁹¹.

Figure 4.11 displays a rigid object undergoing both a rotation (ϕ) about an infinite helical

axis (\mathbf{n}) as well as a translation (\mathbf{t}) along that axis. First the Transformation Matrix (\mathbf{T}) is computed between two time steps, which describes the relative motion of the superior vertebral body with respect to the inferior vertebral body.

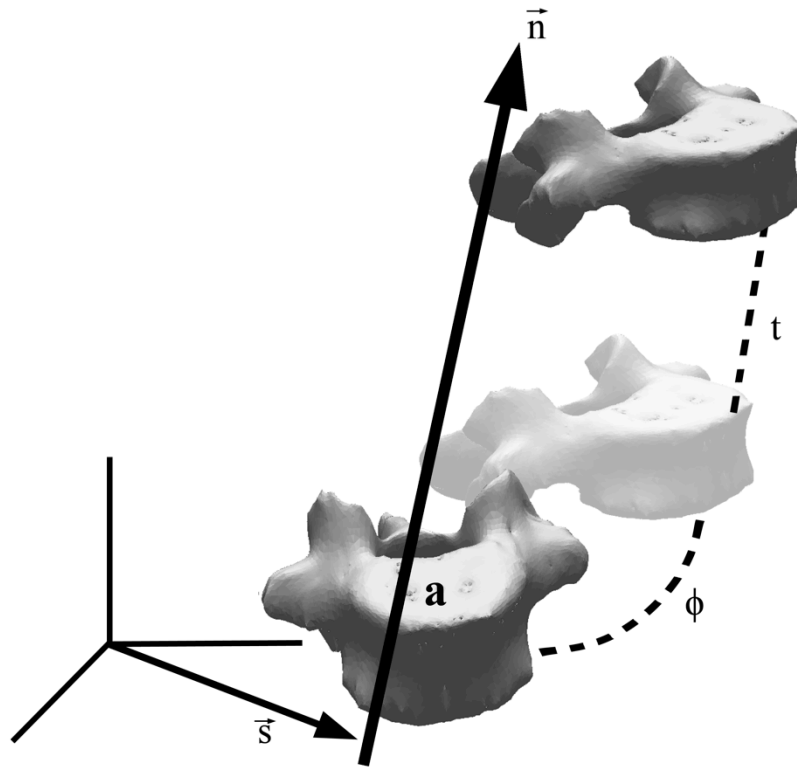


Figure 4.11- Helical Axis Parameters.

The above rigid object undergoes both a translation and a rotation about the helical axis (\mathbf{n}). The angle of rotation about the helical axis is ϕ . The translation along the helical axis is t . The position of the helical axis is defined as s , which is the shortest distance from the coordinate systems' origin to the helical axis.

The transformation matrix (\mathbf{T}) can be broken into two subsets, the rotation matrix (\mathbf{R}) and translation vector (\mathbf{v}). The rotation matrix components are such that \mathbf{R}_{ij} equals the cosine of the angle between the i^{th} axis in the original coordinate system and the j^{th} axis in the rotated coordinate system (i.e. when $i/j = 1$:x-axis, 2:y-axis, 3:z-axis).

The following Equation 2 was developed by Spoor and Veldpaus to describe how ϕ , the angle of rotation, and \mathbf{n} , the unit vector of the helical axis, are related to the components

of the rotation matrix $(\mathbf{R})^{90}$. The translation vector (\mathbf{v}) describes the linear translation the body undergoes in the rotated coordinate system

Equation 2

$$\sin \varphi * \begin{bmatrix} \mathbf{n}_1 \\ \mathbf{n}_2 \\ \mathbf{n}_3 \end{bmatrix} = \frac{1}{2} * \begin{bmatrix} \mathbf{R}_{32} - \mathbf{R}_{23} \\ \mathbf{R}_{13} - \mathbf{R}_{31} \\ \mathbf{R}_{21} - \mathbf{R}_{12} \end{bmatrix}$$

With $\mathbf{n}^T \mathbf{n} = 1$, the angle of rotation (φ) can be solved for by the following Equation 3 and plugged into the previous equation to solve for the helical axis unit vector (\mathbf{n}):

Equation 3

$$\sin \varphi = \frac{1}{2} \sqrt{(\mathbf{R}_{32} - \mathbf{R}_{23})^2 + (\mathbf{R}_{13} - \mathbf{R}_{31})^2 + (\mathbf{R}_{21} - \mathbf{R}_{12})^2}$$

The helical axis unit vector (\mathbf{n}), translation vector (\mathbf{v}), and angle of rotation (φ) can be used to determine a point on the helical axis (\mathbf{s}), specifically the point that is the shortest distance from the origin of the coordinate system to the helical axis, such that $\mathbf{n}^T \mathbf{s} = 0$ (Equation 4).

Equation 4

$$\mathbf{s} = -\frac{1}{2} \mathbf{n} \times (\mathbf{n} \times \mathbf{v}) + \frac{\sin \varphi}{2(1 - \cos \varphi)} \mathbf{n} \times \mathbf{v}$$

The translation along the helical axis can be quantified by the following Equation 5:

Equation 5

$$t = \sqrt{\mathbf{n}^T \mathbf{v}}$$

These metrics can be visualized previously in Figure 4.11, which displays an object that undergoes both a translation and a rotation. Thus, the outcome measures of a helical axis

solution are: the unit vector of the helical axis (\mathbf{n}), the location of the helical axis (\mathbf{s}), the translation along the axis (t), and the angle of rotation about that axis (ϕ).

The helical axis can be computed over a finite distance, or instantaneously by breaking the motion into multiple steps. Figure 4.12 illustrates this concept. A single helical axis can be computed as the vertebral body moves from position a to position b or multiple axes can be computed from a^1 to a^2 to a^3 and finally to b . The instantaneous helical axes (IHA) approach allows understanding of the pathway of motion, rather than only investigating the end points of motion.

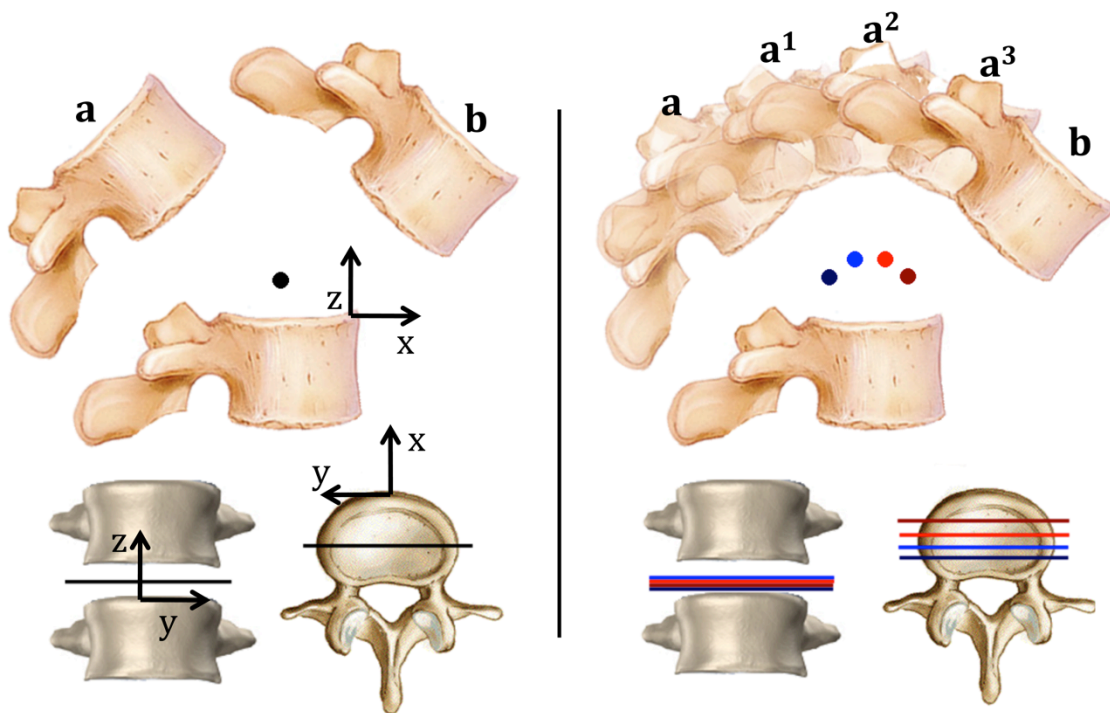


Figure 4.12. Instantaneous Helical Axis of Motion.

A single helical axis can be computed as the vertebral body moves from position a to position b (left) or multiple axes can be computed from a^1 to a^2 to a^3 and finally to b (right). The instantaneous helical axes approach allows understanding of the pathway of motion, rather than only investigating the end points of motion.

Following a sensitivity analysis, detailed in the Appendix, the kinematic data was filtered using a fourth order low-pass Butterworth filter with a cutoff frequency of 0.4 Hz, which is similar to other literature values^{92,93}. However, much of the published helical axis work does not describe their filtering parameters^{84,94-96}. The IHA was computed at every 0.05 degree increments, which were the smallest step size for which stable helical axes could be calculated. The IAR was calculated as where the IHA crosses the mid-sagittal plane (x, z plane) of the intervertebral disc during flexion or extension and the anterior coronal plane (y, z plane) of the intervertebral disc during lateral bending. The IHA was not calculated during axial rotation, due to the small degree of rotation during this motion.

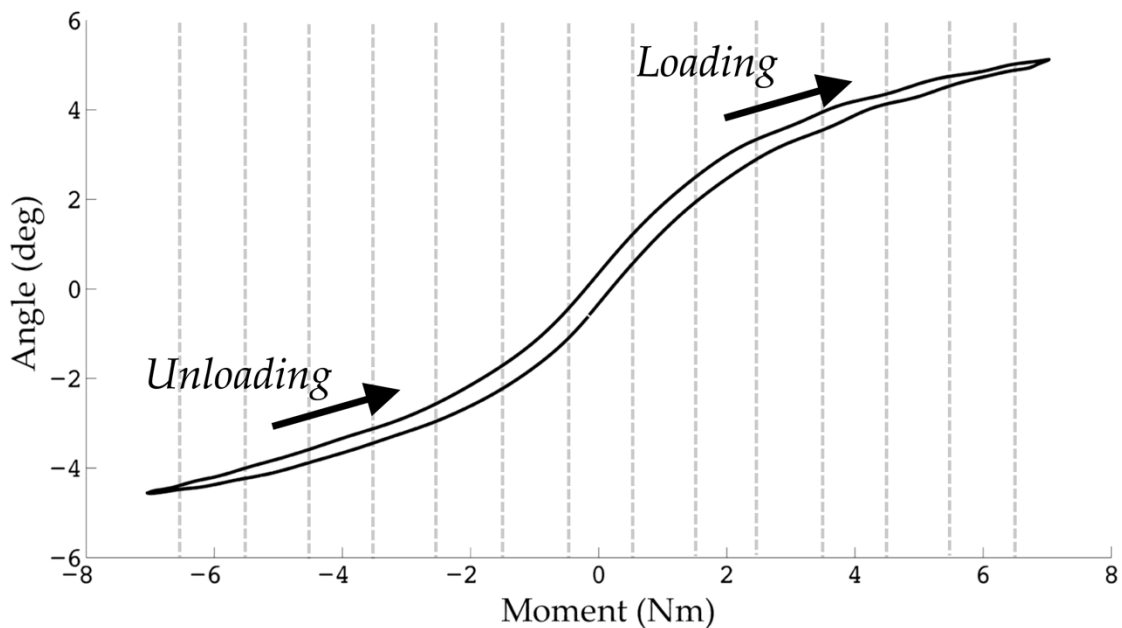


Figure 4.13. Representative Angle vs. Moment Plot with 1 Nm Bins.

The helical axes were calculated every 0.05 degrees, then the helical axis orientation and axis of rotation were averaged over a 1 Nm window from -6.5 Nm to 6.5 Nm and 6.5 Nm to -6.5 Nm, through the unloading and loading curves.

The computed IHA were used for visualization purposes, but for statistical hypothesis testing, the IHA orientation and IAR location was averaged over a 1 Nm window from -

6.5 Nm to 6.5 Nm and 6.5 Nm to -6.5, through the unloading and loading curve, Figure 4.13. This resulted in a minimum of 8 vectors for each direction of bending over the 1Nm window. The standard deviations of the IHA and IAR over each window were also investigated as a relative term of the spread of the helical axes and axes of rotation; a larger standard deviation would be indicative of more instability. Also, over the same windows a minimally enclosed ellipse was fit over the IAR and area was recorded. Using a similar technique, a minimally enclosed ellipse was fit over the vector tips at one unit vector in the primary direction away; the area was recorded, and the volume of vector space was measured by integrating the volume from the IAR ellipse to the vector tip ellipse. Figure 4.14 illustrates this technique by fitting the IAR and vector tips to a minimally enclosed ellipse and displaying the volume of the vector space.

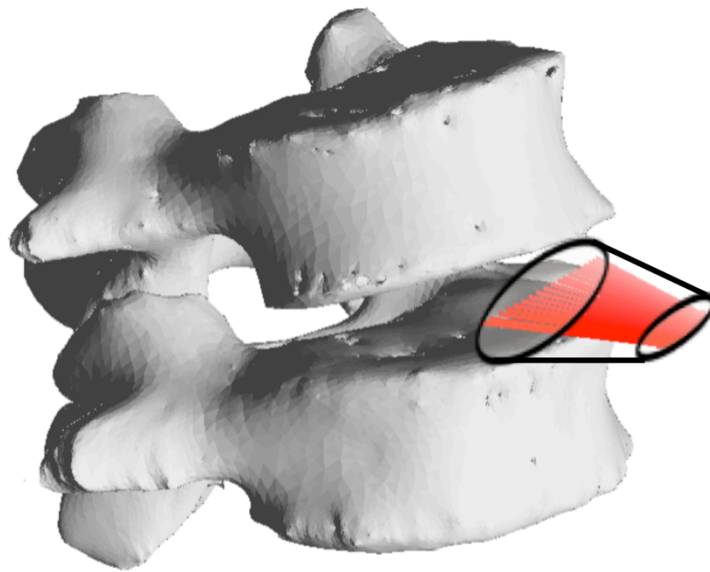


Figure 4.14. Minimally Enclosed Ellipse of IAR, Vector Tips, and Volume of Vector Space.

Each ellipse displayed on the figured is a minimally closed ellipse surrounding the instantaneous axes of rotation (nearest the intervertebral disc) and tips of vectors (away from disc). Also the entire volume of the vector space was computed by integrating between each of the enclosed ellipses.

4.2.7 SUMMARY OF HELICAL AXIS PARAMETERS

Table 4.3. Helical Axis Parameters (n=18)

Variable	Units	Range	Levels Tested	Description
Helical Axis Orientation	Unitless (unit vector)	0.02- 0.98	L4-L5	Three-dimensional Orientation of the instantaneous helical axis
Helical Axis Orientation Standard Deviation	Unitless (unit vector)	0.01- 0.40	L4-L5	Relative Measure of Spread in Helical Axis Orientation
Instantaneous Axis of Rotation	Unitless (normalized by disc dimensions)	0.03- 3.08	L4-L5	Two-Dimensional point where helical axis crosses the mid-sagittal plane of the disc for FE and mid-coronal plane of the disc for LB
Instantaneous Axis of Rotation Standard Deviation	Unitless (normalized by disc dimensions)	0.02- 5.81	L4-L5	Relative Measure of Spread in Instantaneous Axis of Rotation

4.3 LOCAL TISSUE COMPRESSIVE MECHANICS

Following testing in the Spine Kinetic Simulator, further investigation into the local compressive mechanical properties of the intervertebral disc was conducted on the L4-L5 level. Recall that numerous types of local disc tissue biomechanical tests can be performed. Most of these violate the endplate and disrupt the disc tissue, so we have therefore developed an in situ confined methodology aimed at testing the mechanical properties in situ²⁰. The inferior vertebral body (L5) was embedded in PMMA (Figure 4.15A), while the superior body (L4) was cut in half and the trabecular bone was removed (Figure 4.15B), leaving the endplate visible and intact. A custom jig (Figure 4.15C) was used to release a 3mm diameter circular portion of the endplate contiguous with the IVD tissue inferiorly (Figure 4.15D). The rigid porous endplate provides a

boundary connection to the indenter to facilitate hybrid confined / *in situ* indentation loading.

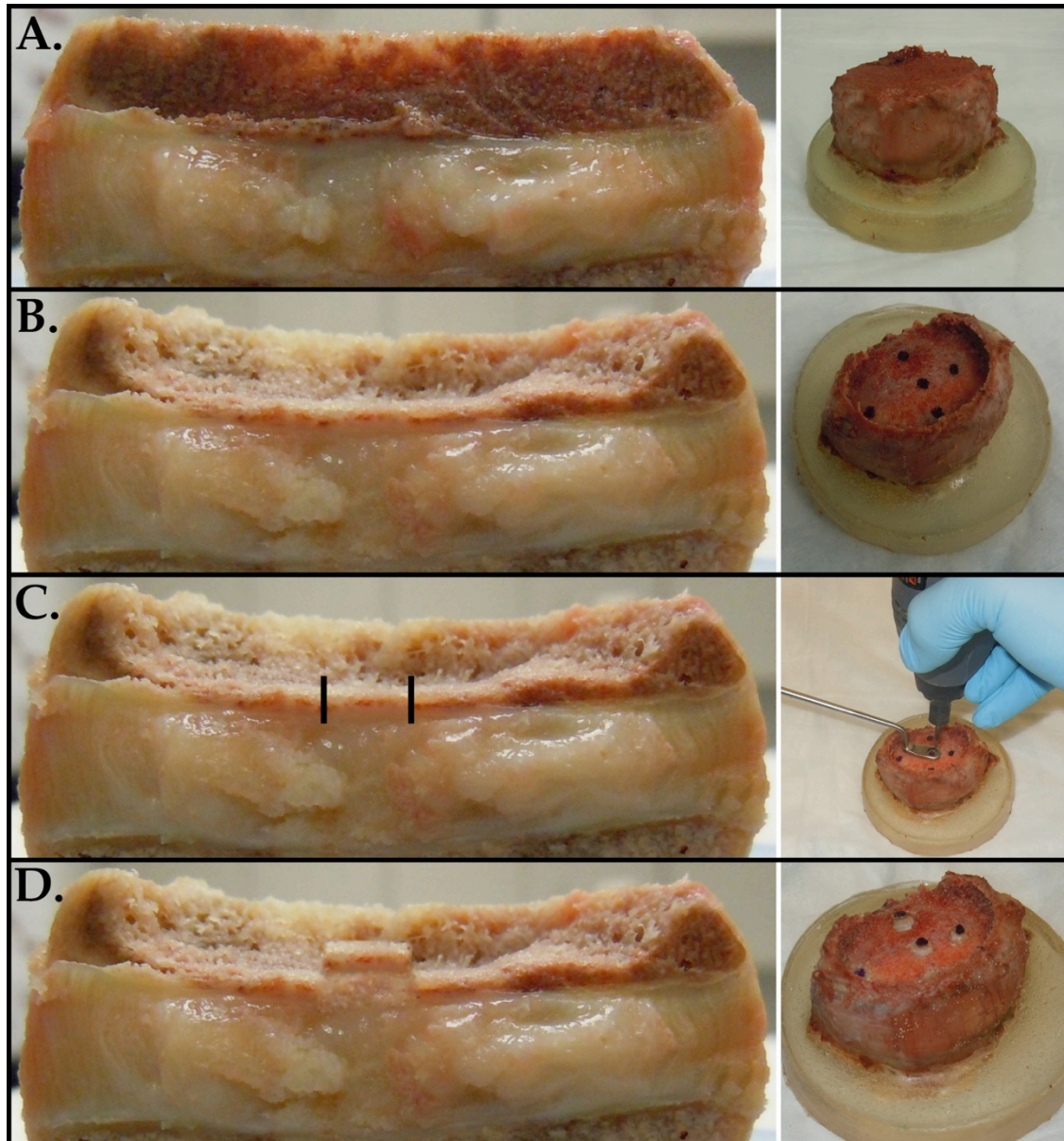


Figure 4.15. Sample Preparation for Hybrid Confined/*in situ* Indentation Tests. Sample has been cut in half for display purposes only. **A.** The inferior body (L5) is potted in PMMA and superior body (L4) is cut in half. **B.** Trabecular bone is removed from the superior vertebral body. This leaves the cartilaginous endplate visible and intact. **C.** Using a custom made jig and a high –speed rotary tool, a 3mm circular portion of the endplate is released from the rest of the endplate, while leaving the intervertebral disc still attached below. **D.** Following releases of the endplate, the portion rose in height, indicating the presence of an internal residual stress.

4.3.1 HYBRID CONFINED / IN SITU INDENTATION METHODOLOGY

The hybrid confined/*in situ* indentation test was performed at 5 regionally spaced sites, displayed in Figure 4.16, included the center nucleus pulposus (NP) and four in the annulus fibrosus (AF), including three outer AF areas: anterior (aAF), posterior (pAF), and lateral (oAF), as well as one inner lateral region (iAF). These were the same regions of interest used in T2* quantification.

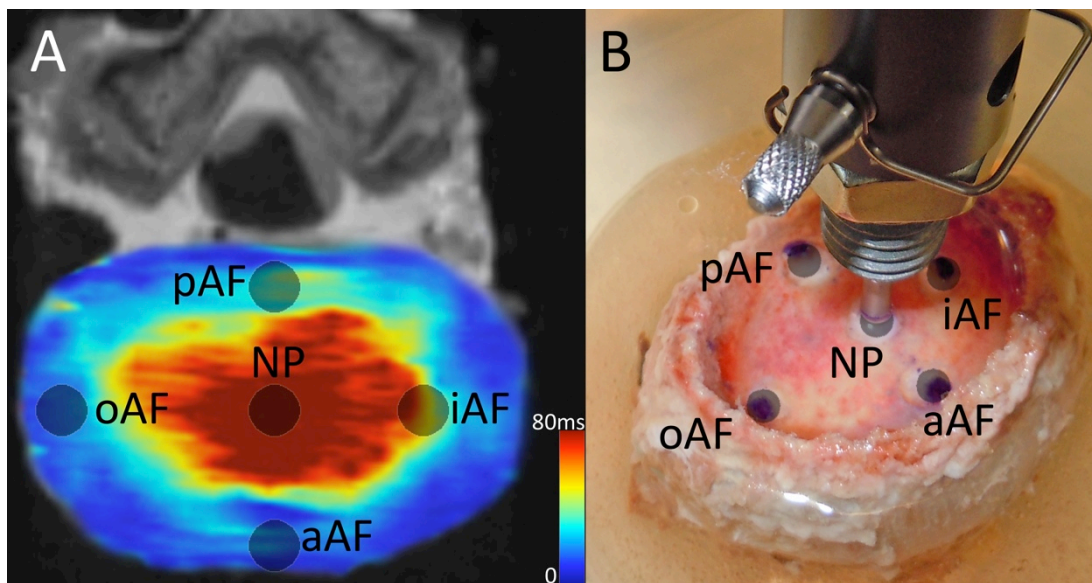


Figure 4.16. Hybrid Confined/*in situ* Indentation Test Sites.

*Test locations on a specimen undergoing stress relaxation tests using hybrid confined/*in situ* indentation methodology. These were the same regions used in measuring MRI values. NP: nucleus pulposus, AF: annulus fibrosus, o: outer, i: inner, a: anterior, p: posterior*

Following excision of the endplate, the released section increased in height, indicating the presence of an internal residual stress (Figure 4.15D). The height increase was used to calculate the excised strain by dividing the change in height increase by the original site-specific disc height (ϵ_R). Site-specific heights were measured from MR image reconstructions at each test location.

Each test site was subjected to stress-relaxation indentation tests performed with an Instron microtester (5548 Instron, Norwood, MA) equipped with a 3mm cylindrical indenter tip. Load and displacement were recorded using Bluehill software (Instron Systems) at 100Hz. The entire IVD was submerged in room temperature 0.9% saline solution 30 minutes prior to testing and remained so throughout the test to keep the disc physiologically hydrated.

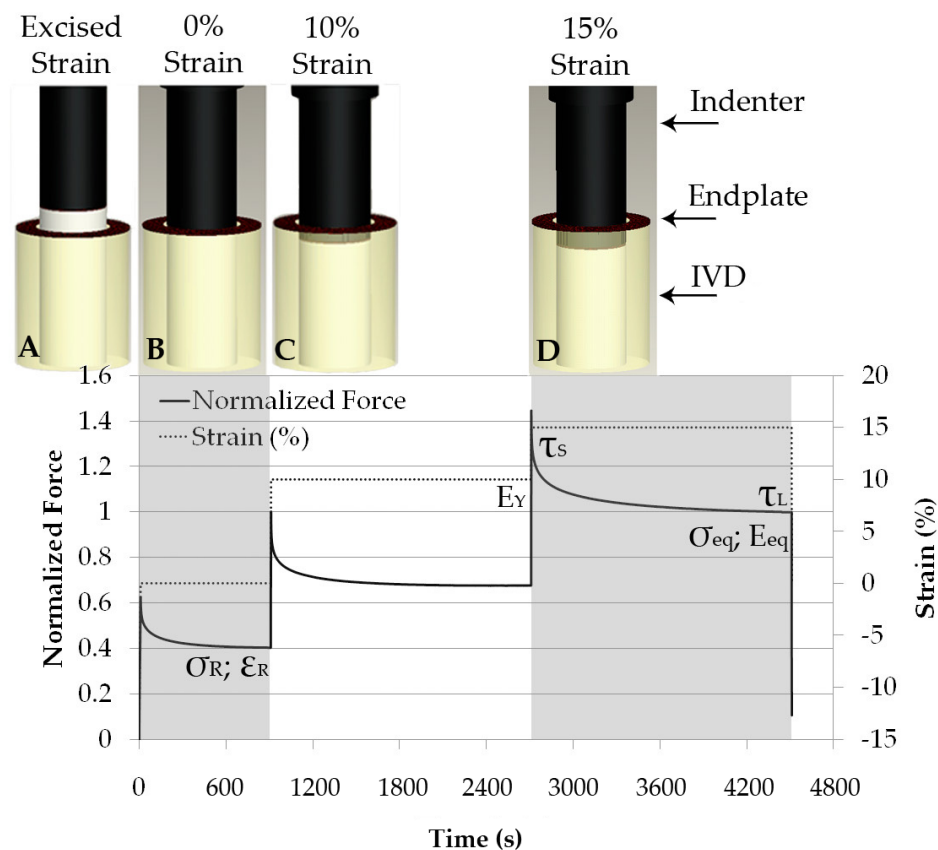


Figure 4.17. Time history of stress-relaxation protocol with representative test site data. Following excision of the endplate, the released section increased in height (A), indicating the presence of an internal residual stress. The height increase was used to calculate the excised strain. The endplate was re-positioned back to its original height with the indenter tip and allowed to equilibrate for 900 sec (B); this equilibrium residual stress was measured. The tissue was then subjected to a 10% strain preload and allowed to relax for 1800 sec (C); followed by an additional 5% strain applied at a rate of 5% strain/second and held for another 1800 sec (D). Test site-specific strains were computed from MR image reconstructions providing the intact disc height (reprinted with permission)²⁰.

The test protocol, displaying representative force and strain data, is visually represented in Figure 4.17. The endplate was re-positioned back to its original height with the indenter and allowed to equilibrate for 900 seconds; the equilibrium residual stress was determined by dividing the applied equilibrium force by the 3mm indenter tip area (σ_R). The tissue was then subjected to a 10% strain preload and allowed to relax for 900 seconds; followed by an additional 5% strain applied at a rate of 5% strain/second and held for another 1800 seconds. In all tests, this protocol resulted in relaxation equivalent to less 0.02% change in force over the final 100 seconds, which we have defined as equilibrium. The peak force was collected and the elastic modulus (E_V) was computed on the final ramp as the change in stress over the change in strain. The final equilibrium force value was used to quantify the equilibrium stress (σ_{eq}), similar to the residual stress calculation. The equilibrium modulus (E_{eq}) was found using the following Equation 6⁹⁷:

Equation 6

$$E_{eq} = \frac{P \cdot (1 - \nu^2)}{2 \cdot a \cdot h}$$

where ‘P’ is the equilibrium force, ‘a’ is the radius of the indenter, ‘h’ is the indentation depth, and ‘ ν ’ is the Poisson’s ratio⁹⁸. Poisson’s ratio was estimated to be 0.4, 0.375, or 0.35 for ‘healthy’, ‘moderate’, or ‘severe’ tissues in the outer annular regions and 0.445, 0.4, or 0.375 for inner annular regions, respectively⁹⁹. The Poisson’s ratio input for ‘healthy’, ‘moderate’ or ‘severe’ in the NP region ranged from 0.49 to 0.445 to 0.4, respectively⁹⁹.

The final stress-relaxation curve was fit to the following 3 series prony stress-relaxation function ($G(t)$) to understand the viscoelastic response of the tissue, Equation 7¹⁰⁰. It has

been previously shown that a 3 series model was efficient and comparable to the continuous spectrum model^{100,101}. The force was normalized by the equilibrium force before curve-fitting.

Equation 7

$$G(t) = 1 + g \cdot \sum_{i=1}^3 e^{\frac{-t}{\tau_i}}$$

Curve-fitting to this function allows for the quantification of spectrum magnitude (g) and three time constants ($\tau_1 = \tau_S$, $\tau_2 = \tau_M$, $\tau_3 = \tau_L$, where τ_M is the logarithmic average of τ_S , τ_L). The computation of τ_M was based on the assumption that there was a decadic interval between τ_S and τ_L , which was consistent with our data¹⁰¹. These metrics govern the overall shape of the curve, allowing for comparison of stress-relaxation responses between different locations and degeneration grades. All post-processing was completed using MATLAB custom scripts (Mathworks Inc. Natick, MA).

4.3.2 SUMMARY OF COMPRESSIVE MECHANICAL PROPERTIES

Table 4.4. Compressive Mechanical Parameters (n=18)

Variable	Units	Range	Levels Tested	Sites Investigated	Description
Residual Stress	MPa	0 – 0.20	L4-L5	NP, aAF, pAF, iAF, oAF	Equilibrium Force (0% strain) / indentation area
Excised Strain	% Strain	0 - 29.8	L4-L5	NP, aAF, pAF, iAF, oAF	Change in disc height following release of endplate / original disc height
Equilibrium Modulus	MPa	0.01 – 0.72	L4-L5	NP, aAF, pAF, iAF, oAF	Modulus determined at 15% Strain
Spectrum Magnitude (g)	Unitless	0.06 – 149.24	L4-L5	NP, aAF, pAF, iAF, oAF	Dictates relative size of viscoelastic relaxation curve
Tau 1	sec	0.06 – 10.37	L4-L5	NP, aAF, pAF, iAF, oAF	Short Viscoelastic Time Constant
Tau 2	sec	0.20 – 11.06	L4-L5	NP, aAF, pAF, iAF, oAF	Logarithmic Average of Short and Long Viscoelastic Time Constant
Tau 3	sec	1.67 – 38.74	L4-L5	NP, aAF, pAF, iAF, oAF	Long Viscoelastic Time Constant
Equilibrium Stress	MPa	0.01 – 91.6	L4-L5	NP, aAF, pAF, iAF, oAF	Equilibrium force (15% strain) / indentation area
Elastic Modulus	MPa	0.08 – 0.57	L4-L5	NP, aAF, pAF, iAF, oAF	Change in stress / strain during 5% strain ramp

4.4 BIOCHEMICAL ANALYSIS

Following the indentation protocol, each intervertebral disc was wrapped in 0.9% saline soaked chuck and re-frozen at -20°C. Subsequent biochemical analysis was performed at each test site investigating the proteoglycan and total collagen content. Proteoglycans are

made up of a core protein with many covalently attached glycosaminoglycan chains and typically assay of the sulfated-glycosaminoglycan (s-GAG) reveals the proteoglycan concentration within a tissue.

A sharp 3 mm biopsy punch was used to remove the endplate-disc-endplate construct at each test site (Figure 4.18). Both endplates were then removed, and the cylindrical disc sample was divided in half along the transverse axis. In a randomized fashion, either the superior or inferior section was used to quantify either s-GAG or collagen (Figure 4.19).

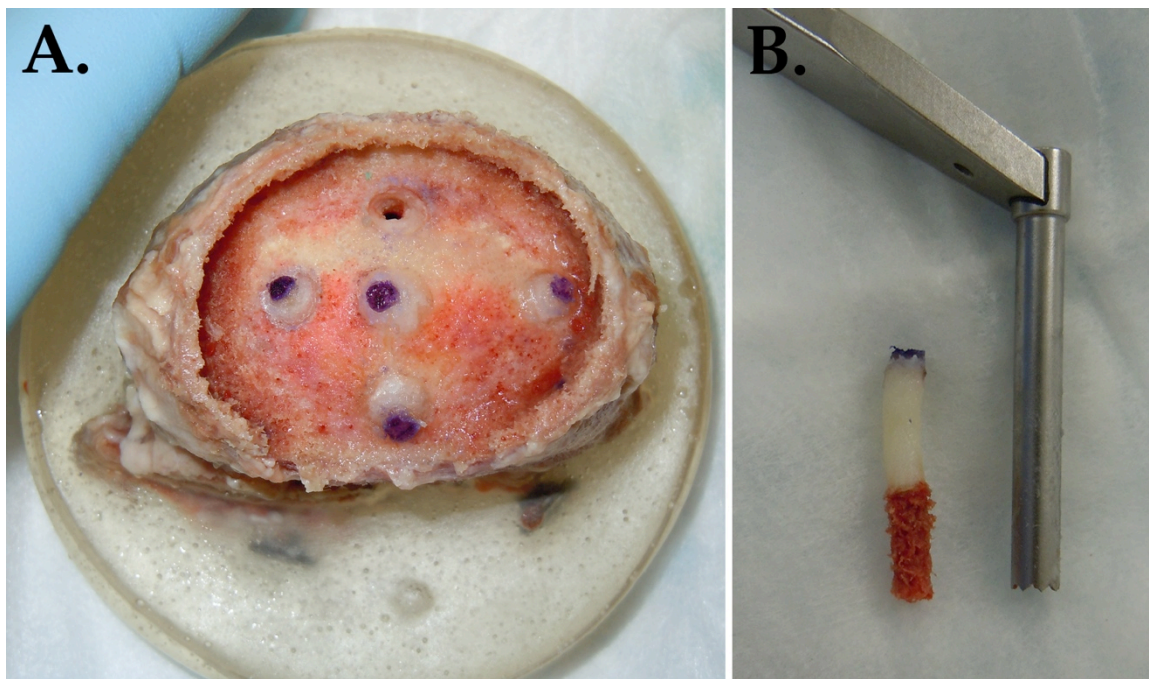


Figure 4.18. Sites for Biochemical Analysis.

A 3 mm biopsy punch was used to remove a plug of tissue at the same locations where indentation tests were performed, and where MRI relaxation times were recorded. The endplate and inferior trabecular bone were removed prior to biochemical quantification.

To determine s-GAG and water content, disc samples were dried at 60°C to constant dry weight (for three days). Water content (% H₂O) was also calculated as (wet weight-dry weight)/wet weight at each location. A commercially available 1,9 dimethylmethylene blue (DMB) assay was used (Astart Biologics Rheumera, Proteoglycan Detection Kit,

Redmond, WA). Dried samples were digested with Protease-K at 56°C overnight to cleave the protein into polypeptide fragments, by cleaving peptide bonds (Worthington Biochemical Corporation, Proteinase K). Samples were diluted in phosphate buffered saline (1:2000) to be within the standard curve. Then, the cationic dimethylmethylene blue was added and the GAG content detected at 525 nm. DMB binds with the sulfate groups on the s-GAG resulting in a color shift. s-GAG content was normalized by dry weight ($\mu\text{g}/\mu\text{g}$).

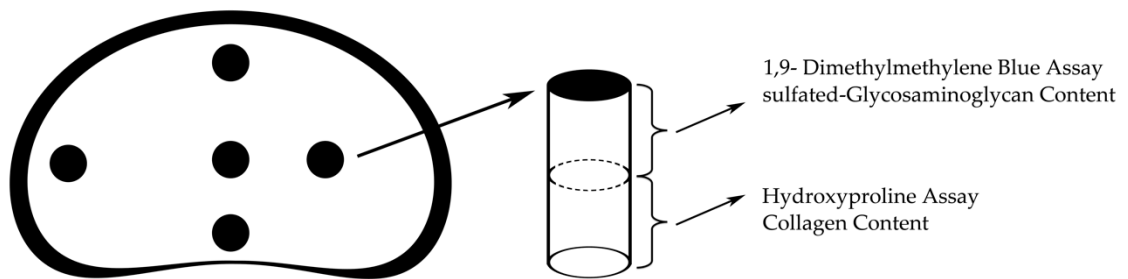


Figure 4.19. Schematic for Biochemical Analysis.

A 3mm plug was removed from each test site. Both endplates were then removed and the cylindrical disc sample was divided in half along the transverse axis. In a randomized fashion, either the superior or inferior section was used to quantify either s-GAG or collagen.

To determine protein content in the ninhydrin and hydroxyproline assays, samples were prepared using a method adapted from Starcher¹⁰². Samples were digested with 6N HCl for 24 hours at 110°C to cleave all peptide bonds. Then, the acid was removed with a SpeedVac centrifugal evaporator with heating at 45°C. Samples were solubilized in assay buffer of 1:10 stock buffer (5 g/L citric acid (monohydrate) (Sigma), 12 g/L sodium acetate (trihydrate) (Sigma), sodium hydroxide 3.4 g/L, and 1.2 mL glacial acetic acid (Sigma)). A small amount of charcoal was added to remove sugars and the charcoal

subsequently removed by passing the samples through glass wool. Prior to assay, samples were briefly centrifuged to remove any remaining charcoal.

The ninhydrin assay used was adapted from Starcher and described here briefly. This assay detects amine groups. Samples were diluted in H₂O (from millipore, > 16MΩcm, 1:200) to be within the standard curve. A stannous chloride (57 mg tin(II) chloride (Sigma) and 570 μL ethylene glycol) and ninhydrin (200 mg ninhydrin (Sigma), 7.5 mL ethylene glycol, 4N sodium acetate buffer (pH 5.5)) solution (300 μL stannous chloride solution and 12 mL ninhydrin solution) was added, and the plate was incubated at 56°C for one hour. Total protein content was detected at 570 nm.

The hydroxyproline assay used was adapted from Stegemann and Stalder and is described here briefly¹⁰³. This assay detects hydroxyproline residues. Collagen is a helical chain, made up of a three amino acid sequence of hydroxyproline – X – glycine, where X is any other amino acid, so collagen has high hydroxyproline content. Samples were diluted in assay buffer (1:20) to be within the standard curve. Chloramine-T (0.141 g Chloramine-T (Sigma), 5.33 mL stock buffer, 2.6 mL N-propanol, and 2.07 mL H₂O (from Millipore, > 16MΩcm)) and Dimethylaminobenzaldehyde (p-DMBA) (1 g p-DMBA (Sigma), 6 mL N-propanol, and 2.6 mL Perchloric acid (Fischer Scientific)) were added and hydroxyproline detected at 570 nm. Chloramine-T and p-DMBA form a chromophore on the hydroxyproline residues. Hydroxyproline content was normalized by total protein (μg/μg) and s-GAG content (μg/μg). Dry weights were not available.

4.4.1 SUMMARY OF BIOCHEMICAL PROPERTIES

Table 4.5. Biochemical Parameters (n=18)

Variable	Units	Range	Levels Tested	Test Sites	Description
Sulfated-Glycosaminoglycan Content (% dry weight)	µg / µg	3.9 – 53.9	L4-L5	NP, aAF, pAF, iAF, oAF	1,9 dimethylmethylene blue assay
Hydroxyproline Content (normalized by s-GAG content)	µg / µg	0.01 – 1.61	L4-L5	NP, aAF, pAF, iAF, oAF	Hydroxyproline assay / 1,9 dimethylmethylene blue assay
Hydroxyproline Content (% total protein)	µg / µg	1.6 – 16.1	L4-L5	NP, aAF, pAF, iAF, oAF	Hydroxyproline assay / ninhydrin assay
Water Content	%H ₂ O	66.9 – 86.4	L4-L5	NP, aAF, pAF, iAF, oAF	(wet weight-dry weight) / wet weight

4.5 STATISTICAL TREATMENT AND TESTING OF HYPOTHESES

All statistical analyses were performed using SPSS 20.0 (IBM Corp., Armonk, NY). An intra-class correlation coefficient was found for between observer variability on disc grade. Pearson correlational tests were performed between numerous parameters investigating the relationship between disc health and biochemical content and mechanical function. A repeated measures analysis of variance (ANOVA) was performed on the location biochemical content, local compressive biomechanics, and local imaging relaxation times between each test site with in a specific degeneration level. Degeneration severity was categorized ‘Healthy’, ‘Moderate’ and ‘Severe’ based on an even weighted average of three T2* MR imaging parameters:

Equation 8

$$\frac{NP T2^*}{\text{Max NP T2}^*} + \frac{T2^* \text{ Intensity Area}}{\text{Max T2}^* \text{ Intensity Area}} + \frac{\text{Transition Zone Slope}}{\text{Max Transition Zone Slope}}$$

‘Healthy’ had a value of half the standard deviation above the average and ‘Severe’ was less than half the standard deviation below the average. ‘Moderate’ discs were within half the standard deviation above and below the average.

An ANOVA was also performed to assess the differences at each test-site between each degeneration level. All pair-wise post-hoc t-tests were performed using a Tukey correction. For all tests an alpha value of 0.05 was used to determine significance. Each null hypothesis was tested independently to evaluate the role of disc health on the functional mechanics of the spine. The hypotheses are re-stated below with the statistical test utilized for evaluation.

Hypothesis 1: *Pfarrmann Grade is negatively correlated with the following quantitative T2* MR imaging parameters: a) the NP T2* relaxation time, b) transition zone slope between the NP and AF, and c) T2* signal intensity area of the coronal plane.* A Pearson’s correlation test was performed between each Pfarrmann Grade and each of the T2* imaging parameters, where the null hypothesis is no correlation between each of the variables.

Hypothesis 2: *The T2* relaxation time is correlated with the following site-specific biochemical properties: A) Glycosaminoglycan Content (positively), B) Hydroxyproline Content (negatively), and C) water content (positively), at the following regions: a) NP, b) inner lateral AF, c) outer lateral AF, d) anterior AF, and e) posterior AF.* A Pearson’s

correlation test was performed between the site-specific T2* relaxation time and corresponding biochemical content, where the null hypothesis is that there is no correlation.

Hypothesis 3: *The T2* relaxation time is positively correlated with the following local compressive mechanical properties: A) residual stress and B) excised strain at the following regions: a) NP, b) inner lateral AF, c) outer lateral AF, d) anterior AF, and e) posterior AF. A Pearson's correlation test was performed between the site-specific T2* relaxation time and corresponding biomechanical properties, where the null hypothesis is that there is no correlation.*

Hypothesis 4: *The range of motion in A) flexion, B) extension, and C) lateral bending is positively correlated with, and d) axial rotation is negatively correlated with T2* MR imaging parameters of disc health, including: a) NP T2* relaxation, b) transition zone slope between the NP and AF, and c) T2* signal intensity area of the coronal plane. A Pearson's correlation test was performed between the intersegmental range of motion and T2* MR imaging parameters of disc health, where the null hypothesis is that there is no correlation.*

Hypothesis 5: *The neutral zone to range of motion ratio in A) flexion, B) extension, C) lateral bending and D) axial rotation negatively correlated with T2* MR imaging parameters of disc health, including: a) NP T2* relaxation time, b) transition zone slope between the NP and AF, and c) T2* signal intensity area of the coronal plane. A Pearson's correlation test was performed between the intersegmental neutral zone to*

range of motion ratio and T2* MR imaging parameters of disc health, where the null hypothesis is that there is no correlation.

Hypothesis 6: *The bending stiffness in A) flexion, B) extension, and C) lateral bending is negatively correlated with, and d) axial rotation positively correlated with T2* MR imaging parameters of disc health, including: a) NP T2* relaxation, b) transition zone slope between the NP and AF, and c) T2* signal intensity area of the coronal plane.* A Pearson's correlation test was performed between the intersegmental spinal unit bending stiffness and T2* MR imaging parameters of disc health, where the null hypothesis is that there is no correlation.

Hypothesis 7: *The average primary orientation of the helical axis vector in A) flexion, B) extension, and C) lateral bending is positively correlated with T2* MR imaging parameters of disc health, including: a) NP T2* relaxation time, b) transition zone slope between the NP and AF, and c) T2* signal intensity area of the coronal plane.* Pearson's correlation tests were performed between the average primary helical axis unit vector component, computed over a 1 Nm window from one end range of motion to the other, through unloading and loading (-6.5 Nm to 6.5 Nm), and T2* MR imaging parameters. The null hypothesis is that there is no correlation between the orientation of the helical axis and the T2* MR imaging parameters throughout motion.

Hypothesis 8: *The standard deviation of the primary orientation of the helical axis vector in A) flexion, B) extension, and C) lateral bending is negatively correlated with T2* MR imaging parameters of disc health, including: a) NP T2* relaxation, b) transition zone slope between the NP and AF, and c) T2* signal intensity area of the coronal plane.*

Pearson's correlation tests were performed between the standard deviation of the primary helical axis unit vector components, computed over a 1 Nm window from one end range of motion to the other, through unloading and loading (-6.5 Nm to 6.5 Nm), and T2* MR imaging parameters. The null hypothesis is that there is no correlation between the standard deviation of the helical axis vector orientation and the T2* MR imaging parameters throughout motion.

Hypothesis 9: *The average distance of the instantaneous axis of rotation from the origin in A) flexion, B) extension, and C) lateral bending is negatively correlated with T2* MR imaging parameters of disc health, including: a) NP T2* relaxation, b) transition zone slope between the NP and AF, and c) T2* signal intensity area of the coronal plane.*

Pearson's correlation tests were performed between the average IAR position, computed over a 1 Nm window from one end range of motion to the other, through unloading and loading (-6.5 Nm to 6.5 Nm), and T2* MR imaging parameters. The null hypothesis is that there is no correlation between the movement of the IAR and the T2* MR imaging parameters.

Hypothesis 10: *The standard deviation of the distance of the instantaneous axis of rotation from the origin in A) flexion, B) extension, and C) lateral bending are negatively correlated with T2* MR imaging parameters of disc health, including: a) NP T2* relaxation time, b) transition zone slope between the NP and AF, and c) T2* signal intensity area of the coronal plane.* Pearson's correlation tests were performed between the standard deviation of the IAR position, computed over a 1 Nm window from one end range of motion to the other, through unloading and loading (-6.5 Nm to 6.5 Nm), and T2* MR imaging parameters. The null hypothesis is that there is no correlation between

the standard deviation of the IAR movement and the T2* MR imaging parameters throughout motion.

Hypothesis 11: *The A) bending stiffness, B) range of motion, and C) neutral zone to range of motion ratio in A) flexion, B) extension, C) lateral bending, and D) axial rotation are correlated with the a) residual stress, b) excised strain, c) sulfated-glycosaminoglycan content, and d) water content in the NP.* A Pearson's correlation test was performed between the intersegmental functional mechanics and the discs' biochemical and biomechanical properties, where the null hypothesis is that there are no correlations.

Hypothesis 12: *The A) helical axis orientation and B) instantaneous axis of rotation location in A) flexion, B) extension, and C) lateral bending are significantly correlated to the a) residual stress, b) excised strain, c) sulfated-glycosaminoglycan content, and d) water content in the NP.* Pearson's correlation tests were performed between both the average primary helical axis unit vector component and the average IAR position (x, y), computed over a 1 Nm window from one end range of motion to the other, through unloading and loading (-6.5 Nm to 6.5 Nm), and local biomechanical and biochemical properties. The null hypothesis is that there is no correlation between either the orientation of the helical axis or the position of the IAR and the discs' biochemical and biomechanical properties throughout motion.

5 CHAPTER 5: RESULTS

The methods for this work were performed in the order reported in Chapter 4 due to the progressively destructive nature of the experiments. The results section will report the results of the imaging initially and then present the results from the local biochemistry, local mechanics, and then global kinematics of the spinal segment. This treatment of the results follows the rationale for the hypotheses, as they have been numbered, from a micro-scale to a macro-scale.

All eighteen human cadaveric lumbar spine segments were imaged with MRI and received the full battery of biomechanical testing and biochemical analyses. The specimen demographics are reported in Table 5.1 below. The mean age of the specimens was 53.2 ± 15.5 years ranging from 21 to 71 years including 11 males and 7 females.

Table 5.1. Specimen Demographics

Age	Sex	Height (cm)	Weight (kg)	Cause of Death
21	M	175.26	65.77	Gunshot Wound of the Head
29	M	190.50	77.11	Unavailable
32	F	167.64	79.38	Blunt Force Head Injury
39	F	165.10	90.72	Metastatic Malignant Melanoma
43	F	172.72	77.11	Oxycodone Toxicity
45	M	182.88	83.91	Alcohol Poisoning
48	M	182.88	104.33	Unavailable
49	M	177.80	72.57	Atherosclerotic Cardiovascular Disease
58	M	177.80	79.38	Cardiac Arrest
60	M	180.34	133.81	Congestive Heart Failure
61	F	170.18	104.33	Liver Metastasis
62	M	170.18	68.04	Myocardial Infarction
65	M	185.42	108.86	Ischemic Bowel Necrosis
66	F	152.40	65.77	Myocardial Infarction
69	M	180.34	131.54	Congestive Heart Failure
69	F	162.56	108.86	Ventricular Failure
70	M	177.80	72.57	Sepsis
71	F	172.72	72.57	Alzheimer's Dementia

5.1 QUANTITATIVE T2* ASSESSMENT OF DISC HEALTH

All 54 intervertebral discs were imaged and given a Pfirrmann Grade based on the observations of seven spine surgeons and three experienced spine researchers. The graders of disc health had an intra-class correlation coefficient value of 0.686. The average rater Pfirrmann grade indicates a normal distribution of disc health included in the study (Figure 5.1).

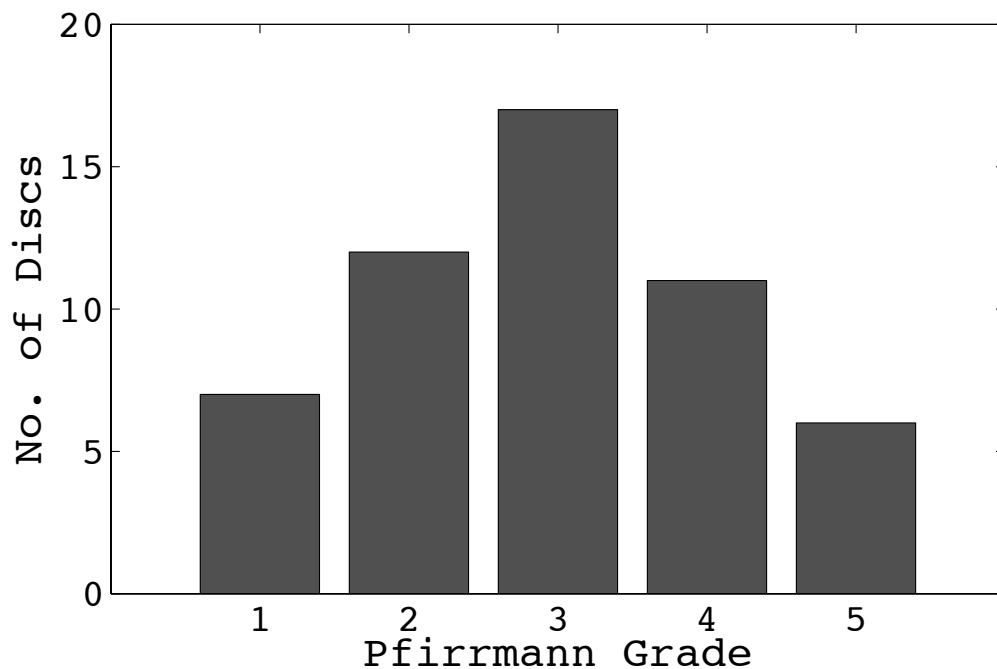


Figure 5.1. Distribution of Disc Health.

The sample of 54 intervertebral discs displays a normal distribution when graded based on the Pfirrmann scale.

Pfirrmann grade was significantly correlated with ROI's 2-5 from T2* maps, as well as the transition zone slope and T2* intensity area (Figure 5.2, Table 5.2). Recall that the ROI 1, the only non-significant correlation is located at the anterior annulus fibrosus of a mid-sagittal plane section.

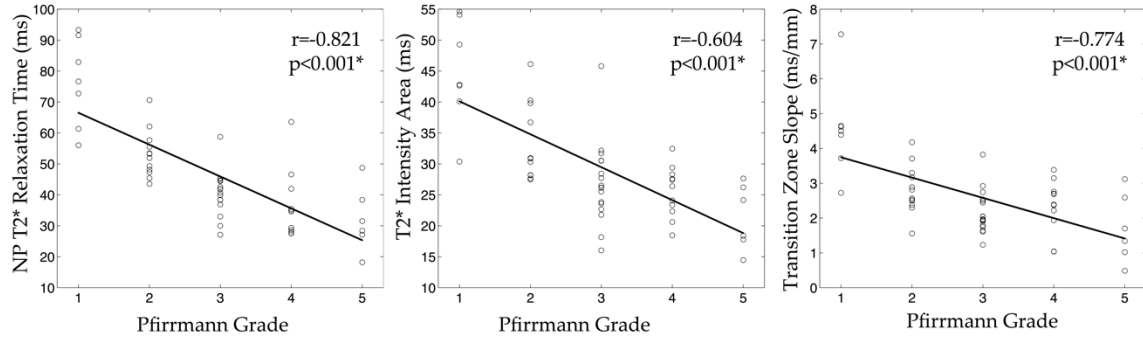


Figure 5.2. Correlation between T2* Imaging Parameters and Pfirrmann Grade.
 A significant correlation was found between the nucleus pulposus average T2* relaxation time, T2* Intensity Area, and the Transition Zone Slope with Pfirrmann Grade.

Table 5.2. Correlations between T2* Imaging Parameters and Pfirrmann Grade

	Pfirrmann Grade	
	r	p
Transition Zone Slope	-0.604	<0.001*
T2* Intensity Area	-0.774	<0.001*
ROI 1	0.001	0.996
ROI 2	-0.698	<0.001*
ROI 3	-0.821	<0.001*
ROI 4	-0.737	<0.001*
ROI 5	-0.381	<0.001*

5.2 BIOCHEMICAL CONTENT

Eighteen intervertebral discs, including only the L4-L5 level were analyzed further to measure their biochemical content and understand changes that occur in response to degeneration. The mean T2* relaxation time was positively correlated with sulfated-

glycosaminoglycan normalized by dry weight in all five corresponding regions: nucleus pulposus and inner, outer, anterior, and posterior annulus fibrosus (Table 5.3). This relationship was particularly strong in the NP ($r=0.944$; $p<0.001$) and inner AF ($r=0.782$; $p<0.001$) (Figure 5.3).

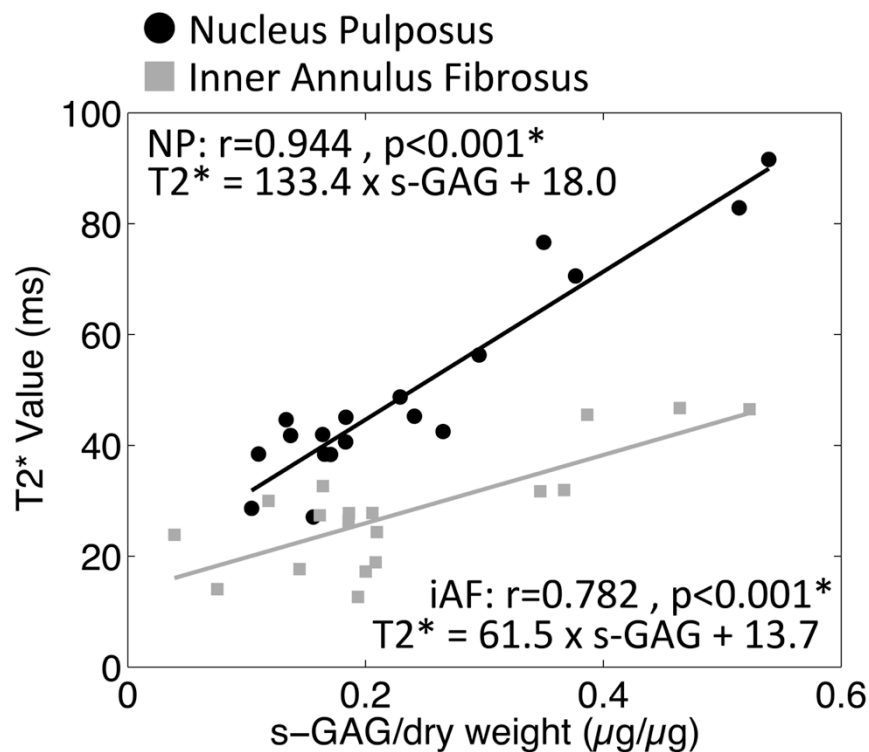


Figure 5.3. Correlation between T2* Relaxation Time and Glycosaminoglycan Content.

Circles indicate the Nucleus Pulposus and squares inner annulus fibrosus. Each correlation was found to be strongly significant ($p<0.001$).

Hydroxyproline, a relative measure of collagen content, normalized to total protein was only significantly correlated with the outer AF ($r=-0.568$; $p=0.014$), when hydroxyproline was normalized to s-GAG a significant negative correlation in the anterior AF ($r=-0.612$; $p=0.007$) was observed. Water content (% H₂O) was significantly correlated with T2* value in the posterior AF region only ($r=0.572$; $p=0.013$). All metrics were found to be significantly correlated with the corresponding T2* relaxation time when all locations were combined.

Table 5.3. Correlations between T2* Relaxation Times (ms) and Biochemical Content
(*r*: Pearson's correlation coefficient; *p*: *p*-value * represents significance at *p*=0.05).

		T2* Relaxation Time (ms)					
		NP	iAF	oAF	aAF	pAF	All
s-GAG/dry weight	r	0.944	0.782	0.647	0.569	0.474	0.586
	p	<0.001*	<0.001*	0.004*	0.014*	0.047*	<0.001*
Hydroxyproline/ Total Protein	r	0.071	0.322	-0.568	-0.153	0.226	-0.217
	p	0.778	0.193	0.014*	0.543	0.368	0.040*
Hydroxyproline/ s-GAG	r	-0.366	-0.354	-0.309	-0.612	0.414	-0.351
	p	0.135	0.149	0.212	0.007*	0.089	0.001*
Water Content	r	0.465	0.330	0.341	0.032	0.572	0.427
	p	0.052	0.181	0.166	0.900	0.013*	<0.001*

Similar trends were observed when comparing the biochemical analysis to Pfirrmann Grade (Table 5.6). However, the strength of the correlational coefficients is lower. Other T2* imaging metrics of disc health, Transition Zone Slope and T2* Intensity Area, displayed similar results, shown in Table 5.4 and Table 5.5, respectively.

Table 5.4. Correlations between Transition Zone Slope and Biochemical Content
(*r*: Pearson's correlation coefficient; *p*: *p*-value * represents significance at *p*=0.05).

		Transition Zone Slope					
		NP	iAF	oAF	aAF	pAF	All
s-GAG/dry weight	r	0.732	0.594	0.569	0.443	0.548	0.564
	p	0.001*	0.009*	0.014*	0.066	0.019*	<0.001*
Hydroxyproline/ Total Protein	r	0.224	0.471	0.167	0.336	-0.028	0.177
	p	0.372	0.048*	0.508	0.173	0.913	0.096
Hydroxyproline/ s-GAG	r	0.002	-0.236	-0.189	-0.177	-0.382	-0.157
	p	0.993	0.347	0.452	0.481	0.118	0.140
Water Content	r	0.410	0.459	-0.015	-0.079	0.129	0.175
	p	0.091	0.055	0.953	0.755	0.611	0.100

Table 5.5. Correlations between T2* Intensity Area and Biochemical Content
*(r: Pearson's correlation coefficient; p: p-value * represents significance at p=0.05).*

		T2* Intensity Area					
		NP	iAF	oAF	aAF	pAF	All
s-GAG/dry weight	r	0.903	0.819	0.834	0.755	0.726	0.785
	p	<0.001*	<0.001*	<0.001*	<0.001*	0.001*	<0.001*
Hydroxyproline/ Total Protein	r	0.032	0.520	-0.100	0.216	0.058	0.125
	p	0.900	0.027*	0.694	0.390	0.818	0.241
Hydroxyproline/ s-GAG	r	-0.361	-0.336	-0.238	-0.303	-0.385	-0.266
	p	0.142	0.173	0.341	0.221	0.115	0.011*
Water Content	r	0.463	0.356	0.213	0.080	0.158	0.236
	p	0.053	0.148	0.396	0.752	0.531	0.025*

Table 5.6. Correlations between Pfirrmann Grade and Biochemical Content
*(r: Pearson's correlation coefficient; p: p-value * represents significance at p=0.05).*

		Pfirrmann Grade					
		NP	iAF	oAF	aAF	pAF	All
s-GAG/dry weight	r	-0.752	-0.725	-0.542	-0.485	-0.411	-0.574
	p	<0.001*	0.001*	0.020*	0.041*	0.091	<0.001*
Hydroxyproline/ Total Protein	r	0.297	-0.313	-0.036	-0.365	-0.016	-0.071
	p	0.231	0.206	0.889	0.136	0.950	0.506
Hydroxyproline/ s-GAG	r	0.349	0.548	-0.043	0.078	0.329	0.172
	p	0.156	0.019*	0.864	0.759	0.183	0.106
Water Content	r	-0.416	-0.361	-0.035	-0.118	0.108	-0.169
	p	0.086	0.141	0.890	0.640	0.671	0.112

5.3 LOCAL BIOMECHANICAL PROPERTIES

The same eighteen L4-L5 intervertebral discs underwent site-specific stress relaxation tests to understand the changes that occur in response to degeneration. T2* relaxation times of the NP, inner AF, and outer AF were significantly correlated with both excised strain ($r= 0.857, p< 0.001$; $r= 0.535, p= 0.022$; $r= 0.668, p= 0.002$) and residual stress ($r= 0.816, p< 0.001$; $r= 0.516, p= 0.028$; $r= 0.485, p= 0.041$). The posterior AF T2* time was also correlated with residual stress ($r= 0.527, p= 0.025$). The correlational plots between

the T2* relaxation time and corresponding excised strain and residual stress in the NP and iAF can be seen in Figure 5.4.

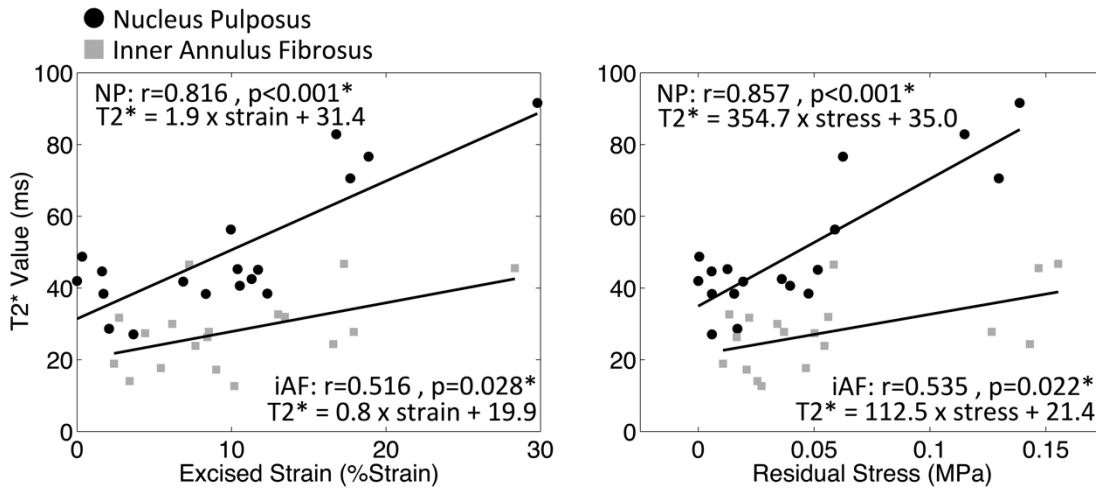


Figure 5.4. Correlations between T2* Relaxation time and Excised Strain and Residual Stress.

Circles represent the nucleus pulposus and squares the inner annulus fibrosus.

The following tables display the correlational coefficients (r) and resultant p-value (p) between the correlations between local biomechanical properties and T2* Relaxation Time (Table 5.7), Transition Zone Slope (Table 5.8), T2* Intensity Area (Table 5.9), and Pfirrmann Grade (Table 5.10). All imaging metrics were correlated with residual stress and excised strain in the NP, with the strongest correlations being from T2* relaxation parameters. Site-specific T2* relaxation times predicted changes in the stress and strain of the disc in the NP, iAF, and oAF. The posterior AF T2* time was also correlated with residual stress. No significant correlations in Equilibrium Stress or Elastic Modulus were determined. The Equilibrium Modulus was significantly correlated with the T2* Relaxation time in the oAF.

Regarding the viscoelastic stress relaxation function (Equation 7), there were no changes observed in the spectrum magnitude (g). The most prominent changes occurred with the medium time constant (τ_M), which decreased with diminishing disc health.

Table 5.7. Correlations between T2* Relaxation Times and Local Biomechanics
(r: Pearson's correlation coefficient; p: p-value * represents significance at p=0.05).

		T2* Relaxation Time (ms)					
		NP	iAF	oAF	aAF	pAF	All
Residual Stress (MPa)	r	0.857	0.535	0.668	0.242	0.527	0.347
	p	<0.001*	0.022*	0.002*	0.332	0.025*	0.001*
Excised Strain (% Strain)	r	0.816	0.516	0.485	-0.040	0.405	0.412
	p	<0.001*	0.028*	0.041*	0.874	0.095	<0.001*
Equilibrium Modulus (MPa)	r	0.270	0.114	0.506	0.072	0.269	0.031
	p	0.279	0.653	0.032*	0.776	0.280	0.774
τ_S (sec)	r	-0.393	-0.364	0.023	0.132	-0.247	-0.122
	p	0.107	0.137	0.929	0.603	0.324	0.251
τ_m (sec)	r	-0.518	-0.530	0.015	-0.202	-0.355	-0.209
	p	0.028*	0.024*	0.952	0.420	0.148	0.048*
τ_l (sec)	r	-0.157	-0.381	0.176	-0.372	-0.115	-0.116
	p	0.535	0.119	0.484	0.128	0.650	0.276

Table 5.8. Correlations between Transition Zone Slope and Local Biomechanics
(r: Pearson's correlation coefficient; p: p-value * represents significance at p=0.05).

		Transition Zone Slope					
		NP	iAF	oAF	aAF	pAF	All
Residual Stress (MPa)	r	0.545	0.132	0.052	0.156	0.590	0.298
	p	0.019*	0.603	0.838	0.536	0.010*	0.004*
Excised Strain (% Strain)	r	0.530	0.280	0.179	0.072	0.573	0.349
	p	0.024*	0.260	0.477	0.776	0.010*	0.001*
Equilibrium Modulus (MPa)	r	0.053	-0.345	0.038	-0.369	0.121	-0.051
	p	0.834	0.161	0.881	0.131	0.633	0.631
τ_S (sec)	r	-0.323	-0.374	-0.634	-0.004	0.036	-0.280
	p	0.190	0.127	0.005*	0.988	0.887	0.008*
τ_M (sec)	r	-0.597	-0.576	-0.784	-0.562	-0.274	-0.513
	p	0.009*	0.012*	<0.001*	0.015*	0.272	<0.001*
τ_L (sec)	r	-0.339	-0.484	-0.583	-0.458	-0.398	-0.411
	p	0.168	0.042*	0.011*	0.056	0.101	<0.001*

Table 5.9. Correlations between T2* Intensity Area and Local Biomechanics
*(r: Pearson's correlation coefficient; p: p-value * represents significance at p=0.05).*

		T2* Intensity Area					
		NP	iAF	oAF	aAF	pAF	All
Residual Stress (MPa)	r	0.876	0.451	0.322	0.291	0.881	0.568
	p	<0.001*	0.060	0.193	0.241	<0.001*	<0.001*
Excised Strain (% Strain)	r	0.822	0.472	0.268	0.081	0.667	0.490
	p	<0.001*	0.048*	0.282	0.750	0.002*	<0.001*
Equilibrium Modulus (MPa)	r	0.273	-0.017	0.173	0.025	0.454	0.202
	p	0.272	0.946	0.492	0.921	0.058	0.056
τ_S (sec)	r	-0.395	-0.459	-0.253	-0.165	-0.351	-0.322
	p	0.104	0.055	0.311	0.512	0.154	0.002*
τ_M (sec)	r	-0.503	-0.657	-0.512	-0.699	-0.486	-0.513
	p	0.033*	0.003*	0.030*	0.001*	0.041*	<0.001*
τ_L(sec)	r	-0.089	-0.488	-0.530	-0.406	-0.193	-0.311
	p	0.727	0.040*	0.024*	0.094	0.442	0.003*

Table 5.10. Correlations between Pfirrmann Grade and Local Biomechanics
*(r: Pearson's correlation coefficient; p: p-value * represents significance at p=0.05).*

		Pfirrmann Grade					
		NP	iAF	oAF	aAF	pAF	All
Residual Stress (MPa)	r	-0.793	-0.373	-0.044	-0.084	-0.754	-0.419
	p	<0.001*	0.128	0.861	0.741	<0.001*	<0.001*
Excised Strain (% Strain)	r	-0.824	-0.286	0.028	-0.070	-0.659	-0.400
	p	<0.001*	0.250	0.911	0.782	0.003*	<0.001*
Equilibrium Modulus (MPa)	r	-0.369	0.070	0.047	0.286	-0.409	-0.112
	p	0.132	0.783	0.854	0.250	0.092	0.295
τ_S (sec)	r	0.389	0.368	0.341	0.033	0.143	0.264
	p	0.110	0.133	0.167	0.896	0.573	0.012*
τ_M (sec)	r	0.480	0.588	0.644	0.445	0.298	0.459
	p	0.044*	0.010*	0.004*	0.064	0.230	<0.001*
τ_L (sec)	r	0.058	0.434	0.599	0.372	0.152	0.297
	p	0.818	0.072	0.009*	0.128	0.548	0.004*

5.4 LOCATION DEPENDENT CHANGES IN DISC HEALTH

In the previous sections, the biochemical and biomechanical properties were related to continuous disc health data location by location. In this section, the data will be crosscut

grouped based on three categories of disc health: ‘healthy’, ‘moderate’, and ‘severe’. This post-hoc analysis will reveal location dependent changes that occur within the disc during degeneration. The metrics that were investigated are as follows: T2* Relaxation Times, Residual Stress and Strain, sulfated-Glycosaminoglycan content, and hydroxyproline content normalized by total protein. Differences in the mean values were analyzed between three stages of disc degeneration: healthy, moderate, and severe. The data is displayed in the subsequent the series of Figures following the general format of Figure 5.5, which illustrates the five regions of interest investigated. The color of the bar is indicative of the average T2* relaxation time in that ROI at that stage of degeneration.

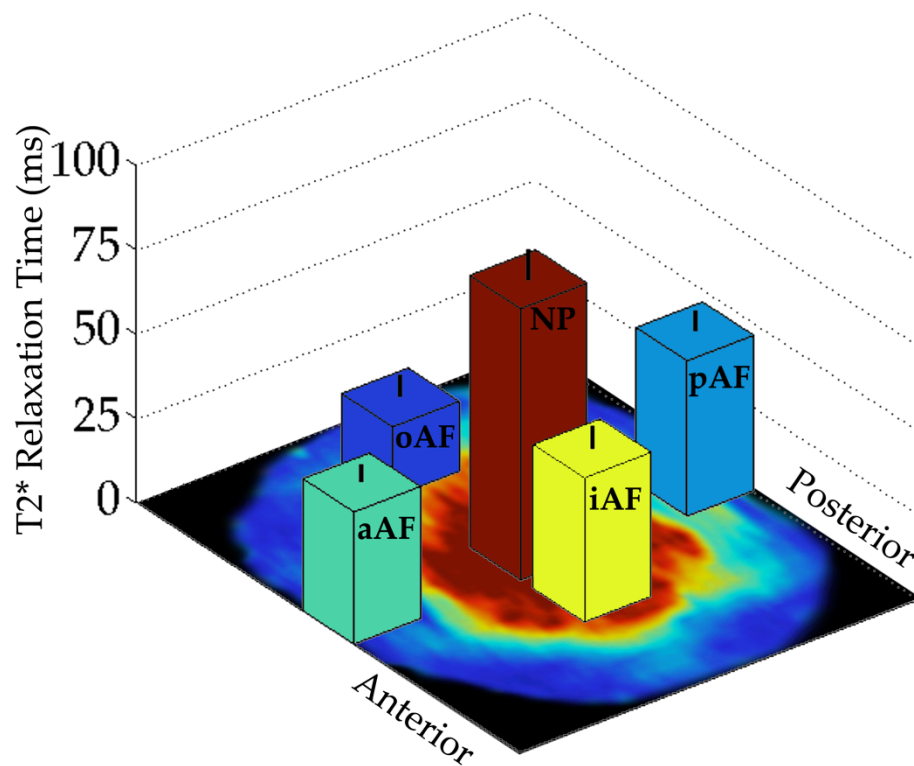


Figure 5.5. Example Plot with Locations Labeled.

The following plots follow the above format, while showing location based differences in Healthy, Moderate, and Severely degenerated discs.

The T2* relaxation time, Figure 5.6, in healthy intervertebral discs is significantly higher in the NP and lower in the outer lateral AF, than any other region ($p < 0.020$). This spatial

distribution remains steady in the moderately degenerated, but the absolute T2* relaxation times are significantly lower ($p < 0.024$). In severely degenerated discs, the oAF remains significantly lower than all other regions ($p < 0.032$), but the NP is similar to the anterior and posterior AF regions.

The distribution of residual stress (Figure 5.7) is relatively similar across all regions, except a significant decrease was observed between the NP and aAF region in the healthy discs ($p = 0.017$). There is a trend of diminished stress in all regions with degeneration. There were no regionally based differences in the moderate discs, but a difference between iAF and pAF in the severe group ($p = 0.047$).

The excised strain (Figure 5.8) was highest in the healthy discs and diminished with degeneration. The aAF exhibited the lowest strains and was significantly different than all regions except iAF in the healthy group ($p < 0.042$). The severe discs displayed a significant difference in the excised strain between the pAF and oAF ($p = 0.013$).

The biochemical content also exhibited location-dependent changes in disc health. The s-GAG content (Figure 5.9) was highest in the healthy discs and also diminished with degeneration. The oAF had significantly lower s-GAG content than the NP, iAF, and pAF in healthy discs ($p < 0.039$), but was only different than the NP in the moderate group ($p = 0.034$). No differences were observed in severe cases. The hydroxyproline content, normalized by total protein, was significantly lower in the NP in all stages of degeneration ($p < 0.040$) (Figure 5.10).

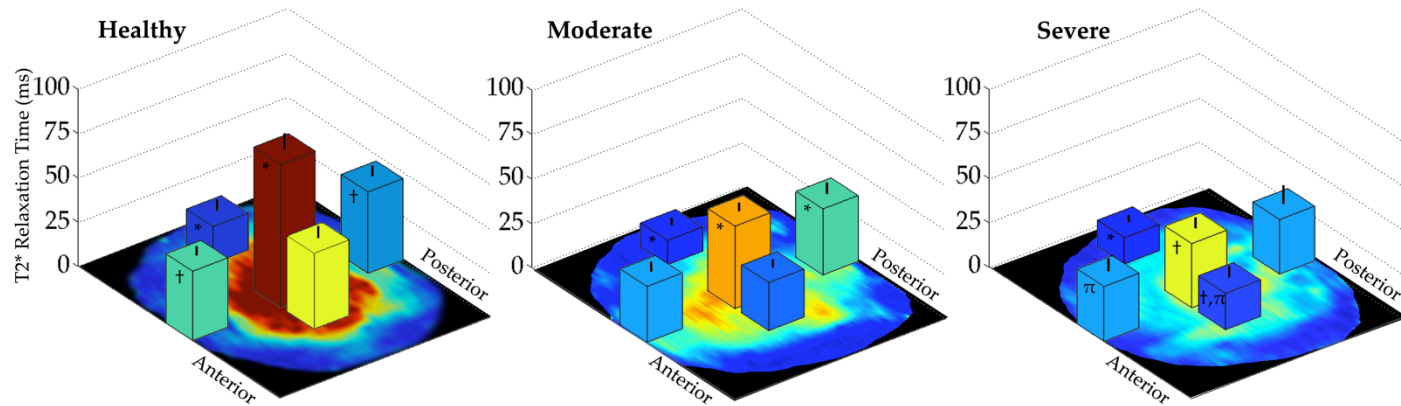


Figure 5.6. Location Based Differences in T2* Relaxation Times for Healthy, Moderate, and Severely Degenerated Discs. An * denotes a significant difference between labeled location and all other locations. All other symbols indicate a significant difference between corresponding symbols within a level of degeneration severity ($p < 0.05$).

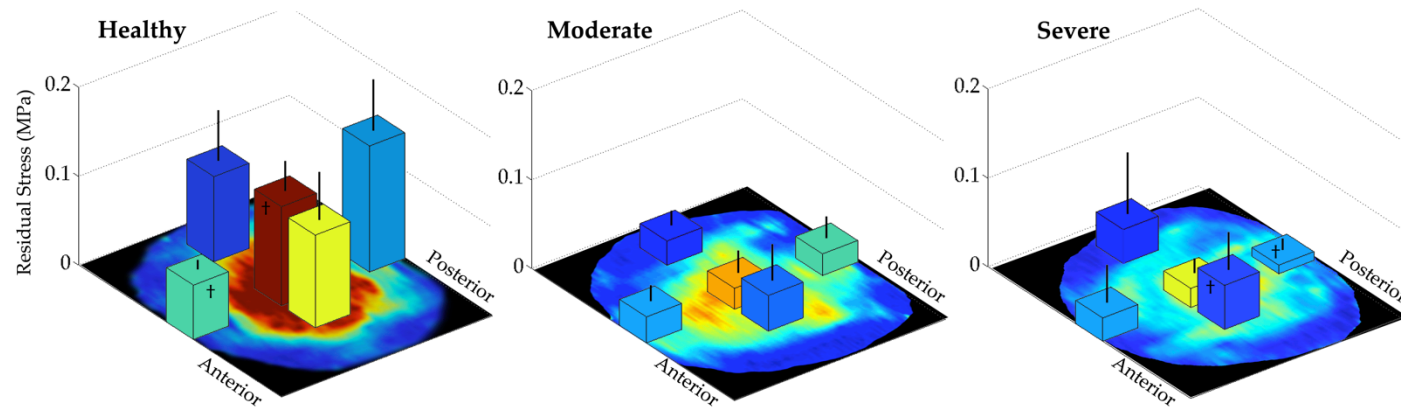


Figure 5.7. Location Based Differences in Residual Stress for Healthy, Moderate, and Severely Degenerated Discs. All symbols indicate a significant difference between corresponding symbols within a level of degeneration severity ($p < 0.05$).

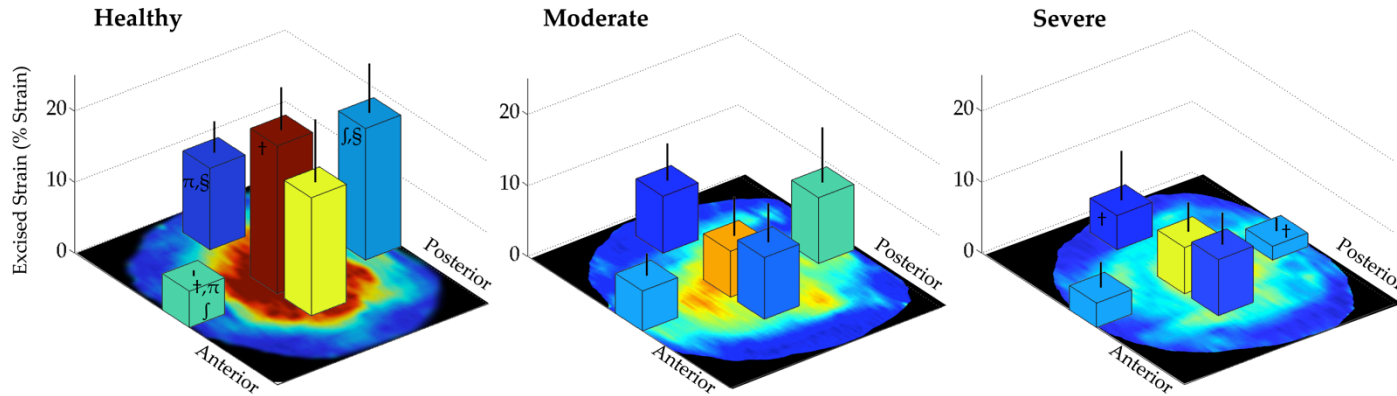


Figure 5.8. Location Based Differences in Excised Strain for Healthy, Moderate, and Severely Degenerated Discs. All symbols indicate a significant difference between corresponding symbols within a level of degeneration severity ($p < 0.05$).

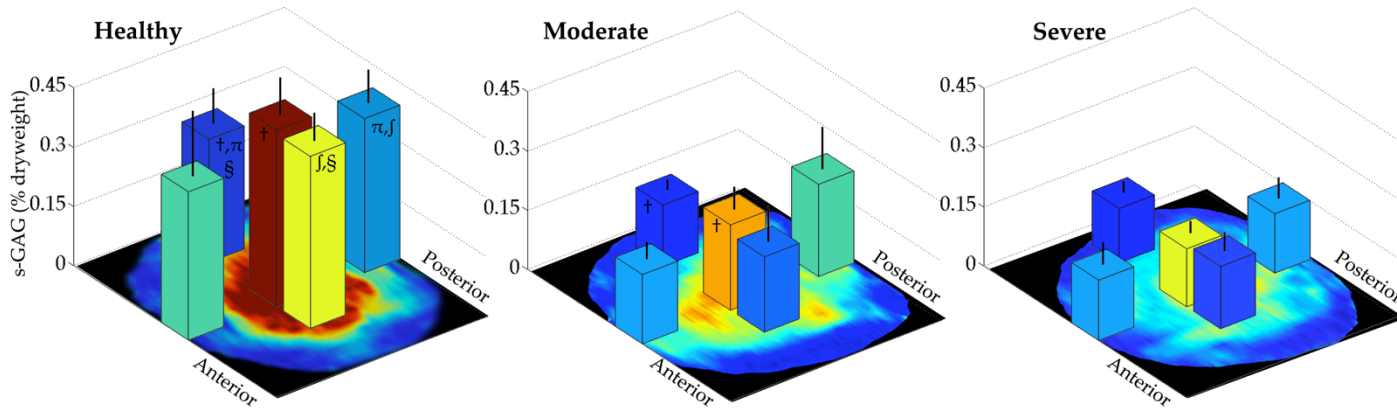


Figure 5.9. Location Based Differences in Glycosaminoglycan Content for Healthy, Moderate, and Severely Degenerated Discs. All symbols indicate a significant difference between corresponding symbols within a level of degeneration severity ($p < 0.05$).

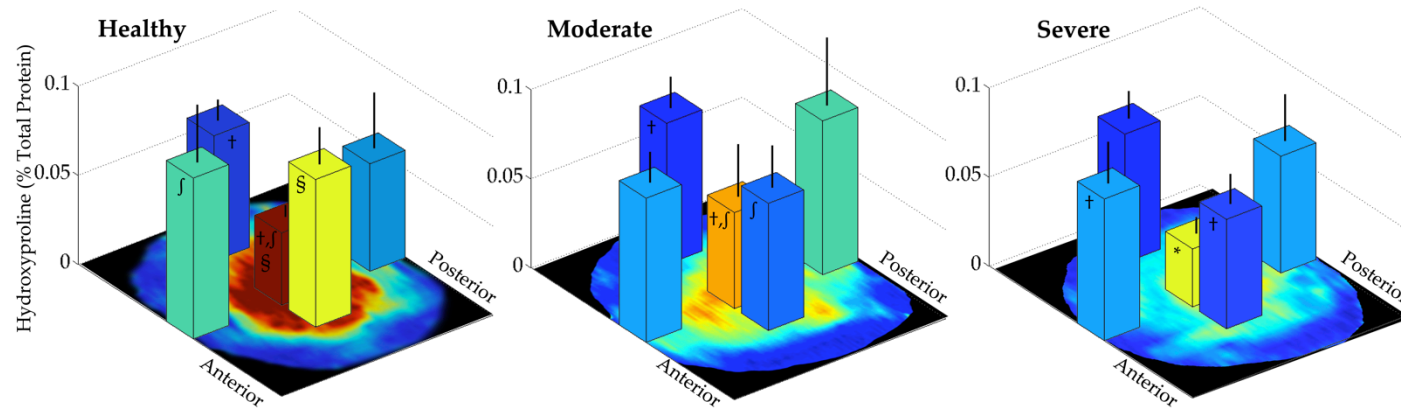


Figure 5.10. Location Based Differences in Hydroxyproline Content for Healthy, Moderate, and Severely Degenerated Discs. An * denotes a significant difference between labeled location and all other locations. All other symbols indicate a significant difference between corresponding symbols within a level of degeneration severity ($p < 0.05$).

The following plots contain the same information presented before spatially, but they are displayed here linearly for ease of comparison between grades within each location. The T2* relaxation time in the NP decreases significantly from healthy to moderate to severe ($p < 0.025$). The iAF T2* relaxation time in healthy discs was significantly higher than the moderate and severe ($p < 0.003$), while the healthy pAF relaxation time was only statistically higher than the severe discs ($p = 0.030$) (Figure 5.11). No other differences were found.

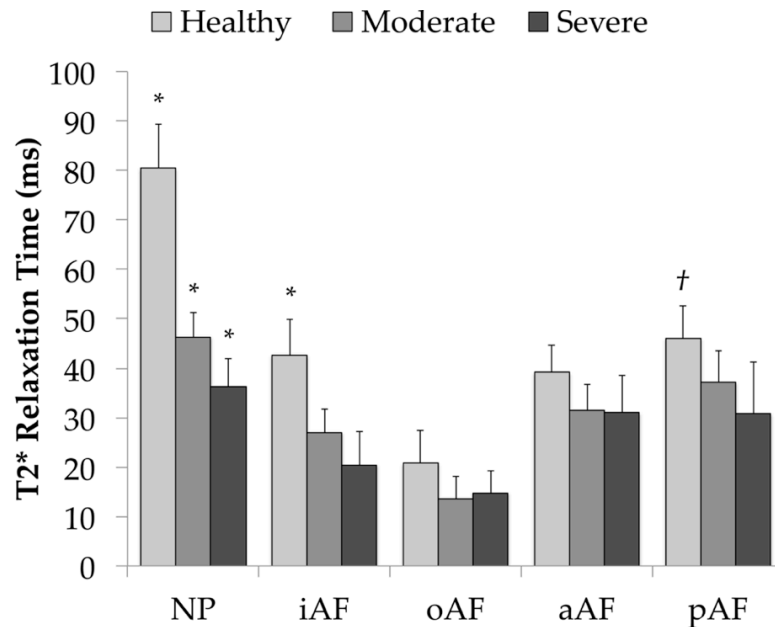


Figure 5.11. T2* Relaxation Time as a Function of Disc Health at Different Locations. An * denotes a significant difference between all groups of disc health. An † denotes a significant difference between 'Healthy' and 'Severe' degenerated discs ($p < 0.05$).

The residual stress and excised strain in the healthy NP was significantly greater than the moderate and severe discs ($p < 0.001$), shown in Figure 5.11 and Figure 5.12, respectively. The residual stress in the healthy posterior annular region also displayed this relationship ($p < 0.001$), but the excised strain was only different between the healthy and severe groups ($p = 0.001$).

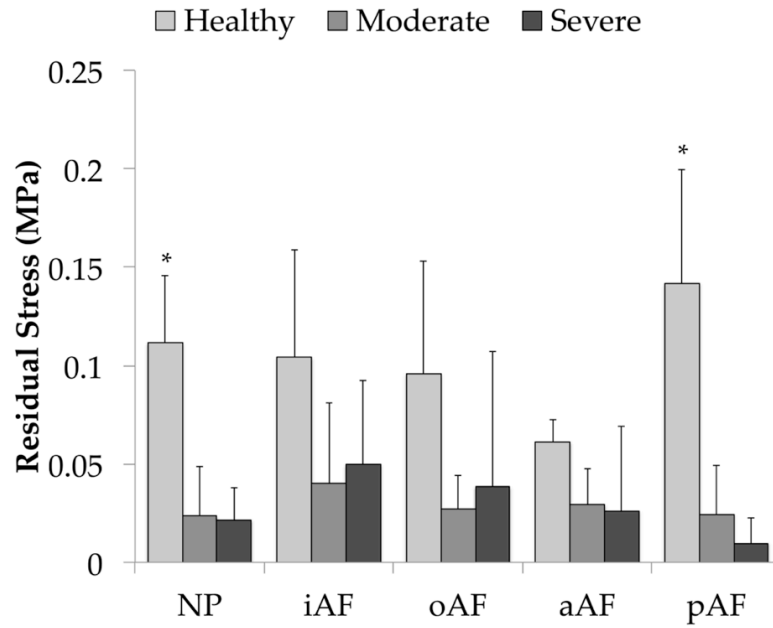


Figure 5.12. T2* Residual Stress as a Function of Disc Health at Different Locations. An * denotes a significant difference between all groups of disc health ($p < 0.05$).

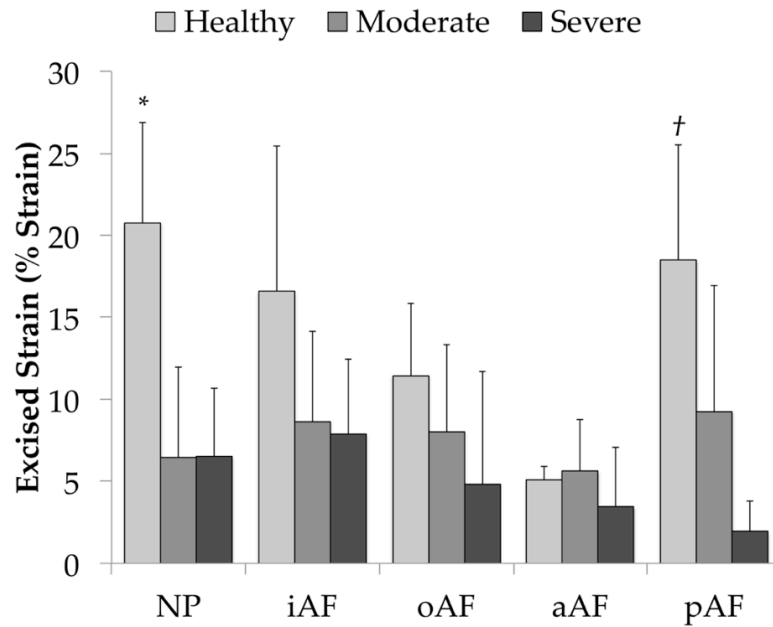


Figure 5.13. Excised Strain as a Function of Disc Health at Different Locations. An * denotes a significant difference between all groups of disc health. An † denotes a significant difference between 'Healthy' and 'Severe' degenerated discs ($p < 0.05$).

The sulfated-glycosaminoglycan content displayed similar relationships in all regions with respect to degeneration (Figure 5.14) where a significantly higher s-GAG content was observed in the healthy discs compared to both the moderate and severely degenerated discs ($p < 0.001$). No significant changes in hydroxyproline (% total protein) were observed in any locations with respect to degeneration (Figure 5.15).

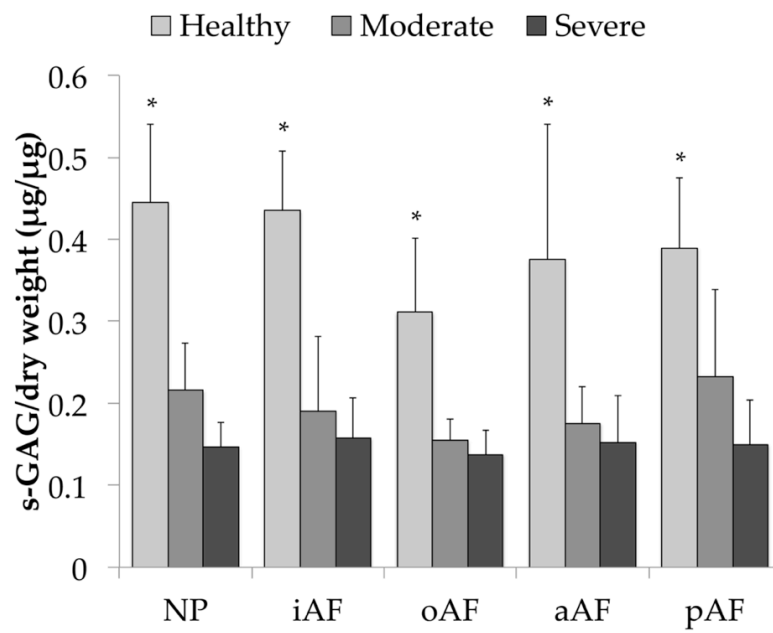


Figure 5.14. Glycosaminoglycan Content as a Function of Disc Health at Different Locations.

An * denotes a significant difference between all groups of disc health ($p < 0.05$).

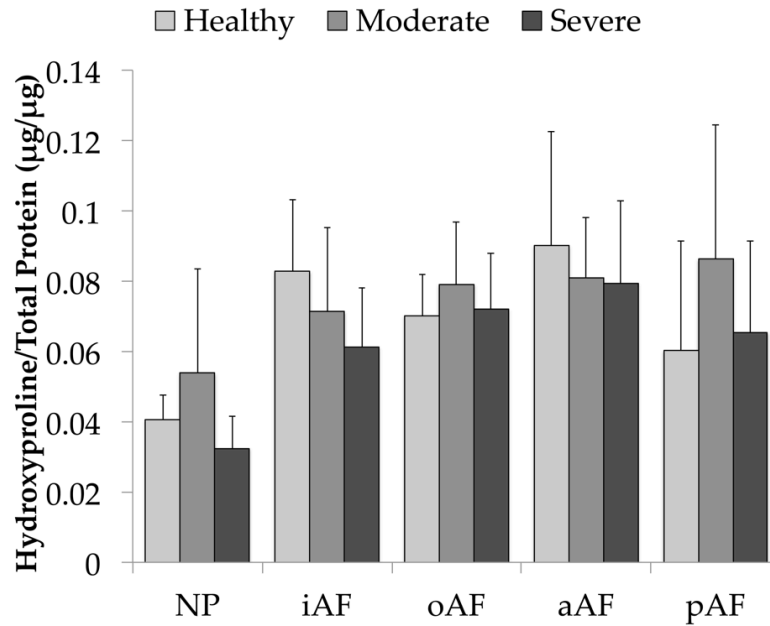


Figure 5.15. Hydroxyproline Content as a Function of Disc Health at Different Locations.

No significant changes were observed.

5.5 FUNCTIONAL MECHANICAL OUTCOMES

All 54 functional spinal units from L3-S1 were subjected to pure moment bending and the output range of motion measurements and stiffness of the functional spinal unit are correlated with imaging parameters of the intervertebral disc and displayed in Table 5.11 and Table 5.12, respectively. Pfirrmann grade was significantly correlated only with LB NZR ($r = 0.468$, $p = 0.001$) and stiffness ($r = 0.362$, $p = 0.007$). T2* Intensity Area and the Transition Zone Slope were also significantly correlated with LB NZR ($r = -0.378$, $p = 0.005$; $r = -0.402$, $p = 0.003$) and stiffness ($r = -0.314$, $p = 0.022$; $r = -0.300$, $p = 0.029$). T2* Intensity Area was also correlated with LB ROM ($r = 0.312$, $p = 0.023$). In addition, T2* Intensity Area and the Transition Zone Slope were significantly correlated with Flexion ROM ($r = 0.334$, $p = 0.015$; $r = 0.414$, $p = 0.002$), NZR ($r = -0.305$, $p = 0.028$; $r = -0.352$, $p = 0.010$), and stiffness ($r = -0.278$, $p = 0.044$; $r = -0.306$, $p = 0.026$). Several regions of

interest also correlated with these variables as well as AR ROM ($r = 0.292$, $p = 0.034$) and AR stiffness ($r = 0.371$, $p = 0.006$).

Table 5.11. Correlations between T2* Parameters and Range of motion and Neutral Zone Ratio

(*r*: Pearson's correlation coefficient; *p*: p-value * represents significance at $p=0.05$).

			Transition Zone Slope	T2* Intensity Area	ROI 1	ROI 2	ROI 3	ROI 4	ROI 5	Pfirschmann Grade
Flexion	% FE ROM	r	0.414	0.334	0.118	0.322	0.311	0.353	0.090	-0.220
		p	0.002*	0.015*	0.398	0.019*	0.024*	0.01*	0.521	0.109
NZR		r	-0.352	-0.305	.084	-0.187	-0.323	-0.293	-0.114	0.136
		p	0.010*	0.028*	.554	0.185	0.019*	0.035*	0.422	0.332
Lateral Bending	ROM	r	0.179	0.312	0.164	0.206	0.262	0.188	0.335	-0.223
		p	0.199	0.023*	0.241	0.139	0.058	0.177	0.014*	0.105
NZR		r	-0.402	-0.378	-0.346	-0.363	-0.406	-0.399	-0.258	0.468
		p	0.003*	0.005*	0.011*	0.007*	0.003*	0.003*	0.062	0.001*
Axial Rotation	ROM	r	-0.143	-0.148	-0.061	-0.292	-0.130	-0.191	0.027	0.193
		p	0.307	0.290	0.667	0.034*	0.355	0.171	0.848	0.162
NZR		r	0.136	0.036	0.128	0.151	0.055	0.099	-0.063	0.071
		p	0.332	0.799	0.361	0.280	0.696	0.481	0.653	0.608

Table 5.12. Correlations between T2* Parameters and Bending Stiffness

(*r*: Pearson's correlation coefficient; *p*: p-value * represents significance at $p=0.05$).

			Transition Zone Slope	T2* Intensity Area	ROI 1	ROI 2	ROI 3	ROI 4	ROI 5	Pfirschmann Grade
Stiffness (deg/Nm)	Flex	r	-0.306	-0.278	0.105	-0.079	-0.308	-0.163	-0.228	0.230
		p	0.026*	0.044*	0.454	0.574	0.025*	0.244	0.101	0.094
	Ext.	r	0.002	0.191	0.106	0.249	0.126	0.172	-0.021	-0.031
		p	0.988	0.170	0.451	0.072	0.368	0.217	0.879	0.822
LB	r	-0.300	-0.314	-0.269	-0.292	-0.341	-0.197	-0.186	0.362	
	p	0.029*	0.022*	0.052	0.034*	0.013*	0.157	0.182	0.007*	
AR	r	0.276	0.241	0.186	0.270	0.233	0.371	0.229	-0.208	
	p	0.043*	0.082	0.182	0.051	0.093	0.006*	0.099	0.132	

Figure 5.16 shows representative correlational plots between flexion stiffness and NZR and Pfirschmann Grade, Transition Zone Slope, and T2* Intensity Area. No statistical

correlation was determined between Pfirrmann Grade and either stiffness or ROM. There was a significant correlation, however, between ROM and stiffness with both Transition Zone Slope and T2* Intensity Area.

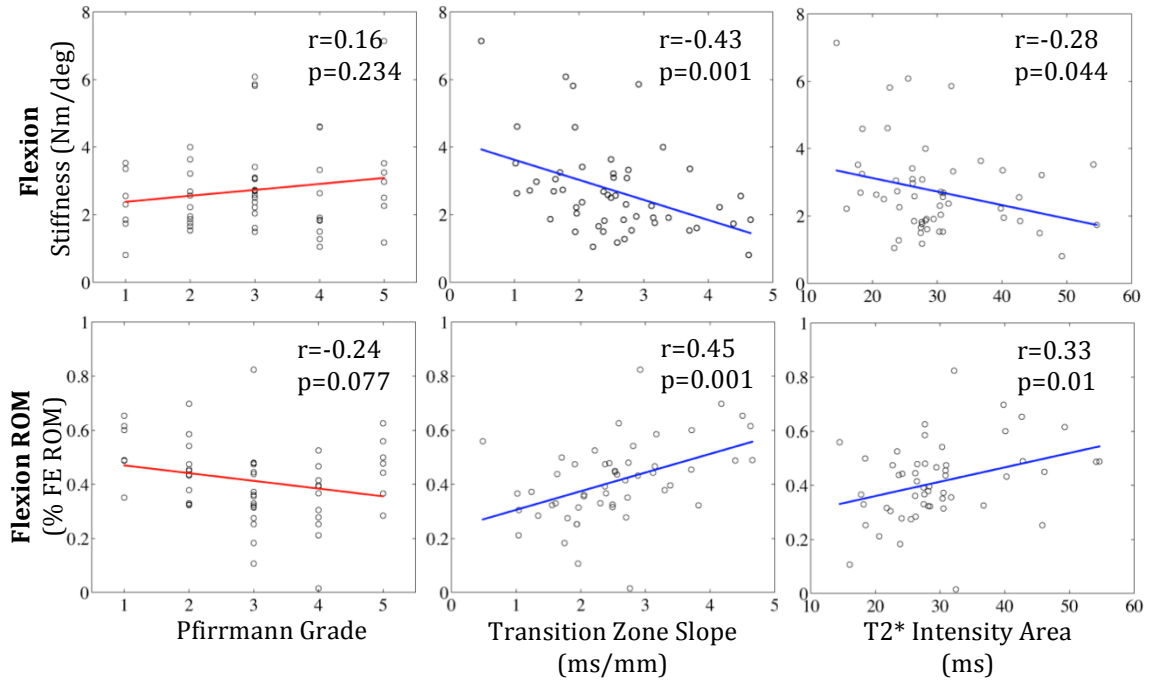


Figure 5.16. Correlational Plots Between Flexion Stiffness and Range of Motion with Disc Health.

Left: No significance was determined between flexion stiffness or flexion ROM and Pfirrmann grade. A significant correlation between both flexion stiffness and ROM with **(Middle)** Transition Zone Slope and **(Right)** T2* Intensity Area.

Figure 5.17 shows a similar set of correlational plots, displaying correlations between lateral bending stiffness and NZR with the NP T2* Relaxation Time, Transition Zone Slope, and T2* Intensity Area.

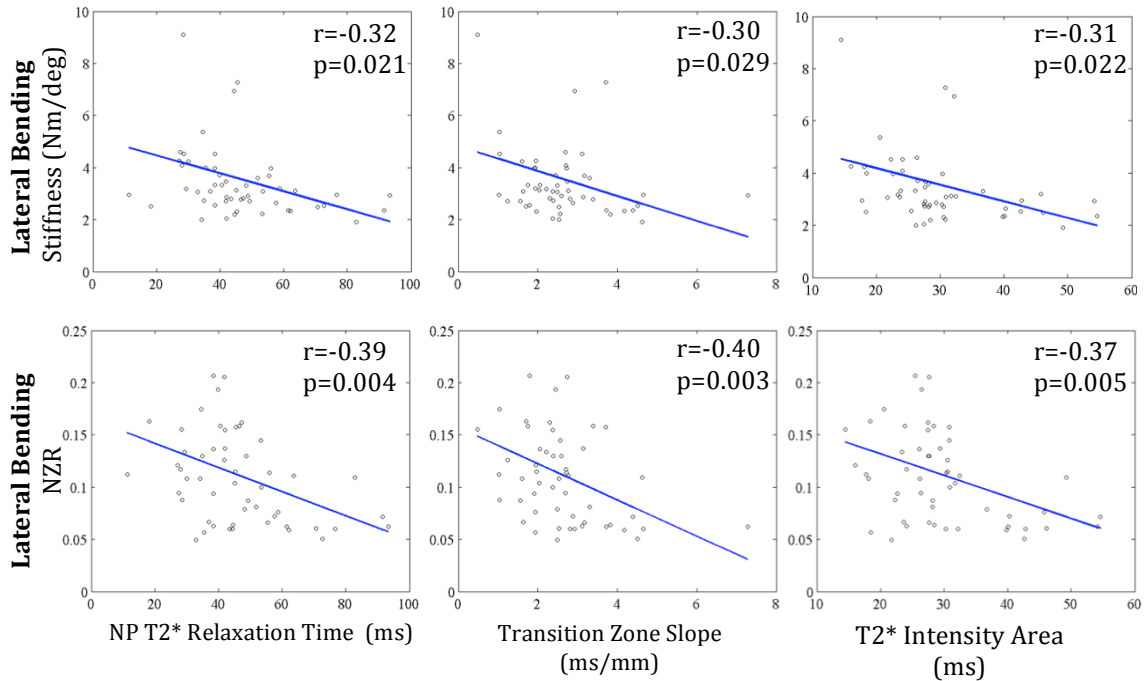


Figure 5.17. Correlational Plots Between Lateral Bending Stiffness and Neutral Zone Ratio with Disc Health.

Left: A significant correlation between both lateral bending stiffness and NZR with **(Left)** Average NP T2* Relaxation Time, **(Middle)** Transition Zone Slope and **(Right)** T2* Intensity Area.

5.6 ALTERATIONS IN HELICAL AXES

The functional mechanics of the lumbar spine have been shown above to be altered by disc health, however these are just scalar measures that simplify the end range of motion and stiffness. The orientation and location of the helical axes were computed for flexion, extension, and lateral bending for the L4-L5 spinal segment (18 functional spinal units) to understand the pathway of motion, and how it is affected by the quality of the intervertebral disc.

Specimens of all degeneration levels exhibited overall similar motion patterns for lateral bending, shown in a representative healthy specimen (Figure 5.18). More degenerative

specimens displayed exacerbated shift in the helical axis orientation, indicating more out-of-plane rotation at the end ranges of motion and a shift in the lateral location. A representative set of helical axes from a degenerated disc is shown in Figure 5.19.

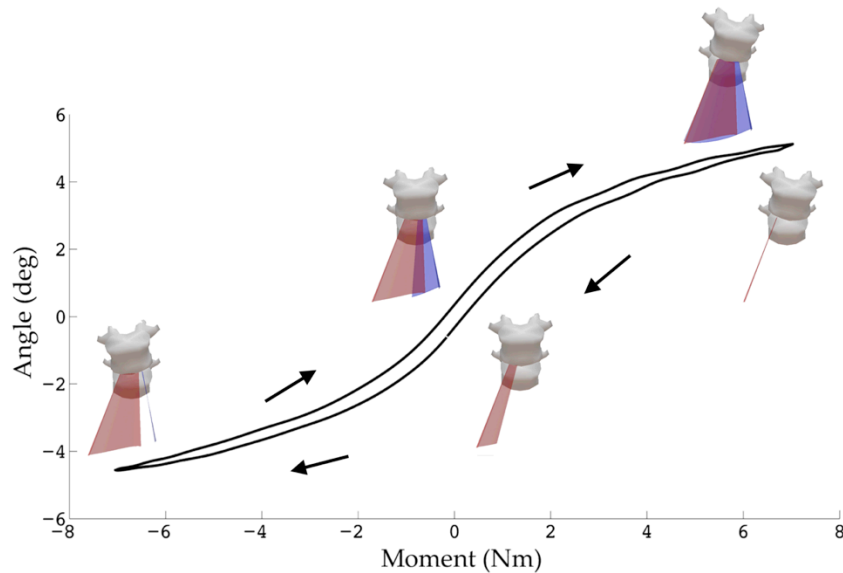


Figure 5.18. Representative Helical Axes from a Healthy Intervertebral Disc. The red surface displays the helical axes for right lateral bending, and blue from left lateral bending.

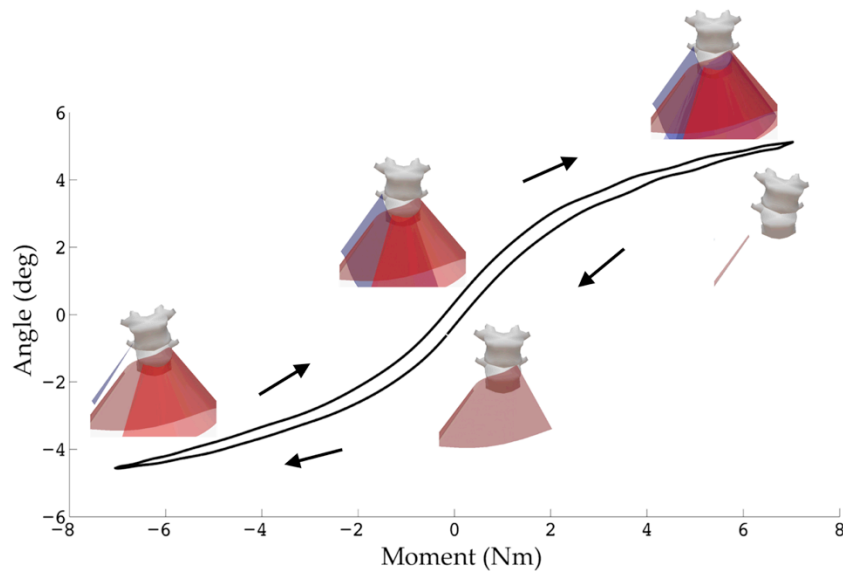


Figure 5.19. Representative Helical Axes from a Degenerative Intervertebral Disc. The red surface displays the helical axes for right lateral bending, and blue from left lateral bending.

Although qualitatively these vector sets appear to be different, to investigate the statistical significance, the helical axis parameters were correlated to imaging parameters of disc health over a 1 Nm window from -6.5 Nm to 6.5 Nm through the unloading and the loading curve. The following figures illustrate the alterations in the helical axis as a function of disc health. They all follow a similar format where a significant correlation between disc health and the helical axis parameter, over the 1 Nm window, is represented by a yellow bar. An example can be seen in Figure 5.20, where there is a significant correlation between the transition zone slope and the helical axis in the x direction over the 1 Nm window from 3.5 Nm to 4.5 Nm; thus the window is shaded to represent the significance.

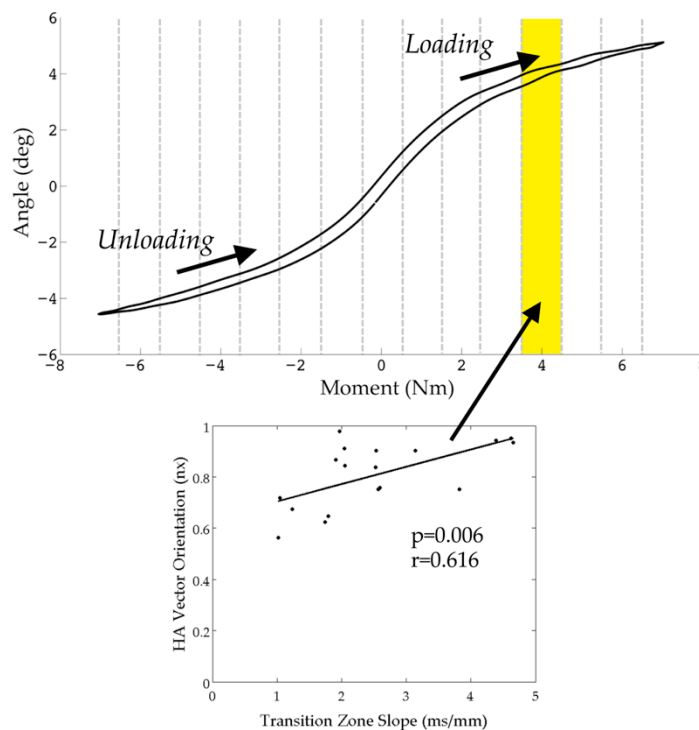


Figure 5.20. Example Angle- Moment Plot Illustrating a significant correlation between the helical axis parameter (nx) and measure of disc health (transition zone slope).

There is a significant correlation between the transition zone slope and the helical axis in the x direction over the 1 Nm window from 3.5 Nm to 4.5 Nm; thus the window is shaded to represent the significance.

There were no significant changes in the helical axis orientation or the IAR location for flexion or extension with respect to any of the measures of disc health. The most significant changes occurred during lateral bending. Recall that the primary orientation of the helical axis vector for lateral bending is in the anterior or x direction. Figure 5.21 shows how the helical axis unit vector in the anterior (x) direction changes as a function of disc health. All significant correlations found the orientation in the x direction to become less aligned when degeneration worsened. An example correlation can be seen in Figure 5.20, as the transition zone slope increases the orientation of the helical axis become more perpendicular to pure lateral bending, therefore as degeneration worsens there is significantly more out of plane motion. This was particularly prominent during the end ranges of motion, while the axes seem to be primarily aligned in the x-direction through the neutral zone.

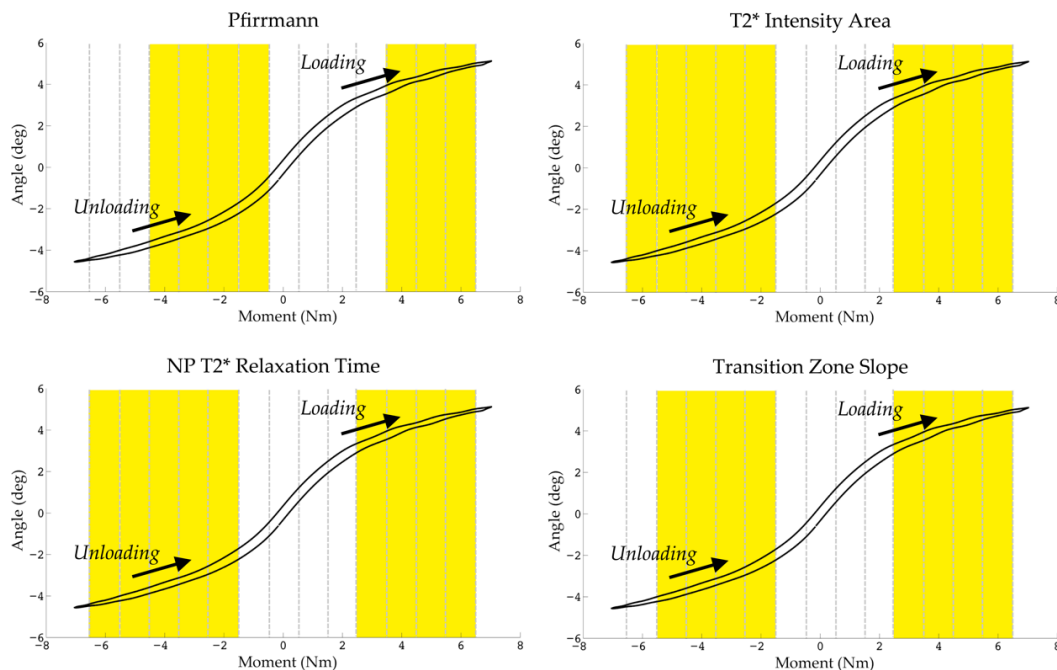


Figure 5.21. Primary Helical Axis Orientation (x-axis) During Lateral Bending. A yellow bar indicates a significant correlation with disc health parameter over the corresponding 1 Nm window ($p < 0.05$). All correlations revealed more out-of-plane motion with worsening degeneration.

Figure 5.22 and Figure 5.23 display the correlations between disc health and the helical axis in the z or the superior direction and y or the lateral direction, respectively. A rotation about the z-axis anatomically represents axial rotation, where rotation about the y-axis represents flexion/extension. As these figures illustrate, there is a significant change in both the y and z orientation of the helical axes during bending. Particularly, there is an observed axial rotation component following the neutral zone, then a flexion component at the very end ranges of motion. This was observed during both unloading and loading. Also, through the neutral zone, the more degenerative specimens underwent slight flexion compared to the healthier specimens.

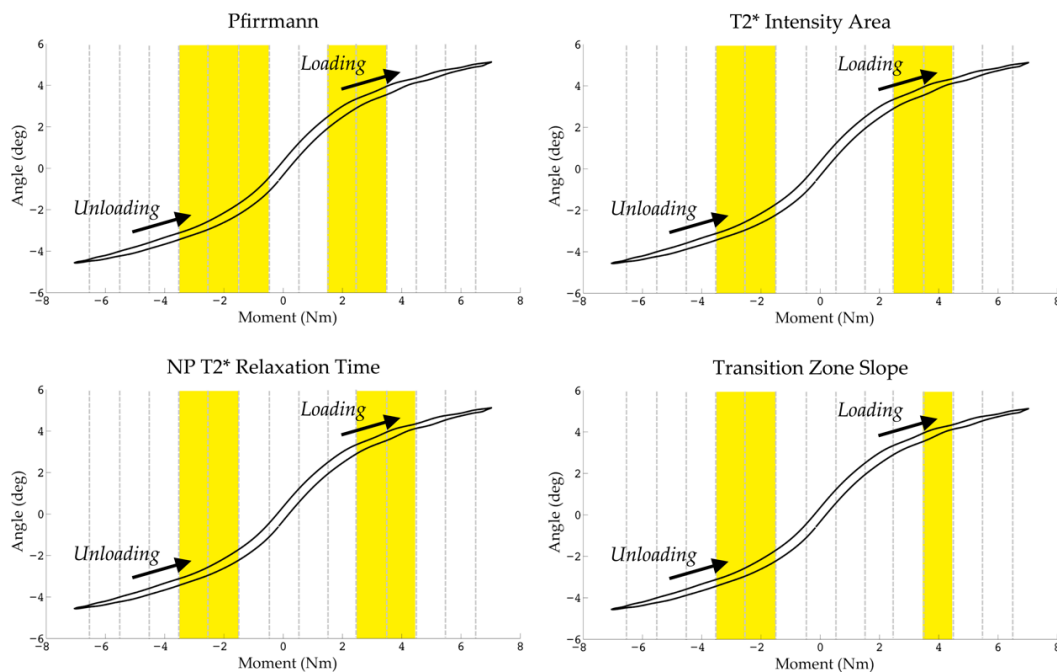


Figure 5.22. Changes in the Helical Axis Orientation (z-axis) During Lateral Bending. A yellow bar indicates a significant correlation with disc health parameter over the corresponding 1 Nm window ($p < 0.05$). All correlations revealed a stronger alignment of the helical axis in the z direction with worsening degeneration. This suggests an increased axial rotation component in the rotation during at the areas shaded in yellow.

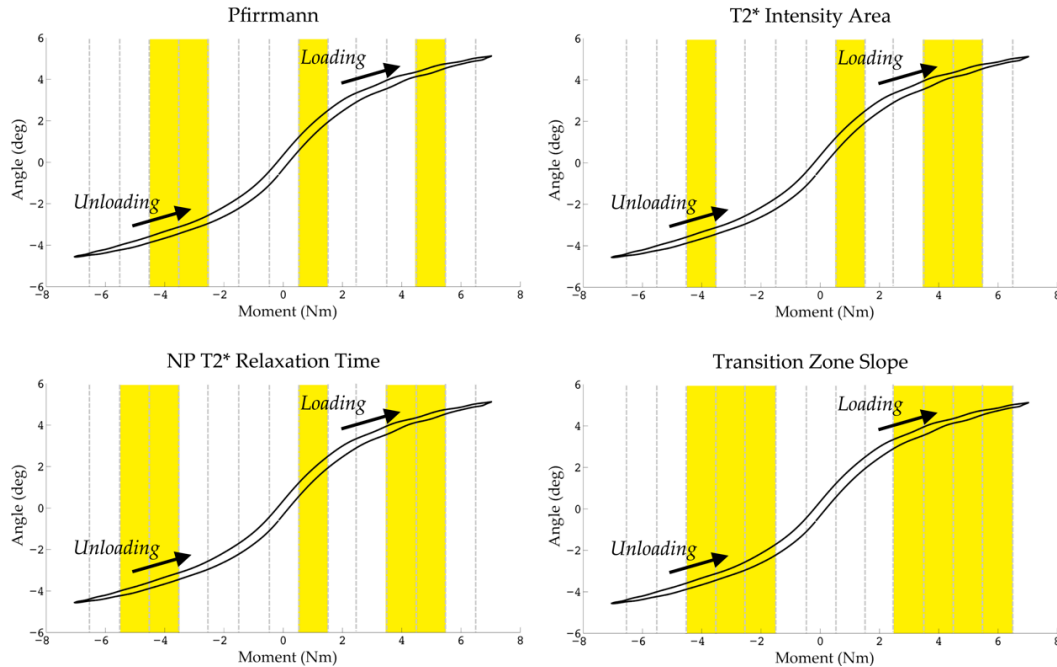


Figure 5.23. Changes in the Helical Axis Orientation (y-axis) During Lateral Bending. A yellow bar indicates a significant correlation with disc health parameter over the corresponding 1 Nm window ($p < 0.05$). All correlations revealed a stronger alignment of the helical axis in the y direction with worsening degeneration. This suggests an increased flexion component in the rotation during at the areas shaded in yellow.

The standard deviation of the primary component of the helical axis during lateral bending, x-direction, provides insight into the relative ‘spread’ of the axes during motion. There was an observed significant correlation between the parameters of disc health and the standard deviation of this vector.

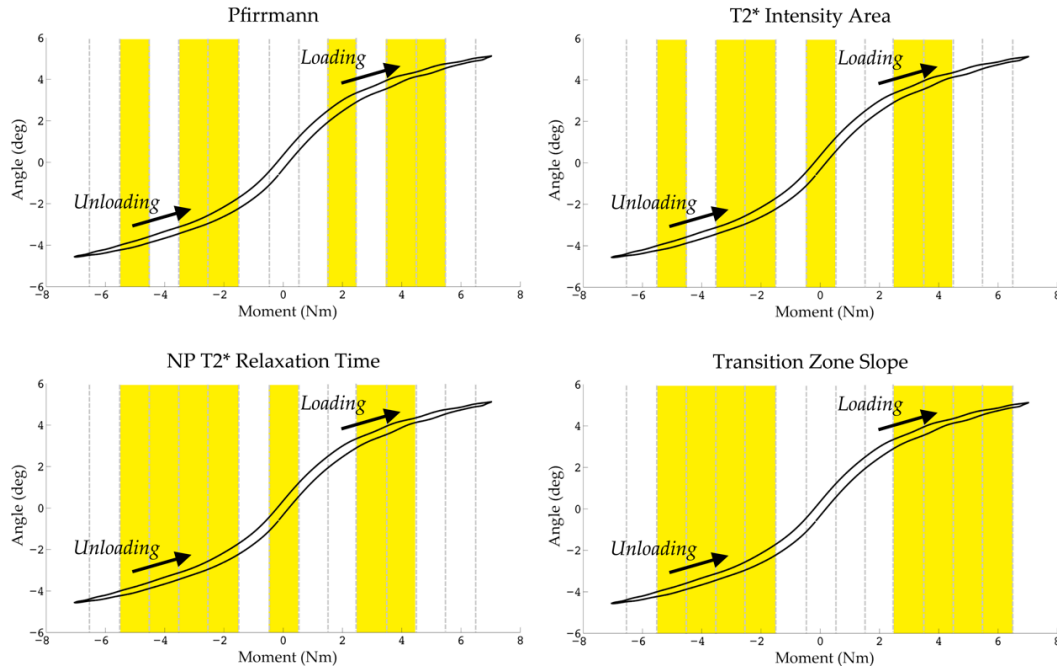


Figure 5.24. Changes in the Standard Deviation of the Primary Helical Axis Orientation (x-axis) During Lateral Bending.

A yellow bar indicates a significant correlation with disc health parameter over the corresponding 1 Nm window ($p < 0.05$). All correlations revealed a larger spread of the helical axis orientation with worsening degeneration.

Both the mean and standard deviation of the instantaneous axis of rotation in the lateral direction was affected by disc health, displayed in Figure 5.25 and Figure 5.26, respectively. With increased signs of degeneration, the IAR shifted further laterally, away from the origin of the intervertebral disc, and the relative spread of the points was greater in more degenerative discs.

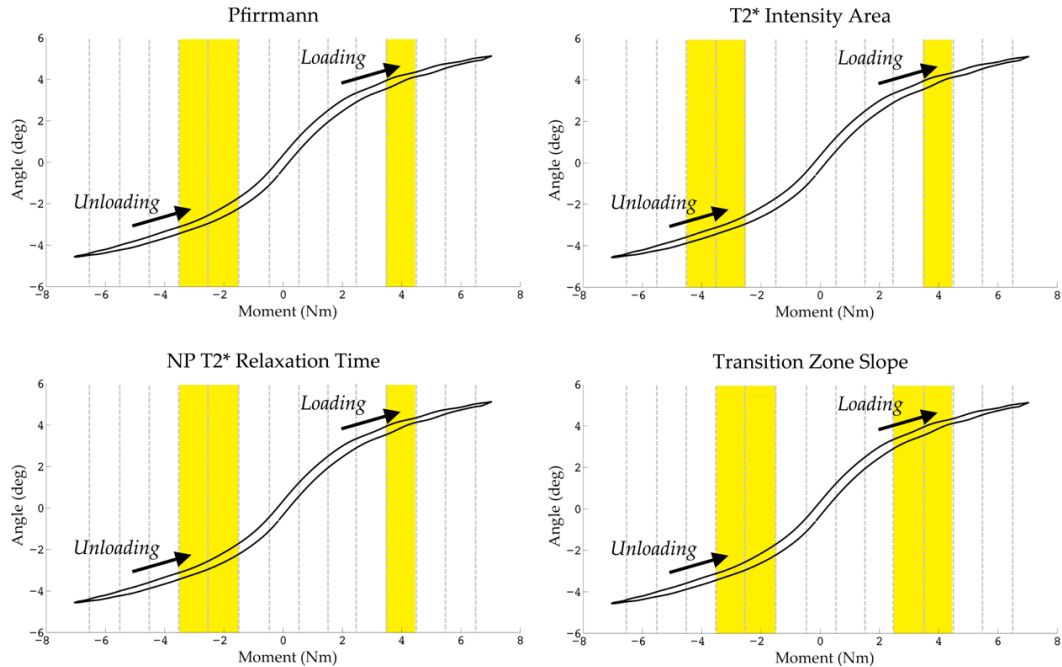


Figure 5.25. IAR Location (lateral) During Lateral Bending.
 A yellow bar indicates a significant correlation with disc health parameter over the corresponding 1 Nm window ($p < 0.05$). All correlations revealed a larger migration of the IAR with worsening degeneration.

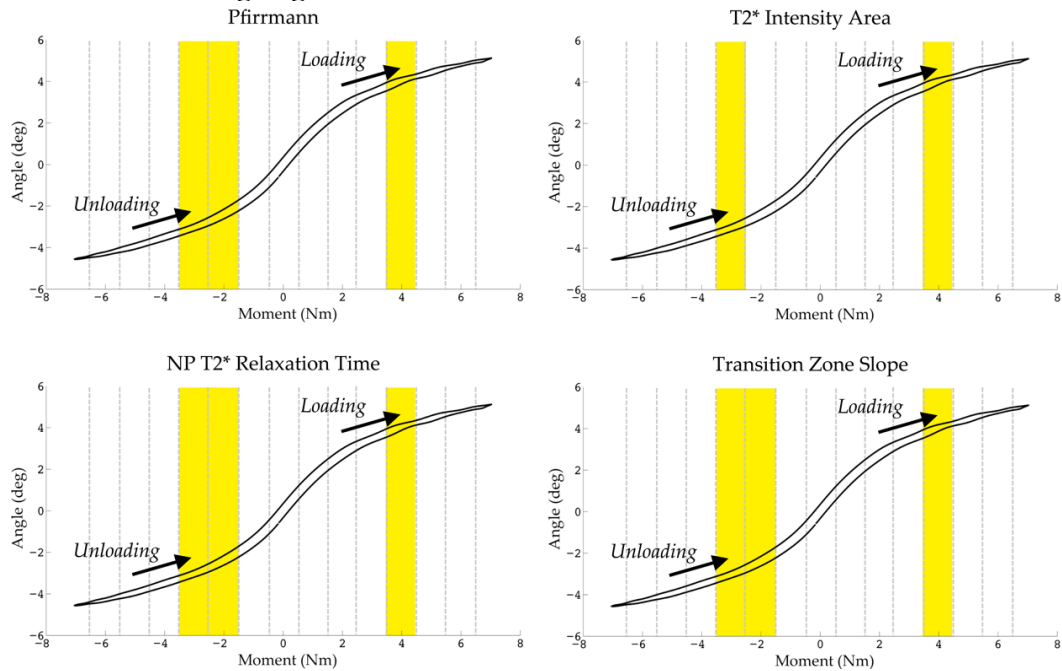


Figure 5.26. Standard Deviation of the IAR Location (lateral) During Lateral Bending.
 A yellow bar indicates a significant correlation with disc health parameter over the corresponding 1 Nm window ($p < 0.05$). All correlations revealed a larger spread of the IAR with worsening degeneration.

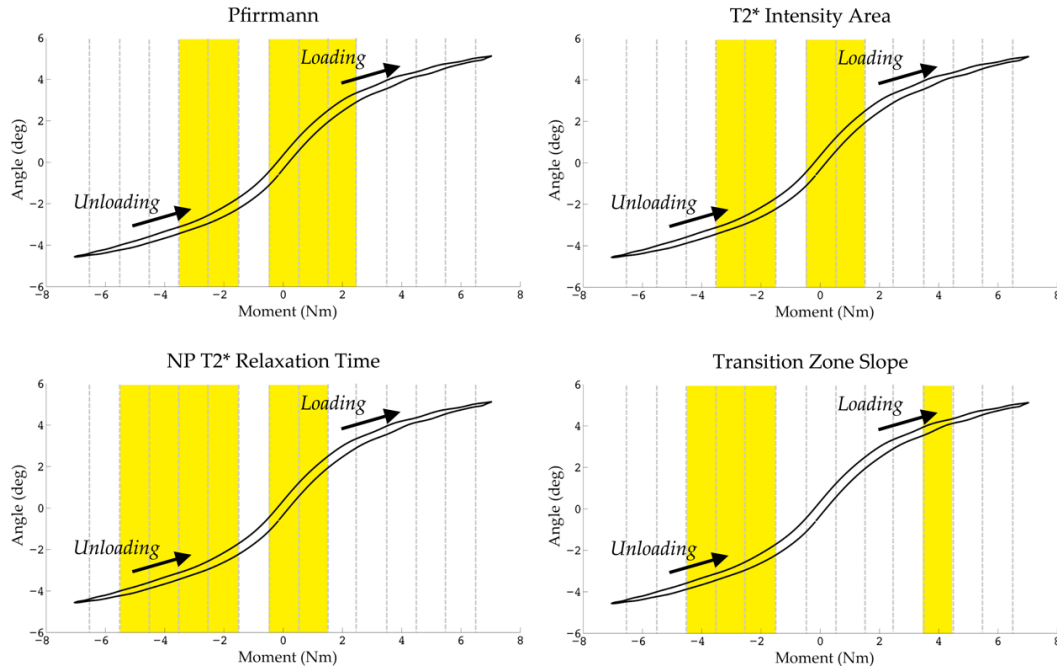


Figure 5.27. Changes in the Standard Deviation of the Instantaneous Axis of Rotation Location (superior direction) During Lateral Bending.

A yellow bar indicates a significant correlation with disc health parameter over the corresponding 1 Nm window ($p < 0.05$). All correlations revealed a larger spread of the IAR with worsening degeneration.

Although there was no change in the position of the IAR in the superior-inferior direction, there was a significant correlation regarding the standard deviation of the position (Figure 5.27). This indicates that the IAR migrates during bending more for degenerative discs, but the average location remains the same.

Regarding the area and volume of the vector space, there were no significant correlations found using the step-wise analysis over 1 Nm bins. When the entire vector space from 0 to 4 Nm is considered, there is a significant correlation between the minimally enclosed elliptical area of the IAR and the Transition Zone Slope ($r = -0.408$, $p = 0.046$) and T2* Intensity Area ($r = -0.417$, $p = 0.042$). The volume of the entire vector space was found to be significantly correlated to the Transition Zone Slope ($r = -0.417$, $p = 0.043$), T2*

Intensity Area ($r = -0.444$, $p = 0.032$), and the NP T2* Relaxation Time ($r = -0.408$, $p = 0.046$).

5.7 FUNCTIONAL MECHANICS CHANGES WITH LOCAL PROPERTIES

The nucleus pulposus exhibits the earliest and greatest changes in biochemical content and mechanical function; therefore this will be the focus of the subsequent changes associated with the functional mechanics. The inner annulus fibrosus will also be investigated.

The functional mechanics of the L4-L5 functional spinal unit were correlated with the local biochemical content and local biomechanical properties; the water content of the NP was found to be negatively correlated with both flexion stiffness ($r = -0.493$, $p = 0.037$) and flexion NZR ($r = -0.472$, $p = 0.048$). The s-GAG content was also correlated with flexion stiffness ($r = -0.470$, $p = 0.049$) as well as flexion ROM ($r = -0.590$, $p = 0.010$). S-GAG content of the NP and the iAF were significantly correlated with LB stiffness ($r = -0.548$, $p = 0.019$; $r = -0.476$, $p = 0.046$). LB NZR was significantly correlated with iAF s-GAG content ($r = -0.516$, $p = 0.028$; $r = -0.483$, $p = 0.042$). Table 5.13 and Table 5.14 display the correlation coefficients of these relationships.

Table 5.13. Correlations between T2* Parameters and Range of motion and Neutral Zone Ratio

(r: Pearson's correlation coefficient; p: p-value * represents significance at p=0.05).

			s-GAG		Water		Residual Stress		Excised Strain	
			NP	iAF	NP	iAF	NP	iAF	NP	iAF
Flexion	% FE ROM	r	0.590	0.267	0.415	-0.087	0.358	0.295	0.175	0.337
		p	0.010*	0.284	0.087	0.731	0.144	0.235	0.487	0.172
NZR	r	r	-0.262	-0.249	-0.472	0.169	-0.187	-0.023	-0.113	-0.156
		p	0.294	0.319	0.048*	0.503	0.457	0.929	0.656	0.538
Lateral Bending	ROM	r	0.239	0.066	0.333	0.110	0.067	-0.107	0.114	0.034
		p	0.341	0.795	0.178	0.663	0.792	0.673	0.568	0.894
NZR	r	r	-0.353	-0.516	-0.167	-0.224	-0.419	-0.249	-0.297	-0.164
		p	0.151	0.028*	0.507	0.371	0.084	0.320	0.232	0.516
Axial Rotation	ROM	r	-0.257	-0.433	0.194	0.026	-0.359	-0.262	-0.406	0.010
		p	0.304	0.072	0.441	0.918	0.143	0.294	0.094	0.969
NZR	r	r	-0.208	-0.131	-0.177	0.213	-0.103	-0.433	0.104	-0.202
		p	0.408	0.605	0.482	0.396	0.686	0.073	0.681	0.421

Table 5.14. Correlations between T2* Parameters and Bending Stiffness

(r: Pearson's correlation coefficient; p: p-value * represents significance at p=0.05)

			s-GAG		Water		Residual Stress		Excised Strain	
			NP	iAF	NP	iAF	NP	iAF	NP	iAF
Flex	r	r	-0.470	-0.264	-0.493	-0.162	-0.306	-0.100	-0.277	-0.246
		p	0.049*	0.291	0.037*	0.520	0.216	0.694	0.266	0.325
Ext.	r	r	-0.111	-0.073	-0.279	-0.224	0.045	0.194	-0.145	-0.242
		p	0.662	0.774	0.262	0.372	0.860	0.442	0.567	0.334
LB	r	r	-0.548	-0.476	-0.465	-0.191	-0.355	0.022	-0.390	-0.030
		p	0.019*	0.046*	0.052	0.447	0.174	0.931	0.109	0.907
AR	r	r	0.216	0.298	-0.049	0.171	0.148	0.066	0.308	0.157
		p	0.388	0.230	0.846	0.497	0.557	0.793	0.214	0.533

The helical axis patterns during lateral bending are also significantly correlated to the local biochemical content and biomechanical properties of the intervertebral disc. The

primary helical axis vector component (x-axis) is positively correlated to the residual stress, excised strain, s-GAG, and water content at the end ranges of motion (Figure 5.28). The out-of-plane vector orientation, z-axis (axial rotation) and y-axis (flexion), was negatively correlated to the residual stress, excised strain, and s-GAG content, but not water content, shown in Figure 5.29 and Figure 5.30, respectively.

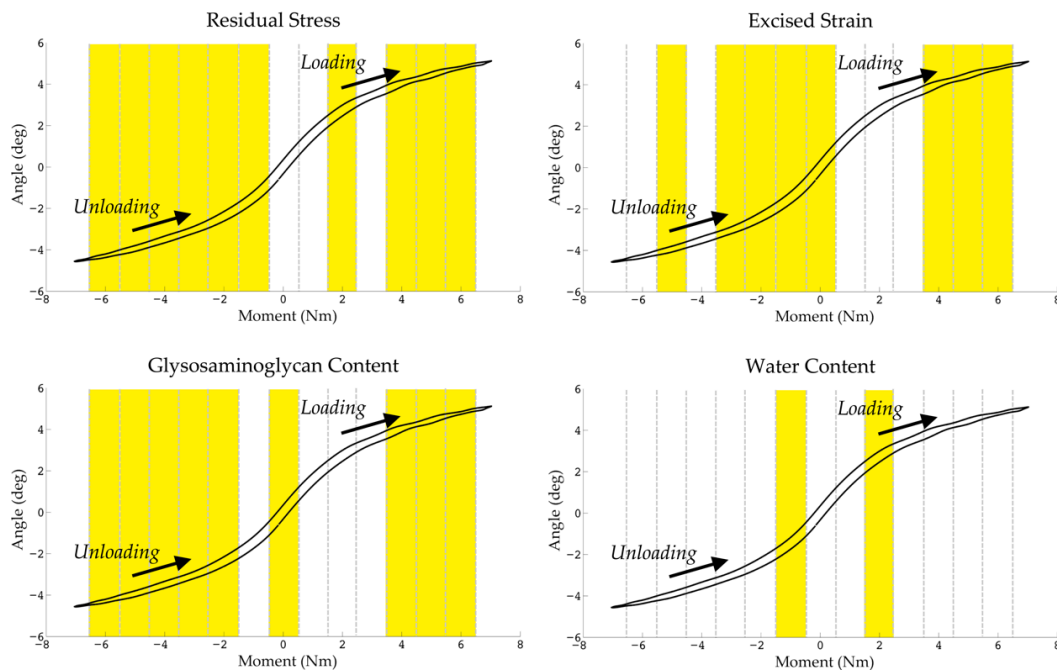


Figure 5.28. Changes in the Primary Helical Axis Orientation (x-axis) During Lateral Bending.

A yellow bar indicates a significant positive correlation with NP parameter listed above each subplot over the corresponding 1 Nm window ($p < 0.05$).

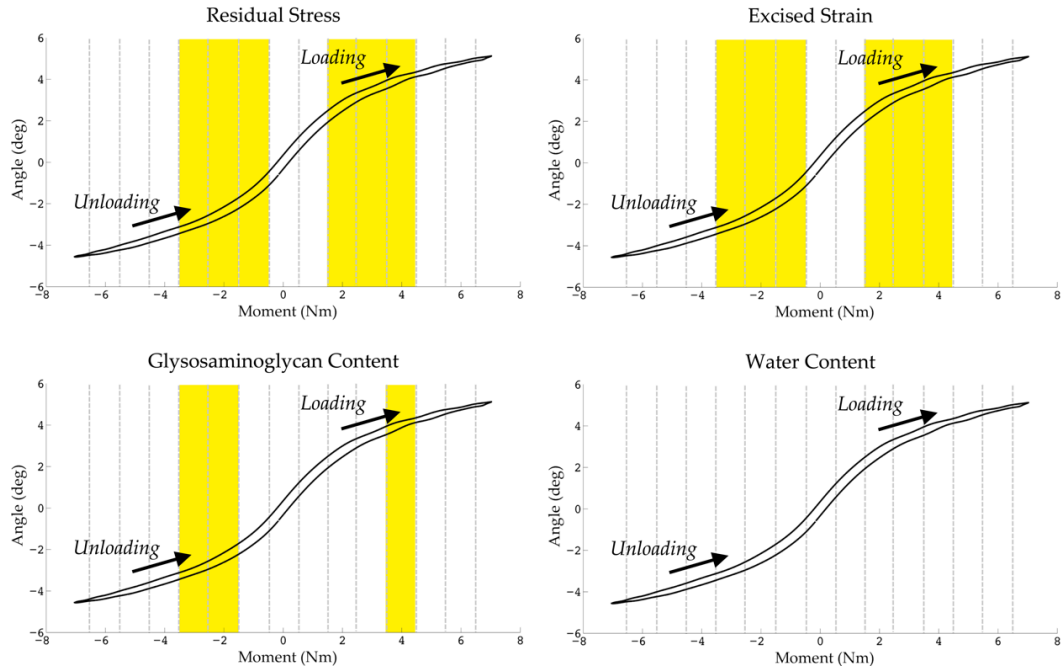


Figure 5.29. Changes in the Helical Axis Orientation (z-axis) During Lateral Bending. A yellow bar indicates a significant negative correlation with NP parameter listed above each subplot over the corresponding 1 Nm window ($p < 0.05$). This suggests an increased axial rotation component in the rotation during at the areas shaded in yellow.

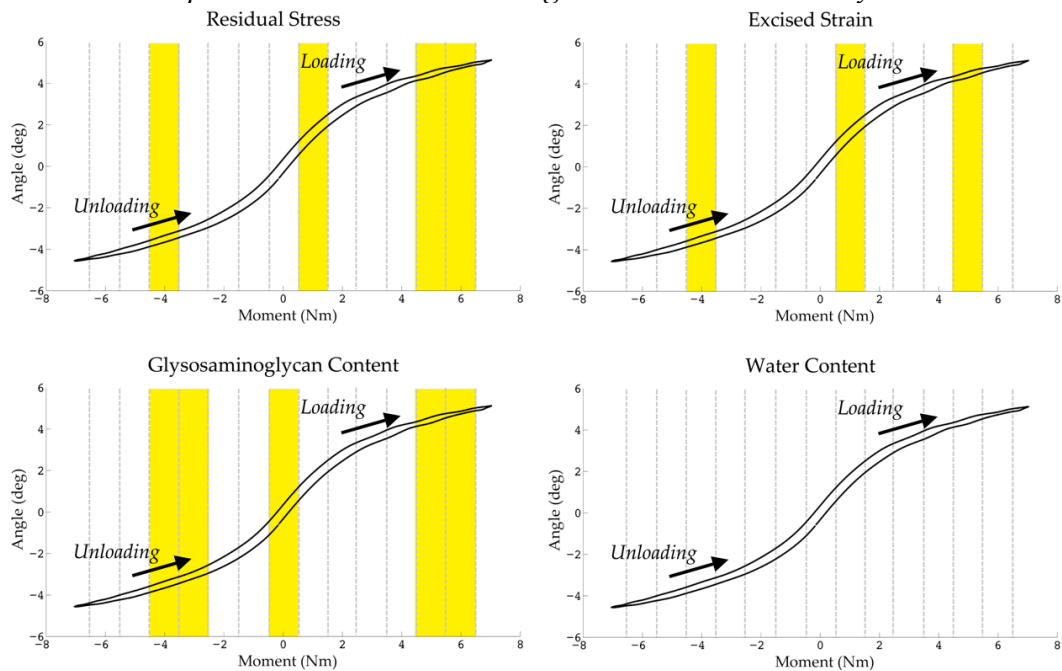


Figure 5.30. Changes in the Helical Axis Orientation (y-axis) During Lateral Bending. A yellow bar indicates a significant negative correlation with NP parameter listed above each subplot over the corresponding 1 Nm window ($p < 0.05$). This suggests an increased flexion component in the rotation during at the areas shaded in yellow.

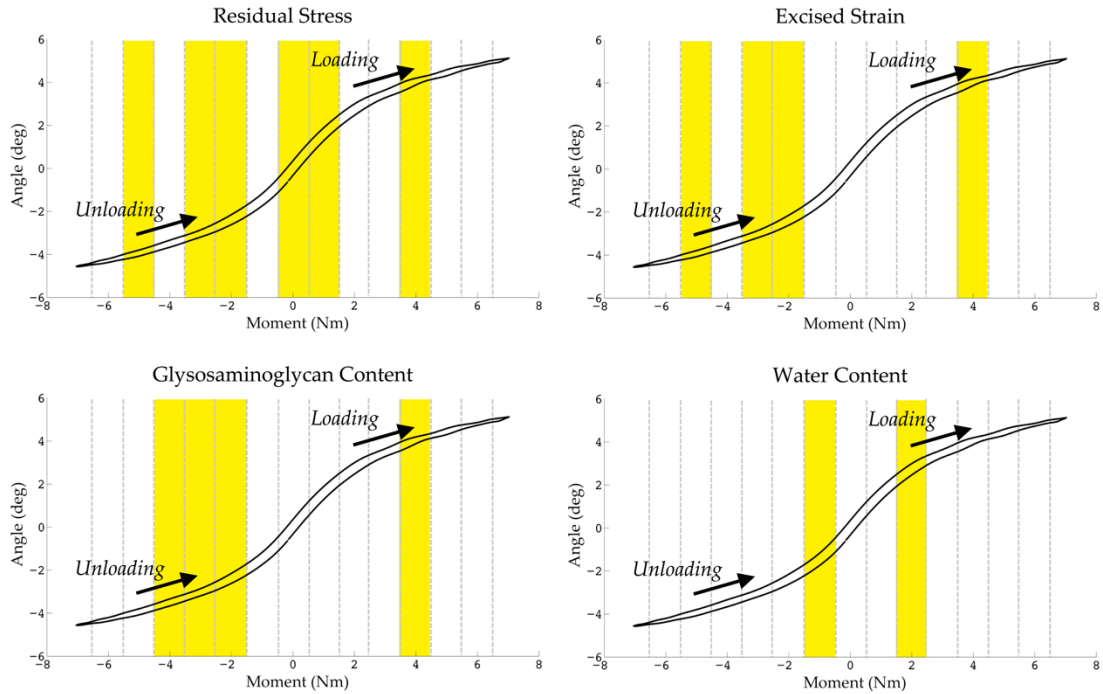


Figure 5.31. Changes in the Instantaneous Axis of Rotation Location (lateral direction) During Lateral Bending.
A yellow bar indicates a significant negative correlation with NP parameter listed above each subplot over the corresponding 1 Nm window ($p < 0.05$).

There were no significant changes in any of the parameters describing the helical axis patterns for flexion or extension. There were significant alterations in the orientation and location of the helical axes for lateral bending correlated with the presence of degeneration, assessed by MRI, biochemistry, and compressive biomechanics of the nucleus pulposus.

6 CHAPTER 6: DISCUSSION

Employing a cadaveric lumbar spine model, this experimental research aimed to define the relationships between (i) disc health, assessed by MR imaging, (ii) local biochemical content, and (iii) compressive biomechanics, and global mechanics of the lumbar spinal segment. Prior studies have investigated portions of this topic singularly, giving rise to the hypotheses and work herein. Unfortunately, a multifactor evaluation of the same tissues over a broad spectrum of disc health has yet to reveal these complex relationships with an approach sensitive to their clinical utility. Specifically, while T2* has been shown to correlate with Pfirrmann grade, there is no documented research investigating how the T2* relaxation times correspond to local biochemistry or biomechanical properties^{46,56}. The relationship between MRI signal and the effects of degeneration from a spatial distribution perspective is not well understood; most previous work just focused on the nucleus pulposus. Previous research has also reported the effects of degeneration on the functional mechanics of the spine; however, these studies measured only ROM, NZ, and stiffness as it relates to the morphological presence of disc degeneration. The analysis of global kinematics also pushes the state of literature further by the addition of instantaneous helical axis patterns and the alterations that occur during changes of disc health. The present research incorporates a new imaging sequence and disc health quantification analysis techniques, as well as includes regional biochemical and biomechanical properties to understand the multi-faceted phenomenon of disc degeneration.

The following section discusses the results of the hypotheses tested in this research program. This examination of the tested hypotheses will identify if each of the null

hypotheses was rejected. After detailing the outcomes of each hypothesis the subsequent sections will contextualize these results with the current state of the literature and demonstrate their potential clinical utility. The limitations of the present research will then be discussed in detail, followed by specific conclusions that can be drawn based on this work.

6.1 EXAMINATION OF TESTED HYPOTHESES

In this section, the original hypothesis will be stated with the results of the testing of the null hypothesis beneath. Due to the multiple part nature of these hypotheses, each part will be individually treated and reported upon such that within a hypothesis, for some parameters the null hypothesis may be rejected and others it may be not rejected. This individual treatment should provide a broader, more complete scientific picture of the intervertebral disc throughout degeneration.

***Hypothesis 1:** Pfirrmann Grade is negatively correlated with the following quantitative T2* MR imaging parameters: a) the NP T2* relaxation time, b) transition zone slope between the NP and AF, and c) T2* signal intensity area of the coronal plane.*

A significant negative correlation was observed between Pfirrmann grade and all T2* MR imaging parameters (NP T2* relaxation time, transition zone slope, and T2* signal intensity area; therefore, the null hypothesis was rejected (**1a, 1b, 1c**).

As Pfirrmann grade increased, representing more degeneration, the T2* relaxation time in the NP, and the entire coronal plane increased. The transition zone slope between the NP and AF also increased, indicating a clearer distinction between the NP and AF.

Rejection of these null hypotheses suggests that the quantitative T2* imaging parameters are sufficient in detecting the morphological changes associated with disc degeneration, as compared with the current gold standard. These T2* imaging parameters may be found to be more accurate due to their elimination of subjectivity as compared to current grading schemes. The next hypothesis builds on the results of *Hypothesis 1* and the understanding that T2* images the water mobility within the macromolecular network.

Hypothesis 2: *The T2* relaxation time is correlated with the following site-specific biochemical properties: A) Glycosaminoglycan Content (positively), B) Hydroxyproline Content (negatively), and C) water content (positively), at the following regions: a) NP, b) inner lateral AF, c) outer lateral AF, d) anterior AF, and e) posterior AF.*

The local T2* relaxation time in all regions (NP, iAF, oAF, aAF, and pAF) was found to be significantly positively correlated with the sulfated-glycosaminoglycan content (% dry weight) and the null hypothesis was rejected (**2A.a-e**). The longer the T2* relaxation time is, the higher the s-GAG content of the intervertebral disc.

No correlation between the T2* relaxation time and the hydroxyproline content (% total protein) was obtained in the NP, iAF, or pAF and the null hypothesis was not rejected (**2B.a,b,e**) for these regions. The null hypothesis was rejected (**2B.c,d**) regarding the oAF and aAF, where there was a significant correlation found.

The null hypothesis that there is a significant correlation between T2* relaxation time and the water content was rejected (**2C.e**) in the pAF region and not rejected for all other regions (**2C.a-d**).

Since T2* relaxation times are shown to be correlated to the biochemistry of the IVD, *Hypothesis 3* is based on the understanding that the biochemical constituents form the structural basis, which directly affect the biomechanical response.

Hypothesis 3: *The T2* relaxation time is positively correlated with the following local compressive mechanical properties: A) residual stress and B) excised strain at the following regions: a) NP, b) inner lateral AF, c) outer lateral AF, d) anterior AF, and e) posterior AF.*

The T2* relaxation time was significantly correlated with the residual stress and excised strain in the NP, iAF, and oAF; wherein a larger stress and strain was observed with a longer T2* relaxation time and the null hypothesis was rejected (**3A.a-c, 3B.a-c**). There was a significant correlation between the residual stress and T2* relaxation time in the pAF as well and therefore the null hypothesis was rejected (**3A.e**). The null hypothesis was not rejected in the other locations (**3A.d** and **3A.d,e**).

The intervertebral disc is the primary motion granting tissue of the functional spinal unit and since T2* relaxation times have been shown to be related to both the local biochemical and biomechanical properties of the IVD, the following *Hypotheses 4-6* have been developed to see if quantitative T2* MR imaging is sensitive in detecting changes in the tradition functional mechanics of the lumbar spine (range of motion, neutral zone ratio, and bending stiffness).

Hypothesis 4: *The range of motion in A) flexion, B) extension, and C) lateral bending is positively correlated with, and D) axial rotation is negatively correlated with T2* MR*

imaging parameters of disc health, including: a) NP T2 relaxation time, b) transition zone slope between the NP and AF, and c) T2* signal intensity area of the coronal plane.*

The null hypothesis that there is no correlation between flexion range of motion and the imaging parameters was rejected (**4A.a-c**). There was a significant positive correlation between the full flexion ROM and NP T2* relaxation time, transition zone slope, and the T2* signal intensity. When degeneration worsens and the relaxation times decrease, the ROM decreases as well. However, with regards to extension and ROM, there was no correlation, and the null hypothesis was not rejected (**4B.a-c** and **4D.a-c**). Lateral bending ROM was not correlated to the NP T2* relaxation time or the transition zone slope; these null hypotheses are not rejected (**4C.a,b**), but the ROM was correlated to T2* signal intensity area, and therefore this null hypothesis was rejected (**4C.c**).

Hypothesis 5: *The neutral zone to range of motion ratio in A) flexion, B) extension, C) lateral bending and D) axial rotation is negatively correlated with T2* MR imaging parameters of disc health, including: a) NP T2* relaxation time, b) transition zone slope between the NP and AF, and c) T2* signal intensity area of the coronal plane.*

The neutral zone to range of motion ratio of flexion and lateral bending was found to be significant and negatively correlated to all T2* MR imaging parameters of disc health. An increase in NZR was measured with decreasing relaxation times and slopes; the null hypothesis was rejected for these cases (**5A.a-c** and **5C.a-c**). The null hypothesis was not rejected for extension (**5B.a-c**) and axial rotation (**5D.a-c**), where there was no significant correlation determined.

Hypothesis 6: *The bending stiffness in A) flexion, B) extension, and C) lateral bending is negatively correlated with, and D) axial rotation positively correlated with T2* MR imaging parameters of disc health, including: a) NP T2* relaxation time, b) transition zone slope between the NP and AF, and c) T2* signal intensity area of the coronal plane.*

The bending stiffness of flexion and lateral bending both decreased significantly with increased T2* MR imaging parameters and the null hypotheses were rejected (**6A.a-c** and **6C.a-c**). Extension stiffness did not change with T2* relaxation times; the null hypothesis was not rejected (**6B.a-c**). Axial rotation stiffness increased significantly with increasing transition zone slope (**6D.b**: rejected), but no correlation was found with the NP T2* relaxation time or the signal intensity area (**6D.a,c**: not rejected).

These classical biomechanical measures of the spine are scalar metrics that reveal end range of motion, but fail to provide information regarding the pathway of motion between these points. Therefore, the investigation of the instantaneous helical axes and the alterations that result from changing disc properties provides new information to the current body of knowledge. Thus, *Hypotheses 7-10* will compare these instantaneous helical axes outcomes to reveal their potential in describing the changes that occur with intervertebral disc degeneration.

Hypothesis 7: *The average primary orientation of the helical axis vector in A) flexion, B) extension, and C) lateral bending is positively correlated with T2* MR imaging parameters of disc health, including: a) NP T2* relaxation time, b) transition zone slope between the NP and AF, and c) T2* signal intensity area of the coronal plane.*

The primary orientation of the helical axis for flexion and extension exhibited no significant correlations with any of the T2* MR imaging parameters and each of the null hypotheses were not rejected (**7A.a-c** and **7B.a-c**). The lateral bending helical axis orientation was significantly correlated with each of the imaging parameters, where the vectors were oriented with an increasing out-of-plane rotation as the disc samples became more degenerative. Therefore, the null hypothesis was rejected (**7C.a-c**).

***Hypothesis 8:** The standard deviation of the primary orientation of the helical axis vector in A) flexion, B) extension, and C) lateral bending is negatively correlated with T2* MR imaging parameters of disc health, including: a) NP T2* relaxation time, b) transition zone slope between the NP and AF, and c) T2* signal intensity area of the coronal plane.*

The standard deviation of the primary orientation of the helical axis for flexion and extension exhibited no significant correlations with any of the T2* MR imaging parameters and each of the null hypotheses were not rejected (**8A.a-c** and **8B.a-c**). The lateral bending helical axis standard deviation of the orientation was significantly correlated with each of the imaging parameters, where the vectors displayed a larger variation with more degenerative specimens. Therefore, the null hypothesis was rejected (**8C.a-c**).

***Hypothesis 9:** The average distance of the instantaneous axis of rotation from the origin in A) flexion, B) extension, and C) lateral bending is negatively correlated with T2* MR imaging parameters of disc health, including: a) NP T2* relaxation time, b) transition zone slope between the NP and AF, and c) T2* signal intensity area of the coronal plane.*

The average distance of the IAR for flexion and extension exhibited no significant correlations with any of the T2* MR imaging parameters and each of the null hypotheses was not rejected (**9A.a-c** and **9B.a-c**). The lateral bending IAR location was significantly correlated with each of the imaging parameters, where the positions deviated from the origin to a larger extent with more degenerative specimens. Therefore, the null hypothesis was rejected (**9C.a-c**).

***Hypothesis 10:** The standard deviation of the distance of the instantaneous axis of rotation from the origin in A) flexion, B) extension, and C) lateral bending are negatively correlated with T2* MR imaging parameters of disc health, including: a) NP T2* relaxation time, b) transition zone slope between the NP and AF, and c) T2* signal intensity area of the coronal plane.*

The standard deviation of the location of the IAR for flexion and extension exhibited no significant correlations with any of the T2* MR imaging parameters and each of the null hypotheses was not rejected (**10A.a-c** and **10B.a-c**). The lateral bending standard deviation of the IAR was significantly correlated with each of the imaging parameters, where the positions displayed a larger variation with more degenerative specimens. Therefore, the null hypothesis was rejected (**10C.a-c**).

The changes in the helical axis patterns, including the average and variation in the orientation and location, provide a more in depth analysis of the kinematic alterations that occur due to the progression of disc degeneration as assessed with T2* MR imaging parameters. These changes primarily occurred during lateral bending. Currently

unavailable in the literature is how the biochemical and biomechanical properties of the intervertebral disc affect the functional mechanics and helical axis parameters of spinal segments. *Hypotheses 11 and 12* examine these relationships.

Hypothesis 11: *The A) bending stiffness, B) range of motion, and C) neutral zone to range of motion ratio in A) flexion, B) extension, C) lateral bending, and D) axial rotation are correlated with the a) residual stress, b) excised strain, c) sulfated-glycosaminoglycan content, and d) water content in the NP.*

The flexion bending stiffness correlation with s-GAG and water content revealed a significant negative relationship and the null hypothesis was rejected (**11A.A.c,d**). The null hypothesis was not rejected for residual stress and strain (**11A.A.a,b**). The null hypothesis for flexion ROM was not rejected (**11B.A.a,b,d**) for residual stress, strain, and water content, but rejected (**11B.A.c**) for s-GAG content, where there was a significant correlation. The flexion NZR was significantly correlated with water content, and the null hypothesis was rejected (**11C.A.d**), but not rejected for residual stress, strain and s-GAG (**11C.A.a-c**). There were no significant correlations determined between extension or axial rotation stiffness, ROM, or NZR and the NP biochemistry or residual mechanics; the null hypotheses were all not rejected (**11A.B.a-d; 11B.B.a-d; 11C.B.a-d; 11A.D.a-d; 11B.D.a-d; and 11C.D.a-d**).

Lateral bending stiffness was significantly correlated to the s-GAG content of the NP, so the null hypothesis was rejected (**11A.Cc**). No other functional mechanics metrics were correlated with the NP biochemistry content or residual mechanics,

and the null hypotheses were not rejected (**11A.C.a,b,d; 11B.C.a-d; and 11C.C.a-d**)

Hypothesis 12: The A) helical axis orientation and B) instantaneous axis of rotation location in A) flexion, B) extension, and C) lateral bending are significantly correlated to the a) residual stress, b) excised strain, c) sulfated-glycosaminoglycan content, and d) water content in the NP.

The helical axis primary orientation or the IAR locations were not found to be significantly correlated to the NP biochemical content or the residual mechanics for flexion or extension. Therefore, these null hypotheses were not rejected (**11A.A.a-b; 11B.A.a-d; 11A.Ba-d; and 11B.B.a-d**).

The helical axes orientation for lateral bending was significantly correlated with the NP residual stress, excised strain, s-GAG, and water content leading to a rejection of the null hypotheses (**11A.C.a-d**). As the NP properties increase the axes shift, indicating more out of plane motion. The IAR location was also correlated to the NP residual mechanics and the s-GAG content, but not the water content. The null hypotheses (**11B.C.a-c**) were rejected, while (**11B.C.d**) was not rejected.

The sequence of these hypotheses are such that they progress from the ability of quantitative T2* to assess the standard scale of disc health, to being able to detect changes in the local biochemical and biomechanical properties, and to being correlated to the functional mechanics and helical axis patterns of the lumbar spine. Then the functional mechanics and helical axis patterns of the spinal segment were regressed by

the local biochemical and biomechanical properties of the disc throughout the degenerative spectrum to identify if a function predictor of disc degeneration may exist.

In the following sections I will contextualize these results with how they support and add to the current body of knowledge. This discussion will follow a similar succession to the order of hypotheses.

6.2 QUANTITATIVE T2* ASSESSMENT OF DISC HEALTH

Quantitative T2* MRI has been shown to be beneficial in cartilage imaging by probing the biochemical content of the tissue. Specifically, T2* relaxation times provide information about spatial macromolecule architecture and its interaction with water molecule mobility^{10, 11}. T2* has also been shown to be related to the organization of the matrix, where short relaxation times are indicative of more aligned molecules or fibers. T2* relaxation is a combination of inherent “true” T2 relaxation and additional relaxation due to magnetic inhomogeneity, on both a microscopic and macroscopic scale ($1/T2^* = 1/T2 + 1/T2'$, where T2' is the relaxation due to magnetic field inhomogeneities). While T2* is affected by bulk inhomogeneities in the magnetic field, which are typically not of interest, it is also affected by the differences in tissue composition at the microscopic level, such as the change from cartilage to bone, annulus to nucleus pulposus or susceptibility-induced changes related to para- or diamagnetic depositions within the disc⁵⁵. These principles have been extrapolated to the intervertebral disc. This study highlights the quantitative nature of the T2* imaging to distinguish features utilized in the Pfirrmann grading system.

The Pfirrmann grading results of this study show an intra-class correlation of 0.686, indicating a moderate variation of grades between the graders, which previous literature reports a similar degree of observer variability (ICC = 0.66)¹⁰⁴. The quantitative nature of T2* MRI and the unique analysis techniques remove subjectivity of the traditional grading scheme. These new methods investigate the features of the Pfirrmann grading system (gold standard), including disc signal intensity and clarity of the transition zone between the AF and NP.

Previous studies have investigated the relationship between T2* relaxation times alone and Pfirrmann grade. Welsch et al. investigated the relationship between T2* relaxation times, grouped into 5 ROI's from anterior to posterior, and Pfirrmann grades of subjects with low back pain⁴⁶. Only including grades 2-5 they found a significant correlation between Pfirrmann grade and all but the anterior most ROI. Hoppe et al. performed a similar study using 7 ROIs⁵⁶. They reported a significant correlation with Pfirrmann grade for all ROIs except for the anterior and posterior most regions. Their study did not include severely degenerated discs. The present study incorporated 54 discs from the entire degeneration spectrum, which followed a normal distribution (7 grade-1, 12 grade-2, 17 grade-3, 11 grade-4, 7 grade-5). Similarly to Welsch et al. there was a significant negative correlation between Pfirrmann grade and ROI's 2-5⁴⁶. The newly defined variables, T2* Intensity Area and Transition Zone Slope were also significantly correlated to the standard Pfirrmann grading, showing the T2* MR imaging parameters are sensitive to the morphological changes associated with disc degeneration. Therefore, the next step is to determine if the changes are not only related to the visual inspection of the tissue, but also changes in the biochemical content and the mechanical competency.

6.3 SITE-SPECIFIC CHANGES WITH DISC HEALTH

The loss of proteoglycans is an early stage of disc degeneration marker; therefore it is of critical interest to be able to estimate the proteoglycan content of the intervertebral disc noninvasively. The T2* relaxation time at all five tested locations (NP, iAF, oAF, aAF, pAF) were significantly and positively correlated with the sulfated-glycosaminoglycan content. An especially strong linear relationship was discovered in the NP ($r=0.944$; $p<0.001$) and inner AF ($r=0.782$; $p<0.001$). Interestingly, there was not a strong correlation between T2* relaxation times and the water content at individual test sites other than the oAF. Though there was weak correlation observed on the whole disc and a trend in the NP that approached significance. This implies T2* may be able to detect the proteoglycans of the disc, not just related hydration levels.

Previous studies have aimed to see the relationship between proteoglycan content of the disc and imaging parameters from various MRI techniques, such as T2 mapping, T1, and T1 ρ . Marinelli et al. did not find a significant correlation between T2 relaxation time and proteoglycan content in the nucleus pulposus ($r=0.73$; $p=0.06$) and the annulus fibrosus ($r=0.45$; $p=0.21$), however the NP did show a trend approaching significance³⁷.

Weidenbaum et al. also reported a lack of significant correlation between 1/T2 and proteoglycan content³⁸. Each of these studies did report a significant correlation between T2 and water content^{37,38}. Terrti et al. and Benneker et al. both found a significant relationship between T2 values and water and proteoglycan content^{39,40}. Johannessen et al. reported a correlation coefficient of $r=0.67$ ($p<0.01$) between T1 ρ values and s-GAG per dry weight in non-degenerative discs with a Pfirrmann grade of 3.5 or less⁴¹. They also found a significant correlation between T1 ρ and water content. Other studies have

established the relationship between T1 ρ and proteoglycans in both articular cartilage and the disc⁴²⁻⁴⁴. Nguyen et al. evaluated the functionality of T1 ρ in more degenerative discs and determine the relationship between T1 ρ values and the mechanics of the NP⁴⁵. The previous relationships with proteoglycans ($r=0.69$; $p<0.05$) and water content ($r=0.53$; $p<0.05$) were confirmed, but were not significant when corrected for the intercorrelations with the same spine. They did find a significant correlation with the swelling pressure ($r=0.59$; $p<0.05$) of the NP. Thus, the results herein are supported by much of the imaging and biochemistry literature and suggest that T2* provides a method to assess s-GAG content. Therefore, T2* may be able to distinguish early stage degenerative changes with a high degree of sensitivity.

Since it is the biochemical and biomechanical changes resulting from degeneration which are most clinically relevant and the most often reported, assessing the ability of T2* imaging to predict site-specific biomechanical changes is critical. T2* relaxation times were found to be significantly correlated with the residual stress, which was defined as the equilibrium stress when the excised endplate was repositioned to its original height, in all test locations except the anterior AF. The excised strain, defined as the change in disc height following excision of the endplate, was also found to be significantly correlated with T2* relaxation times in the NP, inner AF, and outer AF. In particular, the NP displayed a very strong correlation with residual stress ($r=0.857$; $p<0.001$) and excised strain ($r=0.816$; $p<0.001$), indicating T2* mapping's ability to detect changes in the mechanical behavior of the disc. Since these are both new outcome measures, there are not data in the literature to contextualize these results, but the next paragraph will examine the other measurements, which support the general findings.

The discs' excised strain ranged from no change to a 30% increase in height following release of the endplate, while the residual stress ranged from 0 to 0.20 MPa throughout the degenerative spectrum. Wilke et al. obtained *in vivo* L4-5 NP disc pressures from a healthy male exhibiting no signs of degeneration in various postures¹⁰⁵. Lying in a prone position the pressure measured was 0.1MPa and while standing was 0.5MPa. Andersson et al. performed a similar study years before and determined the average of four subject's disc pressure while standing was 0.331MPa¹⁰⁶. Although the previous *in vivo* studies have a small sample size, it can be seen that the values obtained in the present study are well within range of pressures experienced *in vivo*, as well as reported for pressures *in vitro*^{20,45,105,106}.

The viscoelastic response displayed during the stress-relaxation test was also altered by degeneration of the disc. Specifically, the middle time constant (τ_M), the logarithmic average of the short and long time constants, significantly increased with decreased T2* relaxation times in the NP and the iAF. This increases the percent relaxation rate of degenerative discs, whereas healthier tissues resist the load decay better²⁰.

The inclusion of discs from the entire degenerative spectrum allows for the evaluation of the T2* technique spanning its complete clinical range. This sequence seems to be sensitive in detecting the early changes in the NP, which is reflected by the large differences in relaxation times at the 'healthier' end of the spectrum. The absolute changes become less for the more degenerative tissues, while still maintaining the observed relationship. In other words, the T2* relaxation times drastically decrease early in the degeneration process, similar to the proteoglycan content, then slow down their rate of change during later stages. The strong positive correlations obtained in this study

between T2* relaxation times and s-GAG, residual stress, and excised strain highlight this techniques ability to predict the health of the disc on a biochemical and biomechanical level. T2* relaxation times may serve as a biomarker of both proteoglycan content and mechanical function in the detection of disc degeneration on a currently available technology.

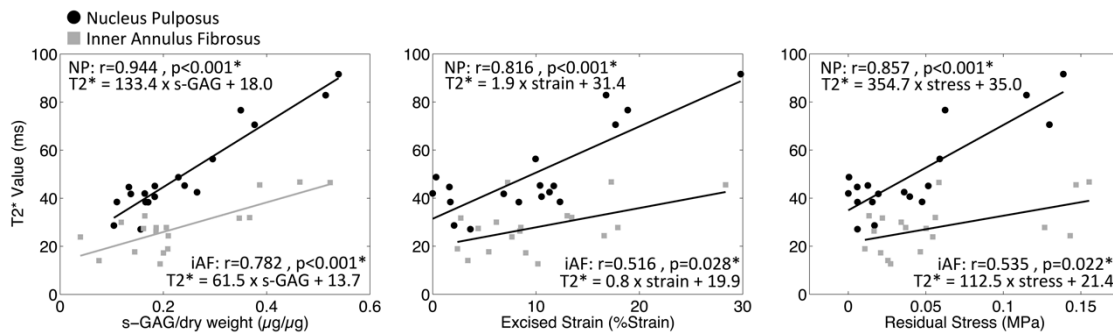


Figure 6.1. T2* Relaxation Time Correlational Plots of the Nucleus Pulposus and Inner Annulus Fibrosus.

Left- T2* vs. sulfated-glycosaminoglycan content (%dry weight). **Middle-** T2* vs. excised strain (%strain). **Right-** T2* vs. residual stress (MPa). R: Pearson's correlational coefficient and p: p-value are displayed on corresponding plot along with linear regression equation. The strength of these correlations highlights this techniques ability to predict the health of the intervertebral disc on a biochemical and biomechanical level.

Quantitative T2* assessment of disc health is sensitive in detecting the local changes associated with disc degeneration and allows for the quantification of key characteristics of disc health. These key new quantitative metrics include the T2* Intensity Area and more uniquely the Transition Zone Slope, which defines the distinction between the NP and AF. With worsening degeneration there is also a change in the distribution of both the biochemistry and the compressive mechanics of the disc. These spatial changes in conjunction with the overall depletion of the competency of the intervertebral disc provide reason to suggest there is a concurrent change in the global functional mechanics of the spinal segment.

6.4 CHANGES IN FUNCTIONAL MECHANICS WITH DISC HEALTH

Multiple parameters of functional mechanics of the spine were investigated and found to correlate with degeneration severity. The classical biomechanics outcomes are widely supported by the literature and some new measurements take our understanding of disc degeneration a step further. Disc health was correlated with the bending stiffness of the lumbar spine in flexion, but not in extension. Flexion bending stiffness increased with degeneration severity, measured by T2* MR imaging parameters, s-GAG, and water content, which resulted in a decrease of flexion ROM. Furthermore, the NZR, a relative measure of joint laxity, was shown to increase with worsening degeneration, indicating a decrease in the stability of the segment. There is more laxity in the joint until the end range of motion, where the tissue is much stiffer, allowing for little motion outside of the neutral zone. These findings were significantly correlated with the Transition Zone Slope, T2* Intensity Area, and specific ROI's, however no correlation was determined with Pfirrmann grade. Due to the role of the facets in global functional spinal mechanics it is not surprising that extension mechanics were not correlated with disc properties. It is encouraging that flexion exhibited correlations with degenerative changes, but given the posterior stabilizing structures, it is reasonable that these correlations are not extremely strong. Similarly to flexion, lateral bending stiffness was found to increase with T2* morphological signs of degeneration and s-GAG content of the NP, while ROM decreased.

The initial motion of lateral bending, near the neutral zone, the kinematics are dictated by the disc alone, however, the interactions of the facet joints play a key role in the kinematics near end ranges of motion. When the facets initiate contact an axial rotation

coupled component results due to the orientation of the facets (Figure 6.2). The degree at which the facets engage is likely a function of both the composition of the disc and its height.

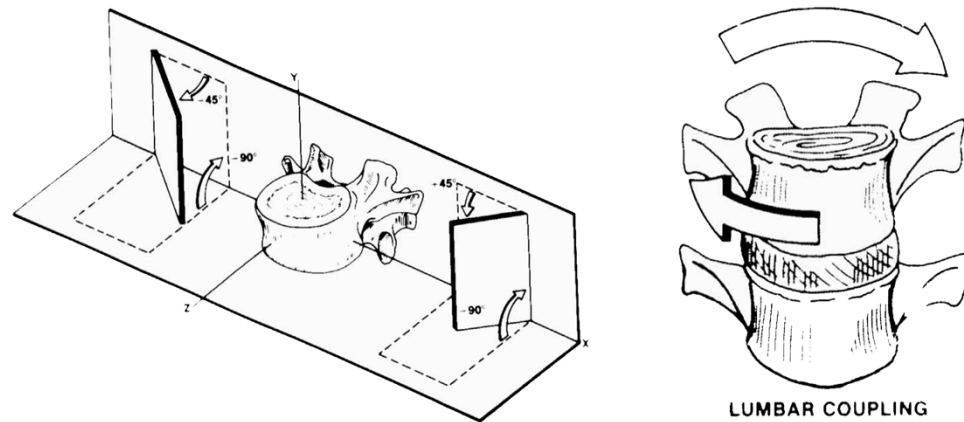


Figure 6.2. Lumbar Facet Orientation and Coupling Nature.

The lumbar facet orientation induces a coupled axial rotation component during lateral bending. Reprinted with permission⁶

Pfirrmann grade was only significantly correlated with LB NZR and stiffness, while parameters of T2* were correlated with flexion, lateral bending, and axial rotation range of motion and stiffness measurements. In support of these outcomes, previous studies have also reported a decrease in range of motion for both flexion and lateral bending, while axial rotation increased with degeneration^{71-74,107,108}. Mimura et al. reported an increase in lateral bending NZR with disc degeneration similar to the results herein⁷⁴. Other studies support the Kirkaldy-Willis and Farfan hypothesis that there are three stages to spinal instability (1) temporary dysfunction, (2) unstable phase, and (3) stabilization; where there is an increase in ROM, followed by a decrease at the very end stages of degeneration^{75,76}. Likely the formations of osteophytes and complete disc collapse at the end stages of degeneration are the primary reason for the increased

stability and fully bridged osteophytes were part of the exclusion criteria of this study. Other differences that could explain the varying results are in the evaluation of disc health, where some used MRI based methods and others used radiographic or macroscopic, dissection based, grading. The literature also suggests an increase in the bending stiffness of both lateral bending and flexion with degeneration⁷⁷. Haughton et al. observed a decrease in axial rotation bending stiffness with degeneration⁷⁸. Thus, the mechanical results of the present study align with the prevailing literature and exhibit identifiable changes across the disc degeneration spectrum.

The observed changes in global mechanics are supported by the changes locally in the AF and NP through degeneration. The mechanical properties of the AF in tension are deteriorated with degeneration, as there is a shift of collagen production from Type I to Type II^{5,9,17,60,109-111}. This results in an increase in AR ROM, while stiffness decreases¹¹². Conversely, flexion and lateral bending place the AF on the same side as bending in compression and previous literature has shown that the compressive modulus of the AF increases with degeneration^{65,66,113}, causing the bending stiffness of the functional spinal unit to increase. This phenomenon is exacerbated when the NP loses hydration due to the loss of proteoglycans, associated with degeneration. The NP no longer acts like a pressure vessel and the disc height decreases while a larger compressive load is placed on the outer AF. Although there are changes associated with stiffness, ROM, and NZR, they are only scalars, which define kinematic endpoints, and the strength of the correlations, in the present study and literature values, are relatively low. Also, the spine can move in infinite pathways of motion to reach those endpoints. In describing the health of the

spine, it may also be pertinent to describe the pathway of motion one vertebra takes with respect to another.

6.5 HELICAL AXES CHANGES WITH DISC HEALTH

The helical axis is a precise three-dimensional vector that describes how a body both rotates and translates about another body; it is a useful instrument for visualization and when the HA is computed at very small intervals, the pathway of motion can be interrogated. This provides substantially more information of the kinematical description of the spinal segment.

For the purpose of this study and to make statistical comparisons, the IHA were averaged over a 1 Nm window through the unloading and loading profiles, this technique isolates the aspect of bending where differences arise. During lateral bending, the majority of the differences in the helical axis parameters with respect to disc health occurred at the end ranges of motion, during both the unloading and loading curves. Wherein, a healthy specimen displayed helical axes orientated nearly perpendicular to the plane of pure bending through the neutral zone. Then closer to the end range of motion there is a slight shift in HA orientation representing interactions between both axial rotation, and flexion.

The IAR location also migrated slightly in the contralateral direction, but not in the superior-inferior direction. These patterns (Figure 6.3) measured and reported herein for the first time are consistent with theoretical models^{11,16,83}.

These motion patterns (Figure 6.3) are exacerbated in the more degenerative specimens, where first there is a markedly increased axial rotation component, followed by an

increased flexion component. These findings reinforce the previous discussion point that the facets orientation and their interactions govern the motion of the lumbar spine during lateral bending. Likely, this is a result of increased facet interaction with the more degenerative discs. When the facets first interact it results in coupled axial rotation, which occurred between 2 and 4 Nm. The axial rotation component was significantly greater in the degenerative discs and was followed by a greater flexion component, occurring from 4 to 6 Nm.

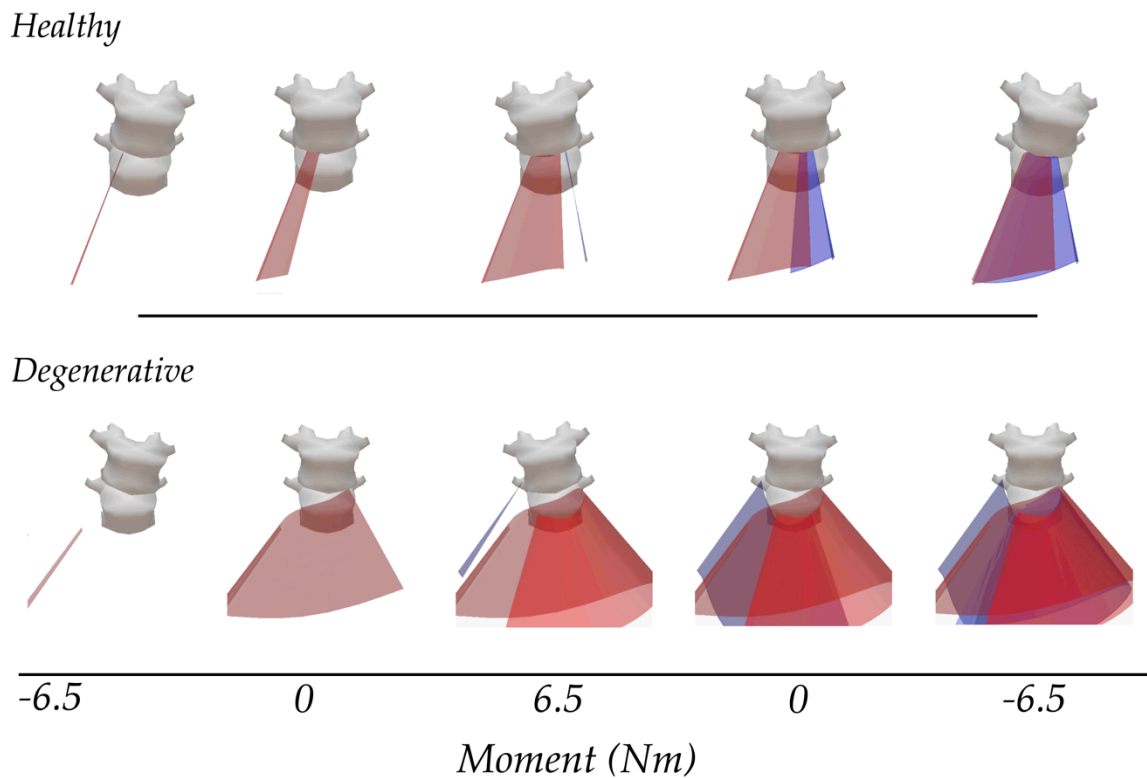


Figure 6.3. Representative Helical Axis Patterns of Healthy (top) and Degenerative (bottom) Disc during Lateral Bending.

The patterns of the healthy disc are consistent with theoretical values, where the vectors are aligned in the anterior direction near the neutral zone and slightly shift toward end ranges of motion. This highlights the coupled motion of the lumbar spine during lateral bending. These patterns are exacerbated in the degenerative specimens.

The standard deviation in the HA orientation, representing the amount of variability in the direction of the vector over the 1Nm window, increased significantly with degeneration along with the standard deviation of the IAR location. The standard deviations of each of these parameters perhaps are a measure of instability. The more sporadic and fluctuating the HA vectors are the less 'smooth' the motion, and therefore less stable. Altogether, there is increased out-of-plane bending in a particular pattern associated with degeneration along with increased variability in vector orientation and location.

These increased out-of-plane motions are postulated to be the result of decreased integrity of the IVD and in fact, the NP residual stress and strain, as well as the s-GAG content were found to be significantly correlated to the orientation and location of the HA in a similar fashion. As each of these metrics decrease, there is an increase in out-of-plane motion and migration of the HA in the lateral direction.

Although there were no significant linear correlations between any of the metrics of disc health and the helical axis patterns, there were trends observed suggesting an increased out of plane rotation and IAR migration. The healthiest intervertebral discs had more aligned helical axes and a tighter grouping of IAR than the most degenerative. However, the variability in the helical axis metrics in the moderately degenerated specimens was so great that no significance was found.

The helical axis patterns, predominantly of lateral bending, seem to be a sensitive measure related to the multi-facet parameters of disc health. The changes in lateral bending helical axis orientation and location from outside the neutral zone to the full

range of motion was correlated to the strongest predictors of disc health; including NP T2* relaxation time, transition zone slope, T2* intensity area, as well as residual stress, excised strain, and s-GAG content of the nucleus pulposus. Classically, clinicians assess functional motion primarily in the flexion-extension direction. However, it appears as though lateral bending may be a better predictor of local biochemical and biomechanical properties throughout degeneration.

6.6 DEVELOPMENT AND PARAMETERIZATION OF A PREDICTIVE MODEL

In a first attempt to explain the interactions between each of the multi-facet aspects of disc degeneration, each variable was evaluated to identify the highest predictors of altered disc health. In this way, this section will propose an initial effort in determining the parameters which should be included in a predictive model and provide a framework within which future more sophisticated predictive modeling may be accomplished. To begin with, each variable was linearly correlated to each other parameter. According to the correlation coefficient, the strongest predictors of disc health were the NP T2* Relaxation Time (ms), Transition Zone Slope (ms/mm), T2* Intensity Area (ms), NP Residual Stress (MPa), NP Excised Strain (% strain), NP s-GAG ($\mu\text{g} / \mu\text{g}$), as well as the lateral bending primary HA orientation (dimensionless- normalized to disc dimensions) and IAR location (dimensionless- normalized to disc dimensions). Table 6.1 displays each of the correlation coefficients and the corresponding p-value between each of the predominant variables related to disc degeneration. Each cell is shaded based on the strength of the correlation from darkest (above 0.8) to lightest (below 0.6).

Table 6.1. Correlation between Strong Predictors of Disc Health.
(r: Pearson's correlation coefficient; p: p-value shaded represents significance at p=0.05). Each cell is shaded based on the strength of the correlation from darkest (above 0.8) to lightest (below 0.6)

		NP T2*	Transition Zone Slope	T2* Intensity Area	s-GAG	Stress	Strain	HA	IAR
NP T2*	r	1	.833	.971	.944	.857	.816	.574	-.632
	p		<0.001	<0.001	<0.001	<0.001	<0.001	0.007	0.003
Slope	r	.833	1	.771	.732	.545	.530	.616	-.557
	p	<0.001		<0.001	0.001	0.019	0.024	0.003	0.008
Area	r	.971	.771	1	.903	.876	.822	.603	-.644
	p	<0.001	<0.001		<0.001	<0.001	<0.001	0.004	0.002
s-GAG	r	.944	.732	.903	1	.855	.805	.536	-.538
	p	<0.001	0.001	<0.001		<0.001	<0.001	0.011	0.011
Stress	r	.857	.545	.876	.855	1	.883	0.444	-.524
	p	<0.001	0.019	<0.001	<0.001		<0.001	0.033	0.013
Strain	r	.816	.530	.822	.805	.883	1	0.466	-.596
	p	<0.001	0.024	<0.001	<0.001	<0.001		0.026	0.005
HA	r	.574	.616	.603	.536	0.444	0.466	1	-.756
	p	0.007	0.003	0.004	0.011	0.033	0.026		<0.001
IAR	r	-.632	-.557	-.644	-.538	-.524	-.596	-.756	1
	p	0.003	0.008	0.002	0.011	0.013	0.005	<0.001	

All of the above relationships displayed a significant correlation; note that many of these display a very strong association. For example, 89% of the variability in predicting the nucleus pulposus s-GAG content, 73% of the residual stress, and 67% of the excised strain is explained by the T2* relaxation times. These single relationships have predictive and clinical value, especially the ability to predict the proteoglycan concentration and internal stress of the disc using a non-invasive imaging technique.

Expanding on these associations, Table 6.2 displays the linear regression coefficients describing the individual relationships between each of the variables. The table is set-up

such that the left column represents ‘y’ and the top row represents ‘x’. ‘m’ is the slope and ‘b’ is the y-intercept ($y = mx + b$).

Table 6.2. Linear Regression Coefficients.

Equations ($y = mx + b$) are displayed such that the left column represents ‘y’ and the top row represents ‘x’. ‘m’ is the slope and ‘b’ is the y-intercept, e.g. $\text{strain} = 0.35(\text{NP T2}^*) - 7.66$)

		NP T2* (ms)	Transition Zone Slope (ms/mm)	T2* Intensity Area (ms)	s-GAG ($\mu\text{g}/\mu\text{g}$)	Stress (MPa)	Strain (%)	HA (unitless)	IAR (unitless)
NP T2* (ms)	m	1.00	13.16	1.77	133.42	354.67	1.92	82.89	-27.32
	b	0.00	16.60	-5.61	17.97	34.96	31.42	-17.04	69.14
Slope (ms/mm)	m	0.05	1.00	0.09	6.55	14.30	0.08	5.64	-1.52
	b	-0.10	0.00	-0.26	0.97	1.93	1.77	-2.02	3.61
Area (ms)	m	0.53	6.69	1.00	70.13	199.16	1.06	47.83	-15.28
	b	4.81	14.50	0.00	14.63	23.03	21.19	-7.21	42.18
s-GAG ($\mu\text{g}/\mu\text{g}$)	m	0.01	0.08	0.01	1.00	2.51	0.01	0.55	-0.16
	b	-0.09	0.03	-0.13	0.00	0.13	0.11	-0.20	0.36
Stress (MPa)	m	0.00	0.02	0.00	0.29	1.00	0.01	0.15	-0.05
	b	-0.06	-0.01	-0.08	-0.03	0.00	-0.01	-0.08	0.08
Strain (%)	m	0.35	3.56	0.64	48.31	155.26	1.00	28.56	-10.94
	b	-7.66	0.64	-10.34	-1.93	3.09	0.00	-13.43	17.34
HA (unitless)	m	0.00	0.07	0.01	0.52	1.27	0.01	1.00	-0.23
	b	0.61	0.64	0.57	0.68	0.75	0.74	0.00	0.97
IAR (unitless)	m	-0.01	-0.20	-0.03	-1.76	-5.02	-0.03	-2.53	1.00
	b	1.43	1.22	1.55	1.12	0.91	1.02	2.74	0.00

These variables represent the strongest way to describe the variability present in the degenerative process. Reducing or explaining the variability in the disc health metric will produce the ability to measure a few parameters and estimate the health of the disc on its progressive degeneration. As a first attempt to describe how these variables are inter-related, a multiple linear regression analysis was performed to predict the parameters of disc health which are not measurable *in vivo* non-invasively, such as the nucleus pulposus proteoglycan content, residual stress, and excised strain by using clinically

obtainable variables. The input parameters include the nucleus pulposus T2* relaxation time, transition zone slope, T2* intensity area, helical axis orientation, and instantaneous axis of rotation position. The following models are the first cut results and Table 6.3 displays each of the independent variable's coefficients (B) and their corresponding p values (p). The figures associated with the model describe the ability of the predictive model to assess the measured values of the nucleus pulposus. The data in each of the figures is fit to the line of equality and a 95% confidence interval. If the model is perfect all of the points would lie directly on the line of equality.

$$sGAG = 0.012(NP T2^*) - 0.035(Trans\ Slope) - 0.006(T2^*\ Area) + 0.201(HA) + 0.057(IAR) - 0.272$$

$$R^2=0.92; p<0.001$$

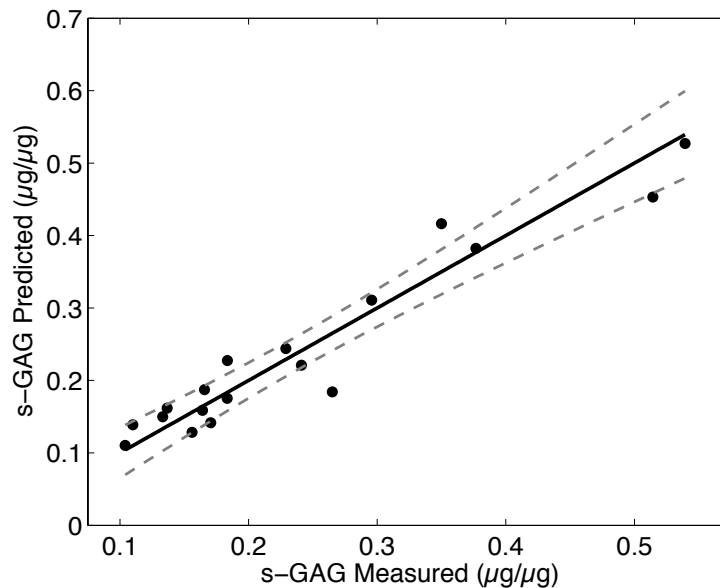


Figure 6.4. Sulfated-Glycosaminoglycan Predictive Model.

Using the sGAG equation above, this plot describes how the predictive model fits the measured variables for the sulfated-glycosaminoglycan content. The data is fit with a line of equality and a 95% confidence interval. This model explains 92% of the variability associated with the sGAG content of the nucleus pulposus.

$$\text{Residual Stress} = 0.002(\text{NP } T2^*) - 0.019(\text{Trans Slope}) - 0.002(T2^* \text{ Area}) + 0.010(\text{HA}) + 0.004(\text{IAR}) - 0.084$$

$R^2=0.84; p<0.001$

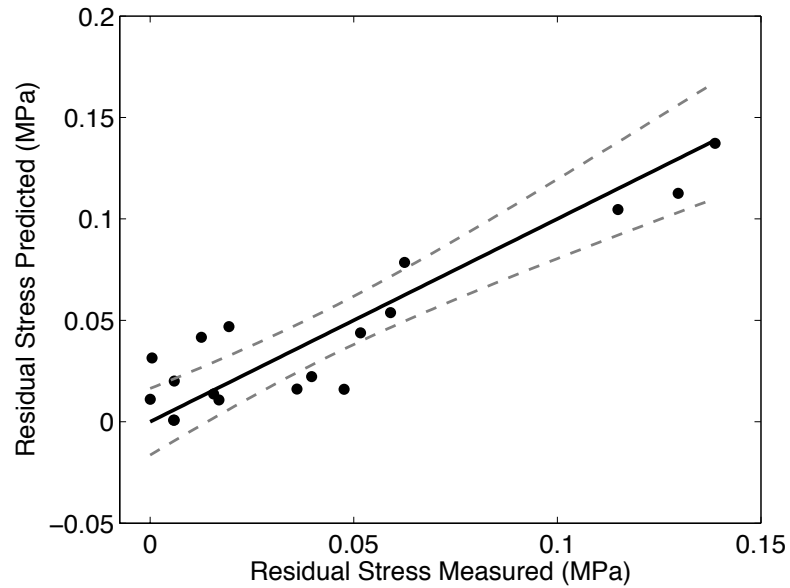


Figure 6.5. Residual Stress Predictive Model.

Using the Residual Stress equation above, this plot describes how the predictive model fits the measured variables for the residual stress of the nucleus pulposus. The data is fit with a line of equality and a 95% confidence interval. This model explains 84% of the variability of the residual stress in the nucleus pulposus.

$$\text{Excised Strain} = 0.425(\text{NP } T2^*) - 3.263(\text{Trans Slope}) + 0.100(T2^* \text{ Area}) - 0.197(\text{HA}) - 2.829(\text{IAR}) - 4.294$$

$R^2=0.75; p=0.002$

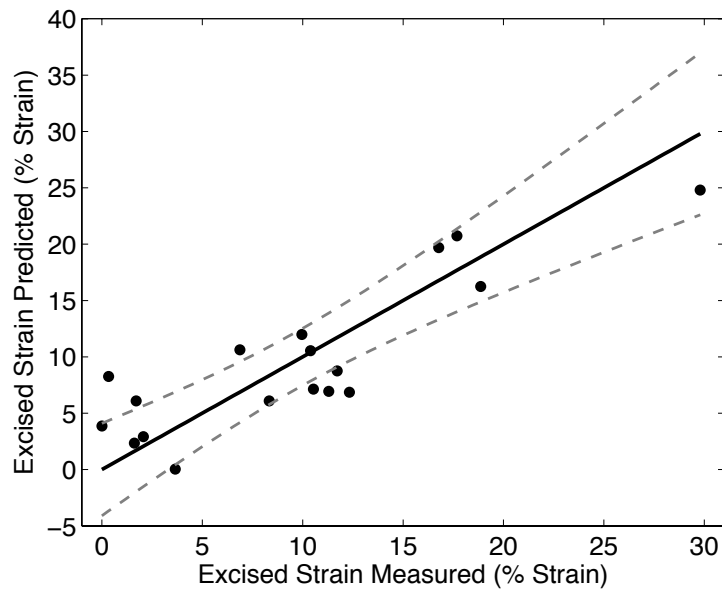


Figure 6.6. Excised Strain Predictive Model.

Using the Excised Strain equation above, this plot describes how the predictive model fits the measured variables for the excised strain of the nucleus pulposus. The data is fit with a line of equality and a 95% confidence interval. This model explains 75% of the variability of the excised strain of the nucleus pulposus.

Table 6.3. Multiple Linear Regression Model Parameters.

B: Model Coefficient; p: p-value

		NP T2* Value	Transition Zone Slope	T2* Intensity Area	HA Orientation	IAR Position	Constant
NP s-GAG	B	0.012	-0.035	-0.006	0.201	0.057	-0.272
	p	0.002	0.085	0.210	0.177	0.185	0.060
NP Residual Stress	B	0.002	-0.019	0.002	0.010	0.004	-0.084
	p	0.184	0.059	0.438	0.892	0.829	0.220
NP Excised Strain	B	0.425	-3.263	0.100	-0.197	-2.829	-4.294
	p	0.212	0.129	0.848	0.990	0.530	0.766

Each of the multiple linear regression models, as a whole, was found to be significant.

Also, the correlation coefficient was higher when using all of the metrics to predict the s-GAG content, residual stress, and excised strain than just using one independent variable.

The independent variable coefficients, other than the nucleus pulposus T2* relaxation time in the s-GAG model, were not significant. It is important to point out these are not comprehensive unique equations, but do demonstrate the multiple interactions between each of the investigated variables.

The limitations of the initial modeling strategy include the assumption and utilization of a linear relationship between the parameters. Since there is no a priori knowledge of the multifactorial relationships between these parameters, a linear function provided a preliminary effort in understanding the intricate interactions. It is likely that a more complex relationship (function) exists. Also, fitting a single equation with numerous unknown coefficients creates a non-unique solution for the model. Despite these limitations, this work identifies the parameters and lays the foundation for future modeling approaches.

Since disc health may be measured by kinematics and MRI, it appears as though the properties of T2* areal intensity, T2* transition zone slope, lumbar lateral bending helical axis orientation, and IAR should be bundled into an equation which may provide a more accurate assessment of a patient's disc. When combined linearly, these models explain 92% of the variability in predicting the nucleus pulposus s-GAG content, 84% of the residual stress, and 75% of the excised strain. Since it is not possible to directly measure the disc's biochemical content and mechanical competency non-invasively, the strength of the models provides great clinical utility for predicting the state of disc health using data that is obtainable *in vivo*.

6.7 EXPERIMENTAL LIMITATIONS

As with any cadaveric study, the limitations of this work should be considered to contextualize the clinical utility of the results. The specimens used were osteoligamentous tissues, with all of the musculature removed. The specimen underwent multiple freeze-thaw processes necessary for all aspects of the entire study; this could have affected the hydration levels of the intervertebral disc. All specimens did however receive the same treatment, so relative measures are likely only affected to a small degree. All imaging was conducted on a motionless specimen without any external soft tissue at room temperature, and therefore is an idealized imaging situation. Also, during the time of imaging the disc was not under any compressive load, which has been shown to alter the relaxation times of various quantitative imaging sequences^{114,115}.

The hybrid confined/ *in situ* indentation technique also has its limitations. Although all trabecular bone was removed from endplate, differing grades of degeneration may have differing endplate properties; however, it is unlikely that they affected our disc property measurements because the endplate has been shown to be much stiffer (>25 times) than the IVD¹¹⁶. Further, the effects of adjacent test sites on the current site, while minimized, are not completely characterized. In order to understand the dynamic response of the disc, the strain ramp rate must be increased for this protocol to more accurately capture the fast time constants. Other major limitations of this technique are the non-uniqueness of the curve fit solutions describing the viscoelastic response and the use of Equation 7, which was developed to quantify the equilibrium modulus of an indenter in an elastic half-space. The assumption of Poisson's ratio for modeling based upon literature values may not be correct. A sensitivity analysis was previously performed on this assumption, which

resulted in a maximum difference in equilibrium modulus of 9% when ν was changed from the ‘healthy’ value to the ‘severe’ values²⁰. The intrinsic error in the estimation of Poisson’s ratio is less than the variability between disc grades when calculating the equilibrium modulus.

Unfortunately, dry weights were not available for the samples used to quantify the hydroxyproline content. Therefore, they were normalized by total protein. This normalization technique is difficult to contextualize and compare to other studies, since the gold standard is to compare the hydroxyproline content against the dry weight of the tissue.

Pure moment bending tests without an axial preload were conducted on cadaveric tissue without musculature at a low loading rate commensurate with flexing fully forward over a 12 second duration. This does not replicate the *in vivo* musculature forces and forces of body weight. Although studies have shown this causes minimal effects on the intersegmental ranges of motion, there is evidence that the pressure of the IVD increases¹¹⁷. This disc loading could affect the helical axis patterns and effectively the pathway of motion, although again, all specimens were tested similarly and so relative differences are valid. Although pure moments were applied to the spine and coupled motions occurred, when analyzing the ROM and NZR only the primary direction of bending was analyzed for each rotation sequence. These coupled motions were investigated and measured using a helical axis approach. When correlating the functional spine mechanics to imaging parameters of disc health, three spinal segments (L3-S1) were all compared against each other, however there was no statistical difference as a function of disc level within a single Pfirrmann grade ($p > 0.10$).

When performing the helical axis analysis, a fifth order low pass Butterworth filter with a cutoff frequency of 0.4 Hz was used, which was similar to previously published work^{92,93}. This filter is nearly three times the input frequency, but is still very aggressive and may have removed some of the signal. However, without proper filtering, the computation of the helical axes over very short steps leads to sporadic vectors due to noise in the signal or non-smooth motion. A more thorough description of the sensitivity analysis can be seen in the Appendix. Even though care was taken to appropriately compute the HA, stray vectors still occurred, which is why the average over a pre-described window was taken to minimize these effects. However, the metrics IAR area and Vector volume space are grossly overestimated in these situations. Further analysis techniques removing outliers is necessary to avoid these errors.

All hypothesis correlational testing was performed first, and then post-hoc analyses were used to address the remaining relationships. These statistical tests assumed the parameters were independent, however it is likely that the system as a whole is all inter-related. Also, hypotheses were rejected based on the p-value of their relationship, rather than the correlation coefficient, allowing for weak to moderate correlations to be found statistically significant.

In spite of these limitations, which are susceptible to all cadaveric biomechanical studies, the samples of specimen spanning the degenerative spectrum and outcome measures represent one of the most complete data sets describing the multi-faceted phenomena of disc degeneration and its affects on global spine mechanics. Furthermore, all specimens included in this study underwent the same regiment so all internal comparisons valid.

6.8 SUMMARY

The intervertebral disc affords the spine its extensive multidirectional motion due to the complex interaction between two morphologically, biomechanically, and biochemically distinct tissues: the annulus fibrosus and the nucleus pulposus. The AF consists of highly organized concentric rings of fibrocartilaginous material surrounding the NP, which is composed of a hydrated, disorganized matrix of collagen and proteoglycans. When a load is applied to the spine, the hydrated NP acts like a pressure vessel, placing the AF in tension. This unique system allows the disc to absorb and dissipate large compressive loads applied to the spine.

Degeneration of the intervertebral disc is a progressive phenomenon that occurs in response to age, injury, pathology, or more likely a combination of these. Increased or abnormal mechanical loading leads to alterations in the discs' biochemical composition. The earliest changes occur in the nucleus pulposus, where there is an initial decrease in the proteoglycan content. These changes lead to diminished mechanical competency resulting in the discs' inability to maintain structure and function potentially causing discogenic pain or pain due to cord occlusion, neural compressive lesions, or nerve root pinching, from altered spinal stability. It is of critical interest to detect these changes early in the degeneration process in order to cease the progression with the development of new therapeutics including biologics and other treatments.

Direct measurements of the disc's biochemical and biomechanical properties are not possible *in vivo*; therefore magnetic resonance imaging is the gold standard for evaluating disc health. This research program utilized quantitative T2* MR imaging sequence to

quantify the features of the Pfirrmann scale. These included the MRI signal intensity and the distinction between the nucleus pulposus and surrounding annulus fibrosus. The T2* relaxation times and the newly defined variables, T2* Intensity Area and Transition Zone Slope were significantly correlated to the standard Pfirrmann grading, showing the T2* MR imaging parameters are sensitive to the morphological changes associated with disc degeneration. Also, the interrogation of these features using the T2* images enable the quantitative grading of disc degeneration without subjectivity or bias but with clinically recognized features of distinction. The T2* intensity area and the Transition Zone Slope significantly decrease with worsening degeneration.

Furthermore T2* relaxation times were found to have a high sensitivity for measuring the proteoglycan content of the intervertebral disc. This relationship could have a profound impact on the early detection of disc degeneration. The T2* relaxation times were also significantly correlated to the residual stress and excised strain of the disc, particularly in the nucleus pulposus and the inner annulus fibrosus. With increased degeneration severity, there is a decrease in the T2* relaxation times, a decrease in the proteoglycan content, a decrease in the residual stress, and a decrease in the excised strain of the disc.

These multi-faceted changes that occur with degeneration impact the global mechanics of the spinal unit by increasing the NZR, or joint instability, and altering the bending stiffness and range of motion. Even stronger correlations were identified for altered disc health's affects on the helical axis patterns of lateral bending. There was a marked increase of out-of-plane rotations and a larger migration of the instantaneous axis of rotation with worsening degeneration evaluated by MRI, local biochemistry, and local residual mechanics.

Quantitative T2* MRI has the sensitivity to predict the local biochemical and biomechanical properties of the intervertebral disc. This in combination with the understanding of the pathway of motion throughout the degenerative progress, using the helical axis approach, enhances the mechanistic understanding of the degenerative intervertebral disc. Each of these measurements, MRI and spinal kinematics, has the ability to be measured *in vivo*; therefore this approach has great potential for clinical utility. Together, these data may provide the foundation for a clinically relevant tool for patient assessment and disc health identification for the purposes of patient stratification for targeted treatment options.

7 BIBLIOGRAPHY

1. Andersson GB. Epidemiological features of chronic low-back pain. *Lancet*. Aug 14 1999;354(9178):581-585.
2. Wilder DG, Pope MH. Epidemiological and aetiological aspects of low back pain in vibration environments - an update. *Clin Biomech (Bristol, Avon)*. Mar 1996;11(2):61-73.
3. Leigh JP, Markowitz SB, Fahs M, Shin C, Landrigan PJ. Occupational injury and illness in the United States. Estimates of costs, morbidity, and mortality. *Arch Intern Med*. Jul 28 1997;157(14):1557-1568.
4. Gray H. *Anatomy : descriptive and surgical*. San Diego, CA: Thunder Bay; 2001.
5. Urban JP, Roberts S. Degeneration of the intervertebral disc. *Arthritis Res Ther*. 2003;5(3):120-130.
6. Panjabi MM, White AA, 3rd. Basic biomechanics of the spine. *Neurosurgery*. Jul 1980;7(1):76-93.
7. Roughley PJ, Melching LI, Heathfield TF, Pearce RH, Mort JS. The structure and degradation of aggrecan in human intervertebral disc. *Eur Spine J*. Aug 2006;15 Suppl 3:S326-332.
8. Kim PK, Branch CL, Jr. The lumbar degenerative disc: confusion, mechanics, management. *Clin Neurosurg*. 2006;53:18-25.
9. Roughley PJ. Biology of intervertebral disc aging and degeneration: involvement of the extracellular matrix. *Spine (Phila Pa 1976)*. Dec 1 2004;29(23):2691-2699.
10. Frijns AJH, Huyghe JM, Janssen JD. A validation of the quadriphasic mixture theory for intervertebral disc tissue. *International Journal of Engineering Science*. 1997;35(15):1419-1429.
11. White AA, Panjabi MM. *Clinical biomechanics of the spine*. Philadelphia: Lippincott; 1978.
12. Teyhen DS, Flynn TW, Childs JD, et al. Fluoroscopic video to identify aberrant lumbar motion. *Spine (Phila Pa 1976)*. Apr 1 2007;32(7):E220-229.
13. Alexander LA, Hancock E, Agouris I, Smith FW, MacSween A. The response of the nucleus pulposus of the lumbar intervertebral discs to functionally loaded positions. *Spine (Phila Pa 1976)*. Jun 15 2007;32(14):1508-1512.
14. Fazey PJ, Takasaki H, Singer KP. Nucleus pulposus deformation in response to lumbar spine lateral flexion: an in vivo MRI investigation. *Eur Spine J*. Jul 2010;19(7):1115-1120.
15. Panjabi MM. The stabilizing system of the spine. Part II. Neutral zone and instability hypothesis. *J Spinal Disord*. Dec 1992;5(4):390-396; discussion 397.

16. Schmidt H, Heuer F, Wilke HJ. Interaction between finite helical axes and facet joint forces under combined loading. *Spine*. Dec 1 2008;33(25):2741-2748.
17. Antoniou J, Steffen T, Nelson F, et al. The human lumbar intervertebral disc: evidence for changes in the biosynthesis and denaturation of the extracellular matrix with growth, maturation, ageing, and degeneration. *J Clin Invest*. Aug 15 1996;98(4):996-1003.
18. Pearce RH, Grimmer BJ, Adams ME. Degeneration and the chemical composition of the human lumbar intervertebral disc. *J Orthop Res*. 1987;5(2):198-205.
19. Buckwalter JA. Aging and degeneration of the human intervertebral disc. *Spine (Phila Pa 1976)*. Jun 1 1995;20(11):1307-1314.
20. Ellingson AM, Nuckley DJ. Intervertebral disc viscoelastic parameters and residual mechanics spatially quantified using a hybrid confined/in situ indentation method. *J Biomech*. Feb 2 2012;45(3):491-496.
21. Johannessen W, Elliott DM. Effects of degeneration on the biphasic material properties of human nucleus pulposus in confined compression. *Spine*. Dec 15 2005;30(24):E724-729.
22. Pfirrmann CW, Metzdorf A, Zanetti M, Hodler J, Boos N. Magnetic resonance classification of lumbar intervertebral disc degeneration. *Spine (Phila Pa 1976)*. Sep 1 2001;26(17):1873-1878.
23. Thompson JP, Pearce RH, Schechter MT, Adams ME, Tsang IK, Bishop PB. Preliminary evaluation of a scheme for grading the gross morphology of the human intervertebral disc. *Spine (Phila Pa 1976)*. May 1990;15(5):411-415.
24. Arana E, Royuela A, Kovacs FM, et al. Lumbar spine: agreement in the interpretation of 1.5-T MR images by using the Nordic Modic Consensus Group classification form. *Radiology*. Mar 2010;254(3):809-817.
25. Raininko R, Manninen H, Battie MC, Gibbons LE, Gill K, Fisher LD. Observer variability in the assessment of disc degeneration on magnetic resonance images of the lumbar and thoracic spine. *Spine (Phila Pa 1976)*. May 1 1995;20(9):1029-1035.
26. Boden SD, Davis DO, Dina TS, Patronas NJ, Wiesel SW. Abnormal magnetic-resonance scans of the lumbar spine in asymptomatic subjects. A prospective investigation. *J Bone Joint Surg Am*. Mar 1990;72(3):403-408.
27. Savage RA, Whitehouse GH, Roberts N. The relationship between the magnetic resonance imaging appearance of the lumbar spine and low back pain, age and occupation in males. *Eur Spine J*. 1997;6(2):106-114.
28. Jensen MC, Brant-Zawadzki MN, Obuchowski N, Modic MT, Malkasian D, Ross JS. Magnetic resonance imaging of the lumbar spine in people without back pain. *N Engl J Med*. Jul 14 1994;331(2):69-73.

29. Powell MC, Wilson M, Szypryt P, Symonds EM, Worthington BS. Prevalence of lumbar disc degeneration observed by magnetic resonance in symptomless women. *Lancet*. Dec 13 1986;2(8520):1366-1367.
30. Bittersohl B, Miese FR, Dekkers C, et al. T2* mapping and delayed gadolinium-enhanced magnetic resonance imaging in cartilage (dGEMRIC) of glenohumeral cartilage in asymptomatic volunteers at 3 T. *European Radiology*. 2012.
31. Krause FG, Klammer G, Benneker LM, Werlen S, Mamisch TC, Weber M. Biochemical T2* MR quantification of ankle arthrosis in pes cavovarus. *J Orthop Res*. Dec 2010;28(12):1562-1568.
32. Carballido-Gamio J, Stahl R, Blumenkrantz G, Romero A, Majumdar S, Link TM. Spatial analysis of magnetic resonance T1rho and T2 relaxation times improves classification between subjects with and without osteoarthritis. *Med Phys*. Sep 2009;36(9):4059-4067.
33. Schmitt B, Zbyn S, Stelzeneder D, et al. Cartilage quality assessment by using glycosaminoglycan chemical exchange saturation transfer and (23)Na MR imaging at 7 T. *Radiology*. Jul 2011;260(1):257-264.
34. Singh A, Haris M, Cai K, et al. Chemical exchange saturation transfer magnetic resonance imaging of human knee cartilage at 3 T and 7 T. *Magn Reson Med*. Aug 2012;68(2):588-594.
35. Buchbender C, Scherer A, Kropil P, et al. Cartilage quality in rheumatoid arthritis: comparison of T2* mapping, native T1 mapping, dGEMRIC, DeltaR1 and value of pre-contrast imaging. *Skeletal Radiol*. Jun 2012;41(6):685-692.
36. Welsch GH, Trattng S, Hughes T, et al. T2 and T2* mapping in patients after matrix-associated autologous chondrocyte transplantation: initial results on clinical use with 3.0-Tesla MRI. *Eur Radiol*. Jun 2010;20(6):1515-1523.
37. Marinelli NL, Haughton VM, Munoz A, Anderson PA. T2 relaxation times of intervertebral disc tissue correlated with water content and proteoglycan content. *Spine (Phila Pa 1976)*. Mar 1 2009;34(5):520-524.
38. Weidenbaum M, Foster RJ, Best BA, et al. Correlating magnetic resonance imaging with the biochemical content of the normal human intervertebral disc. *J Orthop Res*. Jul 1992;10(4):552-561.
39. Benneker LM, Heini PF, Anderson SE, Alini M, Ito K. Correlation of radiographic and MRI parameters to morphological and biochemical assessment of intervertebral disc degeneration. *Eur Spine J*. Feb 2005;14(1):27-35.
40. Terti M, Paajanen H, Laato M, Aho H, Komu M, Kormano M. Disc degeneration in magnetic resonance imaging. A comparative biochemical, histologic, and radiologic study in cadaver spines. *Spine (Phila Pa 1976)*. Jun 1991;16(6):629-634.

41. Johannessen W, Auerbach JD, Wheaton AJ, et al. Assessment of human disc degeneration and proteoglycan content using T1rho-weighted magnetic resonance imaging. *Spine (Phila Pa 1976)*. May 15 2006;31(11):1253-1257.
42. Auerbach JD, Johannessen W, Borthakur A, et al. In vivo quantification of human lumbar disc degeneration using T(1rho)-weighted magnetic resonance imaging. *Eur Spine J*. Aug 2006;15 Suppl 3:S338-344.
43. Blumenkrantz G, Majumdar S. Quantitative magnetic resonance imaging of articular cartilage in osteoarthritis. *Eur Cell Mater*. 2007;13:76-86.
44. Wheaton AJ, Dodge GR, Borthakur A, Kneeland JB, Schumacher HR, Reddy R. Detection of changes in articular cartilage proteoglycan by T(1rho) magnetic resonance imaging. *J Orthop Res*. Jan 2005;23(1):102-108.
45. Nguyen AM, Johannessen W, Yoder JH, et al. Noninvasive Quantification of Human Nucleus Pulposus Pressure with Use of T1 -Weighted Magnetic Resonance Imaging. *The Journal of Bone and Joint Surgery*. 2008;90(4):796-802.
46. Welsch GH, Trattnig S, Paternostro-Sluga T, et al. Parametric T2 and T2* mapping techniques to visualize intervertebral disc degeneration in patients with low back pain: initial results on the clinical use of 3.0 Tesla MRI. *Skeletal Radiol*. May 2011;40(5):543-551.
47. Mamisch TC, Hughes T, Mosher TJ, et al. T2 star relaxation times for assessment of articular cartilage at 3 T: a feasibility study. *Skeletal Radiol*. Apr 19 2011.
48. Williams A, Qian Y, Bear D, Chu CR. Assessing degeneration of human articular cartilage with ultra-short echo time (UTE) T2* mapping. *Osteoarthritis and Cartilage*. 2010;18(4):539-546.
49. Bittersohl B, Miese FR, Hosalkar HS, et al. T2 * mapping of hip joint cartilage in various histological grades of degeneration. *Osteoarthritis Cartilage*. Mar 30 2012.
50. Qian Y, Williams AA, Chu CR, Boada FE. Multicomponent T2* mapping of knee cartilage: technical feasibility ex vivo. *Magn Reson Med*. Nov 2010;64(5):1426-1431.
51. Williams A, Qian Y, Chu CR. UTE-T2 * mapping of human articular cartilage in vivo: a repeatability assessment. *Osteoarthritis Cartilage*. Jan 2011;19(1):84-88.
52. Marik W, Apprich S, Welsch GH, Mamisch TC, Trattnig S. Biochemical evaluation of articular cartilage in patients with osteochondrosis dissecans by means of quantitative T2- and T2-mapping at 3T MRI: a feasibility study. *Eur J Radiol*. May 2012;81(5):923-927.
53. Miese FR, Zilkens C, Holstein A, et al. Assessment of early cartilage degeneration after slipped capital femoral epiphysis using T2 and T2* mapping. *Acta Radiol*. Feb 1 2011;52(1):106-110.
54. Bittersohl B, Hosalkar HS, Hughes T, et al. Feasibility of T2* mapping for the evaluation of hip joint cartilage at 1.5T using a three-dimensional (3D), gradient-echo (GRE) sequence: a prospective study. *Magn Reson Med*. Oct 2009;62(4):896-901.

55. Chavhan GB, Babyn PS, Thomas B, Shroff MM, Haacke EM. Principles, techniques, and applications of T2*-based MR imaging and its special applications. *Radiographics*. Sep-Oct 2009;29(5):1433-1449.
56. Hoppe S, Quirbach S, Mamisch TC, Krause FG, Werlen S, Benneker LM. Axial T2* mapping in intervertebral discs: a new technique for assessment of intervertebral disc degeneration. *Eur Radiol*. Apr 29 2012.
57. Watanabe A, Benneker LM, Boesch C, Watanabe T, Obata T, Anderson SE. Classification of intervertebral disk degeneration with axial T2 mapping. *AJR Am J Roentgenol*. Oct 2007;189(4):936-942.
58. Roberts S, Beard HK, O'Brien JP. Biochemical changes of intervertebral discs in patients with spondylolisthesis or with tears of the posterior annulus fibrosus. *Ann Rheum Dis*. Feb 1982;41(1):78-85.
59. Lyons G, Eisenstein SM, Sweet MB. Biochemical changes in intervertebral disc degeneration. *Biochim Biophys Acta*. Apr 3 1981;673(4):443-453.
60. Hollander AP, Heathfield TF, Liu JJ, et al. Enhanced denaturation of the alpha (II) chains of type-II collagen in normal adult human intervertebral discs compared with femoral articular cartilage. *J Orthop Res*. Jan 1996;14(1):61-66.
61. Boos N, Nerlich AG, Wiest I, von der Mark K, Aebi M. Immunolocalization of type X collagen in human lumbar intervertebral discs during ageing and degeneration. *Histochem Cell Biol*. Dec 1997;108(6):471-480.
62. Best BA, Guilak F, Setton LA, et al. Compressive mechanical properties of the human annulus fibrosus and their relationship to biochemical composition. *Spine (Phila Pa 1976)*. Jan 15 1994;19(2):212-221.
63. Iatridis JC, Setton LA, Weidenbaum M, Mow VC. Alterations in the mechanical behavior of the human lumbar nucleus pulposus with degeneration and aging. *J Orthop Res*. Mar 1997;15(2):318-322.
64. Perie DS, Maclean JJ, Owen JP, Iatridis JC. Correlating material properties with tissue composition in enzymatically digested bovine annulus fibrosus and nucleus pulposus tissue. *Ann Biomed Eng*. May 2006;34(5):769-777.
65. Umehara S, Tadano S, Abumi K, Katagiri K, Kaneda K, Ukai T. Effects of degeneration on the elastic modulus distribution in the lumbar intervertebral disc. *Spine*. Apr 1 1996;21(7):811-819; discussion 820.
66. Iatridis JC, Setton LA, Foster RJ, Rawlins BA, Weidenbaum M, Mow VC. Degeneration affects the anisotropic and nonlinear behaviors of human annulus fibrosus in compression. *J Biomech*. Jun 1998;31(6):535-544.
67. Adams MA, Roughley PJ. What is intervertebral disc degeneration, and what causes it? *Spine (Phila Pa 1976)*. Aug 15 2006;31(18):2151-2161.

68. Adams MA, McNally DS, Dolan P. 'Stress' distributions inside intervertebral discs. The effects of age and degeneration. *J Bone Joint Surg Br.* Nov 1996;78(6):965-972.
69. O'Connell GD, Jacobs NT, Sen S, Vresilovic EJ, Elliott DM. Axial creep loading and unloaded recovery of the human intervertebral disc and the effect of degeneration. *J Mech Behav Biomed Mater.* Oct 2011;4(7):933-942.
70. Cripton PA, Jain GM, Wittenberg RH, Nolte LP. Load-sharing characteristics of stabilized lumbar spine segments. *Spine (Phila Pa 1976).* Jan 15 2000;25(2):170-179.
71. Kettler A, Rohlmann F, Ring C, Mack C, Wilke HJ. Do early stages of lumbar intervertebral disc degeneration really cause instability? Evaluation of an in vitro database. *European Spine Journal.* 2010;20(4):578-584.
72. Niosi CA, Oxland TR. Degenerative mechanics of the lumbar spine. *Spine J.* Nov-Dec 2004;4(6 Suppl):202S-208S.
73. Tanaka N, An HS, Lim TH, Fujiwara A, Jeon CH, Haughton VM. The relationship between disc degeneration and flexibility of the lumbar spine. *Spine J.* Jan-Feb 2001;1(1):47-56.
74. Mimura M, Panjabi MM, Oxland TR, Crisco JJ, Yamamoto I, Vasavada A. Disc degeneration affects the multidirectional flexibility of the lumbar spine. *Spine (Phila Pa 1976).* Jun 15 1994;19(12):1371-1380.
75. Fujiwara A, Lim TH, An HS, et al. The effect of disc degeneration and facet joint osteoarthritis on the segmental flexibility of the lumbar spine. *Spine (Phila Pa 1976).* Dec 1 2000;25(23):3036-3044.
76. Kirkaldy-Willis WH, Farfan HF. Instability of the lumbar spine. *Clin Orthop Relat Res.* May 1982(165):110-123.
77. Brown MD, Holmes DC, Heiner AD. Measurement of cadaver lumbar spine motion segment stiffness. *Spine (Phila Pa 1976).* May 1 2002;27(9):918-922.
78. Haughton VM, Lim TH, An H. Intervertebral disk appearance correlated with stiffness of lumbar spinal motion segments. *AJNR Am J Neuroradiol.* Jun-Jul 1999;20(6):1161-1165.
79. Gertzbein SD, Seligman J, Holtby R, et al. Centrode patterns and segmental instability in degenerative disc disease. *Spine (Phila Pa 1976).* Apr 1985;10(3):257-261.
80. Seligman JV, Gertzbein SD, Tile M, Kapasouri A. Computer analysis of spinal segment motion in degenerative disc disease with and without axial loading. *Spine (Phila Pa 1976).* Sep 1984;9(6):566-573.
81. Haheer TR, Bergman M, O'Brien M, et al. The effect of the three columns of the spine on the instantaneous axis of rotation in flexion and extension. *Spine.* Aug 1991;16(8 Suppl):S312-318.
82. Pearcy MJ, Bogduk N. Instantaneous axes of rotation of the lumbar intervertebral joints. *Spine.* Sep 1988;13(9):1033-1041.

83. Kettler A, Marin F, Sattelmayer G, et al. Finite helical axes of motion are a useful tool to describe the three-dimensional in vitro kinematics of the intact, injured and stabilised spine. *Eur Spine J.* Oct 2004;13(6):553-559.
84. Zhu Q, Larson CR, Sjøvold SG, et al. Biomechanical evaluation of the Total Facet Arthroplasty System: 3-dimensional kinematics. *Spine.* Jan 1 2007;32(1):55-62.
85. Niosi CA, Zhu QA, Wilson DC, Keynan O, Wilson DR, Oxland TR. Biomechanical characterization of the three-dimensional kinematic behaviour of the Dynesys dynamic stabilization system: an in vitro study. *Eur Spine J.* Jun 2006;15(6):913-922.
86. Lund T, Nydegger T, Schlenzka D, Oxland TR. Three-dimensional motion patterns during active bending in patients with chronic low back pain. *Spine (Phila Pa 1976).* Sep 1 2002;27(17):1865-1874.
87. Stokes IA, Wilder DG, Frymoyer JW, Pope MH. 1980 Volvo award in clinical sciences. Assessment of patients with low-back pain by biplanar radiographic measurement of intervertebral motion. *Spine (Phila Pa 1976).* May-Jun 1981;6(3):233-240.
88. Wheeler DJ, Freeman AL, Ellingson AM, et al. Inter-laboratory variability in in vitro spinal segment flexibility testing. *Journal of Biomechanics.* 2011;44(13):2383-2387.
89. Wilke HJ, Wenger K, Claes L. Testing criteria for spinal implants: recommendations for the standardization of in vitro stability testing of spinal implants. *Eur Spine J.* 1998;7(2):148-154.
90. Spoor CW, Veldpaus FE. Rigid body motion calculated from spatial co-ordinates of markers. *J Biomech.* 1980;13(4):391-393.
91. Woltring HJ, Huiskes R, de Lange A, Veldpaus FE. Finite centroid and helical axis estimation from noisy landmark measurements in the study of human joint kinematics. *J Biomech.* 1985;18(5):379-389.
92. Woltring HJ, Long K, Osterbauer PJ, Fuhr AW. Instantaneous helical axis estimation from 3-D video data in neck kinematics for whiplash diagnostics. *J Biomech.* Dec 1994;27(12):1415-1432.
93. Anderst W, Baillargeon E, Donaldson W, Lee J, Kang J. Motion Path of the Instant Center of Rotation in the Cervical Spine During In Vivo Dynamic Flexion-Extension: Implications for Artificial Disc Design and Evaluation of Motion Quality Following Arthrodesis. *Spine (Phila Pa 1976).* Feb 20 2013.
94. Metzger MF, Faruk Senan NA, O'Reilly OM, Lotz JC. Minimizing errors associated with calculating the location of the helical axis for spinal motions. *Journal of Biomechanics.* 2010;43(14):2822-2829.
95. Cripton PA, Sati M, Orr TE, Bourquin Y, Dumas GA, Nolte LP. Animation of in vitro biomechanical tests. *J Biomech.* Aug 2001;34(8):1091-1096.
96. Wachowski MM, Hubert J, Hawellek T, et al. Axial rotation in the lumbar spine following axial force wrench. *J Physiol Pharmacol.* Dec 2009;60 Suppl 8:61-64.

97. Mak AF, Lai WM, Mow VC. Biphasic indentation of articular cartilage--I. Theoretical analysis. *J Biomech.* 1987;20(7):703-714.
98. Natoli KAAaRM. *Introduction to Continuum Biomechanics.* Morgan & Claypool; 2008.
99. Natarajan RN, Williams JR, Andersson GB. Modeling changes in intervertebral disc mechanics with degeneration. *J Bone Joint Surg Am.* Apr 2006;88 Suppl 2:36-40.
100. Suh JK, DiSilvestro MR. Biphasic Poroviscoelastic Behavior of Hydrated Biological Soft Tissue. *Journal of Applied Mechanics.* June 1999;66.
101. Suh JK, Bai S. Finite element formulation of biphasic poroviscoelastic model for articular cartilage. *J Biomech Eng.* Apr 1998;120(2):195-201.
102. Starcher B. A ninhydrin-based assay to quantitate the total protein content of tissue samples. *Anal Biochem.* May 1 2001;292(1):125-129.
103. Stegemann H, Stalder K. Determination of hydroxyproline. *Clin Chim Acta.* Nov 1967;18(2):267-273.
104. Carrino JA, Lurie JD, Tosteson AN, et al. Lumbar spine: reliability of MR imaging findings. *Radiology.* Jan 2009;250(1):161-170.
105. Wilke H, Neef P, Hinz B, Seidel H, Claes L. Intradiscal pressure together with anthropometric data--a data set for the validation of models. *Clin Biomech (Bristol, Avon).* 2001;16 Suppl 1:S111-126.
106. Andersson GB, Ortengren R, Nachemson A. Intradiskal pressure, intra-abdominal pressure and myoelectric back muscle activity related to posture and loading. *Clin Orthop Relat Res.* Nov-Dec 1977(129):156-164.
107. Kettler A, Rohlmann F, Ring C, Mack C, Wilke HJ. Do early stages of lumbar intervertebral disc degeneration really cause instability? Evaluation of an in vitro database. *Eur Spine J.* Apr 2011;20(4):578-584.
108. Oxland TR, Lund T, Jost B, et al. The relative importance of vertebral bone density and disc degeneration in spinal flexibility and interbody implant performance. An in vitro study. *Spine (Phila Pa 1976).* Nov 15 1996;21(22):2558-2569.
109. Fujita Y, Duncan NA, Lotz JC. Radial tensile properties of the lumbar annulus fibrosus are site and degeneration dependent. *J Orthop Res.* Nov 1997;15(6):814-819.
110. Acaroglu ER, Iatridis JC, Setton LA, Foster RJ, Mow VC, Weidenbaum M. Degeneration and aging affect the tensile behavior of human lumbar anulus fibrosus. *Spine (Phila Pa 1976).* Dec 15 1995;20(24):2690-2701.
111. Skaggs DL, Weidenbaum M, Iatridis JC, Ratcliffe A, Mow VC. Regional variation in tensile properties and biochemical composition of the human lumbar anulus fibrosus. *Spine (Phila Pa 1976).* Jun 15 1994;19(12):1310-1319.

112. Jensen GM. Biomechanics of the lumbar intervertebral disk: a review. *Phys Ther.* Jun 1980;60(6):765-773.
113. Périé D, Iatridis JC, Demers CN, et al. Assessment of compressive modulus, hydraulic permeability and matrix content of trypsin-treated nucleus pulposus using quantitative MRI. *Journal of Biomechanics.* 2006;39(8):1392-1400.
114. Apprigh S, Mamisch TC, Welsch GH, et al. Quantitative T2 mapping of the patella at 3.0T is sensitive to early cartilage degeneration, but also to loading of the knee. *European Journal of Radiology.* 2012;81(4):e438-e443.
115. Subburaj K, Kumar D, Souza RB, et al. The Acute Effect of Running on Knee Articular Cartilage and Meniscus Magnetic Resonance Relaxation Times in Young Healthy Adults. *The American Journal of Sports Medicine.* 2012;40(9):2134-2141.
116. Grant JP, Oxland TR, Dvorak MF. Mapping the structural properties of the lumbosacral vertebral endplates. *Spine.* Apr 15 2001;26(8):889-896.
117. Rohlmann A, Neller S, Claes L, Bergmann G, Wilke HJ. Influence of a follower load on intradiscal pressure and intersegmental rotation of the lumbar spine. *Spine (Phila Pa 1976).* Dec 15 2001;26(24):E557-561.

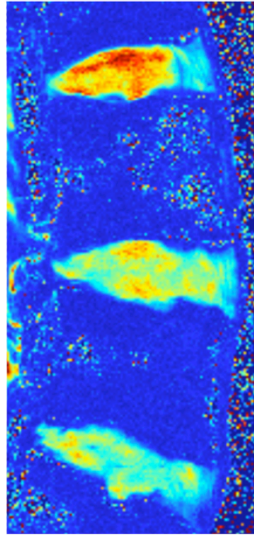
8 APPENDIX

The appendix expands upon two aspects of this dissertation. The first section will focus on the T2* maps and display the corresponding imaging parameters assessing disc health. These include the nucleus pulposus T2* relaxation time, T2* Intensity Area, Transition Zone Slope, and Pfirrmann Grade (based on T2-weighted MRI). The following section details the validation and sensitivity analysis in the parameters used to calculate the instantaneous axis of rotation.

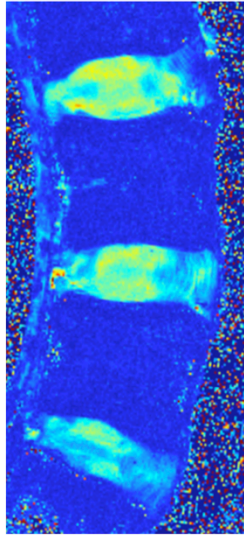
8.1 T2* MRI MAPS

This section of the appendix includes a T2* MRI map of the mid-sagittal slice of each Lumbar Spine (L3-S1). Below the T2* maps is information regarding each intervertebral disc's imaging parameters. The Pfirrmann Grade based on clinical T2-weighted MR images were averaged across seven spine surgeons and three experienced spine researchers. The calculated inter-correlation coefficient was 0.686, indicating a moderate degree of variability due to the subjectivity of the grading scheme. The quantitative T2* imaging parameters, NP T2* Relaxation Time, T2* Intensity Area, and Transition Zone Slope, are also included.

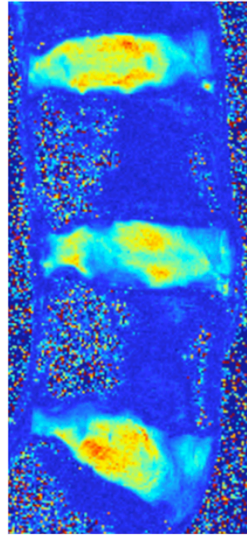
1



2



3

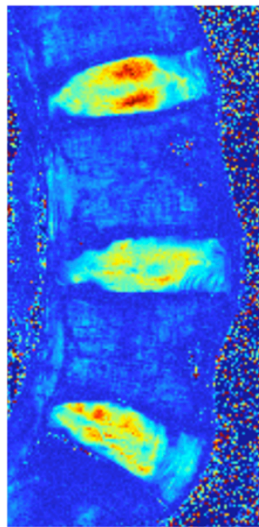


	L3-4	L4-5	L5-S1
Pfirrmann Grade	2	3	4
NP T2* Value (ms)	57.62	45.28	34.64
T2* Intensity Area (ms)	2.88	1.96	1.04
Transition Zone Slope (ms/mm)	40.27	30.53	20.62

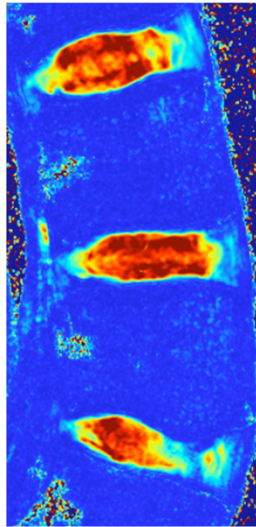
	L3-4	L4-5	L5-S1
Pfirrmann Grade	3	3	3
NP T2* Value (ms)	39.84	38.44	29.96
T2* Intensity Area (ms)	2.44	2.05	1.61
Transition Zone Slope (ms/mm)	26.48	26.14	18.16

	L3-4	L4-5	L5-S1
Pfirrmann Grade	2	3	2
NP T2* Value (ms)	48.16	41.82	49.32
T2* Intensity Area (ms)	2.49	1.24	1.55
Transition Zone Slope (ms/mm)	36.74	30.52	28.16

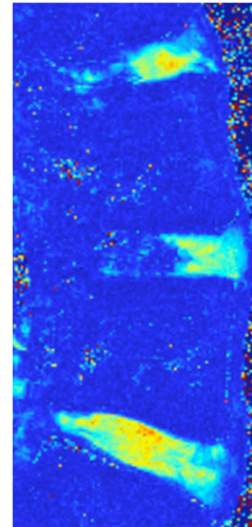
4



5



6

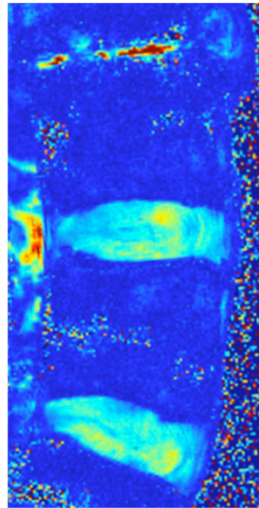


	L3-4	L4-5	L5-S1
Pfirrmann Grade	2	3	2
NP T2* Value (ms)	53.42	40.63	45.43
T2* Intensity Area (ms)	2.38	1.75	3.71
Transition Zone Slope (ms/mm)	30.96	23.82	30.85

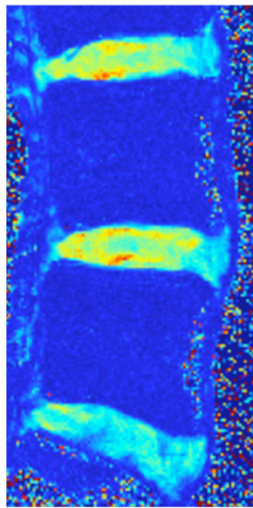
	L3-4	L4-5	L5-S1
Pfirrmann Grade	1	1	2
NP T2* Value (ms)	72.74	76.64	55.45
T2* Intensity Area (ms)	4.50	4.65	3.17
Transition Zone Slope (ms/mm)	42.64	42.79	27.63

	L3-4	L4-5	L5-S1
Pfirrmann Grade	5	5	4
NP T2* Value (ms)	18.19	27.10	46.55
T2* Intensity Area (ms)	1.70	1.02	3.39
Transition Zone Slope (ms/mm)	18.38	17.77	28.33

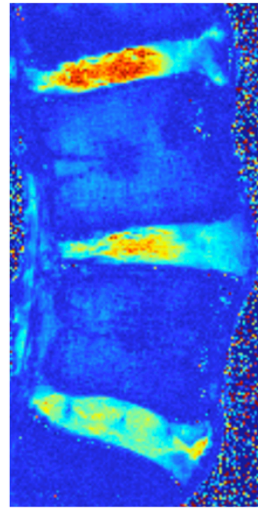
7



8



9

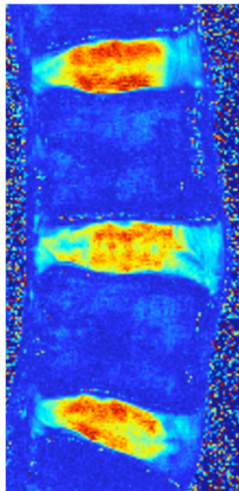


	L3-4	L4-5	L5-S1
Pfirrmann Grade	5	3	3
NP T2* Value (ms)	N/A	42.54	32.95
T2* Intensity Area (ms)	N/A	2.53	2.49
Transition Zone Slope (ms/mm)	N/A	26.17	21.78

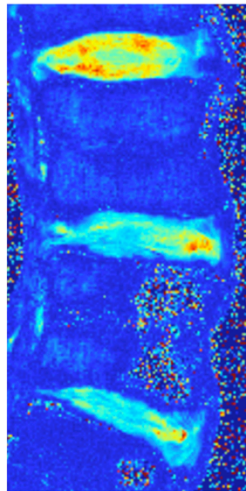
	L3-4	L4-5	L5-S1
Pfirrmann Grade	4	4	3
NP T2* Value (ms)	41.94	41.95	27.11
T2* Intensity Area (ms)	2.37	3.14	1.96
Transition Zone Slope (ms/mm)	27.43	29.41	16.01

	L3-4	L4-5	L5-S1
Pfirrmann Grade	4	5	4
NP T2* Value (ms)	63.58	48.75	35.41
T2* Intensity Area (ms)	2.76	2.59	1.94
Transition Zone Slope (ms/mm)	32.45	27.63	18.45

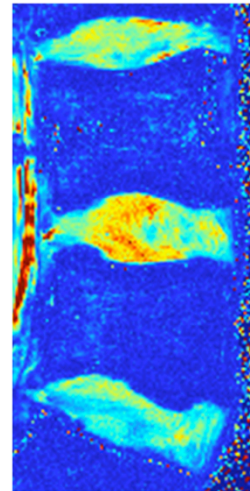
10



11



12

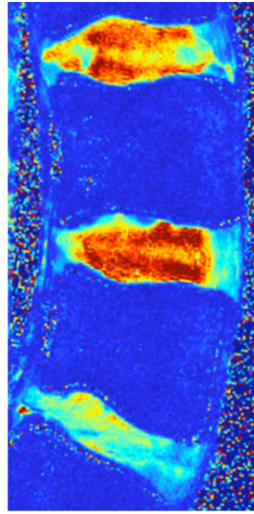


	L3-4	L4-5	L5-S1
Pfirrmann Grade	1	2	1
NP T2* Value (ms)	61.36	53.30	56.02
T2* Intensity Area (ms)	3.72	2.56	2.73
Transition Zone Slope (ms/mm)	40.11	30.86	30.37

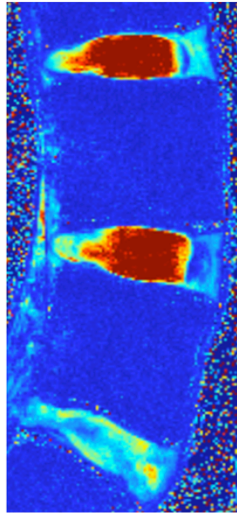
	L3-4	L4-5	L5-S1
Pfirrmann Grade	3	4	5
NP T2* Value (ms)	44.46	28.64	28.42
T2* Intensity Area (ms)	2.92	1.04	0.48
Transition Zone Slope (ms/mm)	32.16	22.33	14.45

	L3-4	L4-5	L5-S1
Pfirrmann Grade	5	3	4
NP T2* Value (ms)	38.35	61.36	53.30
T2* Intensity Area (ms)	3.12	3.82	2.70
Transition Zone Slope (ms/mm)	24.16	28.43	24.07

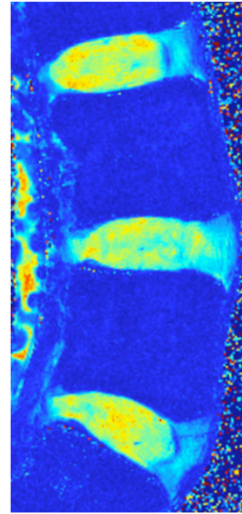
13



14



15

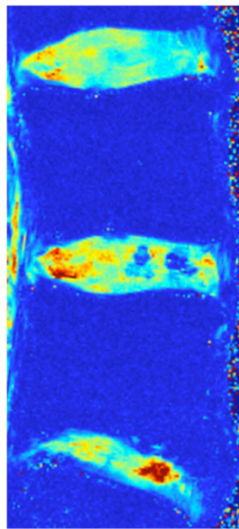


	L3-4	L4-5	L5-S1
Pfirrmann Grade	3	2	4
NP T2* Value (ms)	58.73	70.60	35.02
T2* Intensity Area (ms)	1.94	2.53	2.39
Transition Zone Slope (ms/mm)	45.79	46.13	27.56

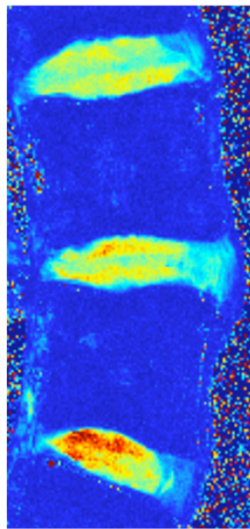
	L3-4	L4-5	L5-S1
Pfirrmann Grade	1	1	4
NP T2* Value (ms)	93.30	91.56	27.45
T2* Intensity Area (ms)	7.28	4.39	2.69
Transition Zone Slope (ms/mm)	54.12	54.62	26.39

	L3-4	L4-5	L5-S1
Pfirrmann Grade	2	3	2
NP T2* Value (ms)	43.54	58.73	70.60
T2* Intensity Area (ms)	2.81	1.79	2.30
Transition Zone Slope (ms/mm)	30.31	25.51	27.47

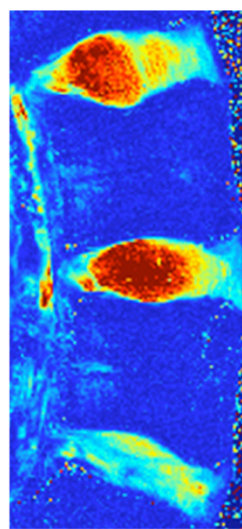
16



17



18



	L3-4	L4-5	L5-S1
Pfirrmann Grade	3	3	5
NP T2* Value (ms)	36.90	38.40	31.55
T2* Intensity Area (ms)	1.63	1.91	1.34
Transition Zone Slope (ms/mm)	23.61	22.65	26.21

	L3-4	L4-5	L5-S1
Pfirrmann Grade	3	3	2
NP T2* Value (ms)	41.88	45.11	51.89
T2* Intensity Area (ms)	2.74	2.04	3.30
Transition Zone Slope (ms/mm)	27.69	31.71	28.18

	L3-4	L4-5	L5-S1
Pfirrmann Grade	2	1	4
NP T2* Value (ms)	62.09	36.90	38.40
T2* Intensity Area (ms)	4.18	4.62	2.21
Transition Zone Slope (ms/mm)	39.81	49.27	23.37

8.2 HELICAL AXIS COMPUTATION

This section of the appendix will first validate the computation of the helical axes using an object with a known center of rotation to verify location and direction of the calculated vector. This will be followed by a sensitivity analysis of the filtering parameters used on the kinematic data.

8.2.1 HELICAL AXIS VALIDATION

The helical axes were computed for a goniometer, which is a hinge joint with a known center of rotation. This procedure was conducted to ensure validity of the MATLAB script. Four infrared reflective markers were placed on each arm of the goniometer and one placed on the center of rotation (Figure 8.1). A rotation of 90 degrees was performed while position data was being captured by the Vicon system. Five axes were computed throughout the motion and error was estimated both by the discrepancy between the marker placed at the center of rotation and the computed IAR, as well as the magnitude of the z component of the helical axis. The rotation of a pure hinge joint will be a unit vector pointing orthogonal to the plane of rotation.

The largest deviation from the marked center of rotation was 1.73 mm. The error could be attributed to the imprecise placement of the center of rotation marker, or the large volume used to capture the activity (performed in gait lab, rather than the small volume to be used with the SKS). The components of the helical axis unit vector were entirely in the z direction (<1% error).

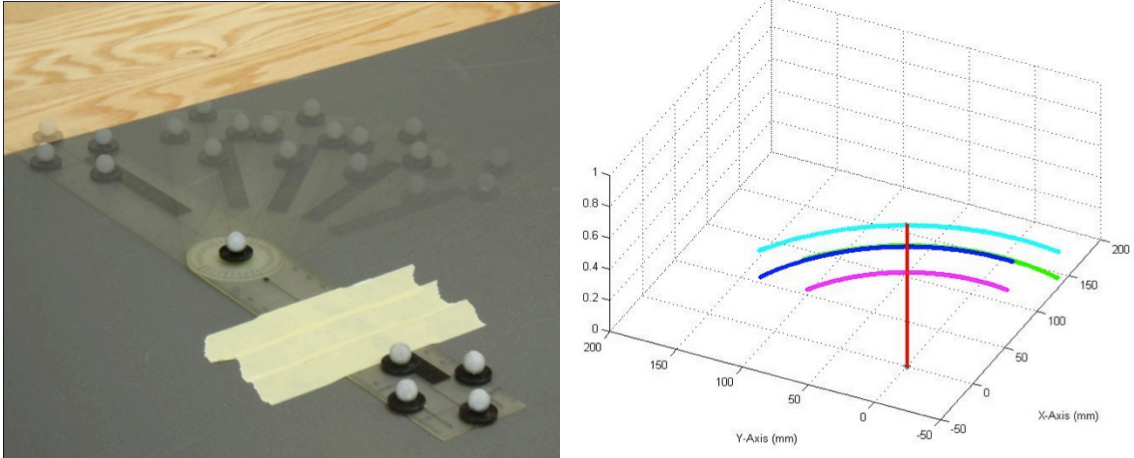


Figure 8.1. Helical Axis Validation Set-up.

To validate the helical axis analysis a goniometer was equipped with reflective markers on each arm and one placed at the center of rotation (left). The apparatus was then rotated 90 degrees. The helical axis was then solved to verify the location and direction of the vector (right). The red vectors represent the placement and orientation of the helical axis. The black asterisk is the marker position placed at the center of rotation. The four colors (cyan, magenta, green, and blue) represent the four markers on the arm of the goniometer as it was moved through space.

8.2.2 HELICAL AXIS SENSITIVITY ANALYSIS

A sensitivity analysis for the calculation of the instantaneous helical axes was performed on a healthy L4-L5 intervertebral disc for lateral bending. The axes were computed over a 0.05 degree increment and assessed based on the low-pass cutoff frequency used in a fourth order forward-backward Butterworth filter. The low-pass cutoff frequencies presented herein are 3.2, 0.8, 0.4, and 0.2 Hz. These were chosen based on similar literature values, and to display over and under filtering of the data. The root mean square of the error (RMSE) was measured between the angular displacement with and without filtering.

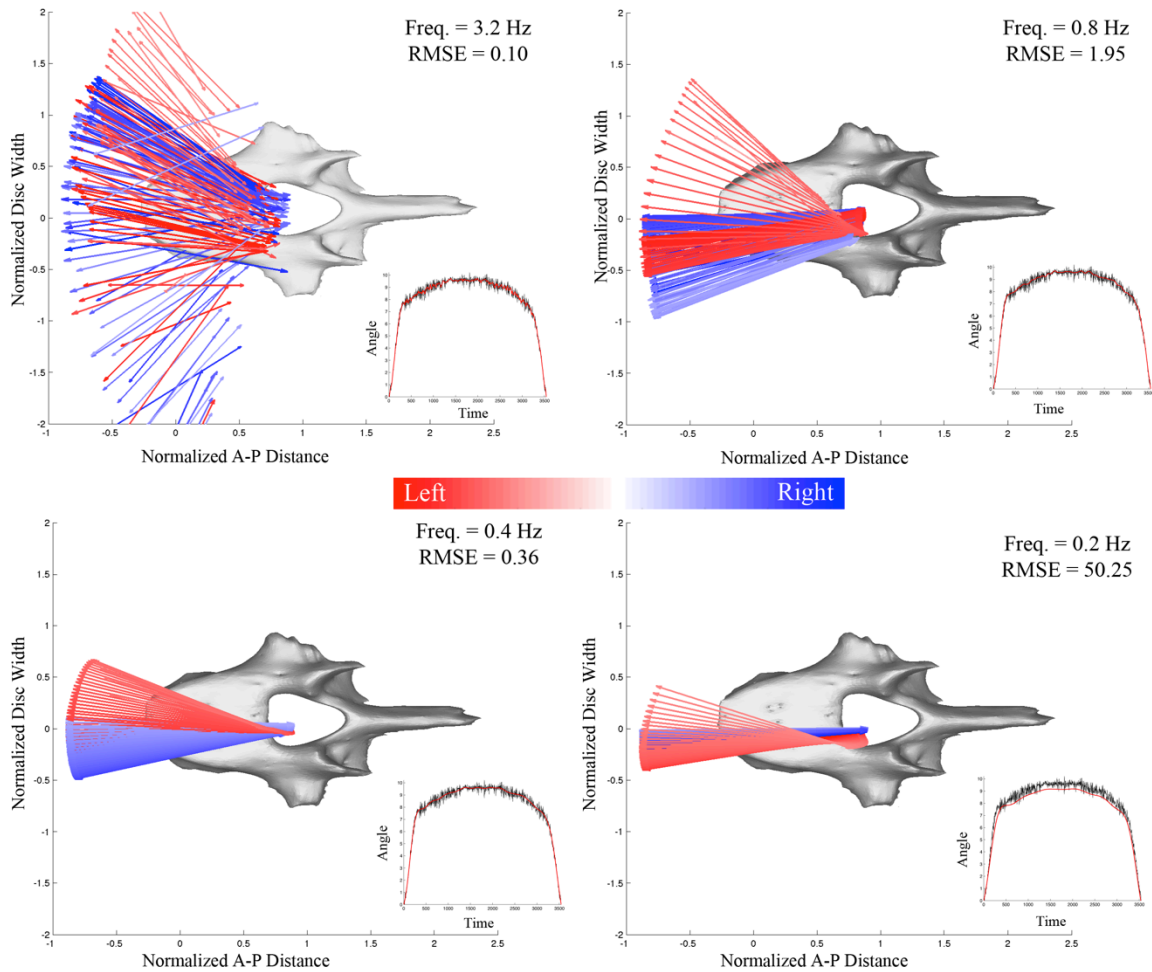


Figure 8.2. Helical Axis Sensitivity Analysis.

The helical axes were calculated at 0.05 degree increments using varying low-pass cutoff frequencies in a forward-backward Butterworth filter. The frequencies displayed are 3.2, 0.8, 0.4, and 0.2 Hz. The root mean squared error (RMSE) was measured between the angular displacement with and without filtering.

Following this sensitivity analysis a cut-off frequency of 0.4 Hz was chosen for the helical axes computations. Higher frequencies displayed stray vectors that were located outside the disc space and oriented in a sporadic fashion. Lower frequencies drastically altered the angular displacement, resulting in an RMS error of 50.25.